Small-Scale Laterally Loaded Non-Slender Monopiles in Sand

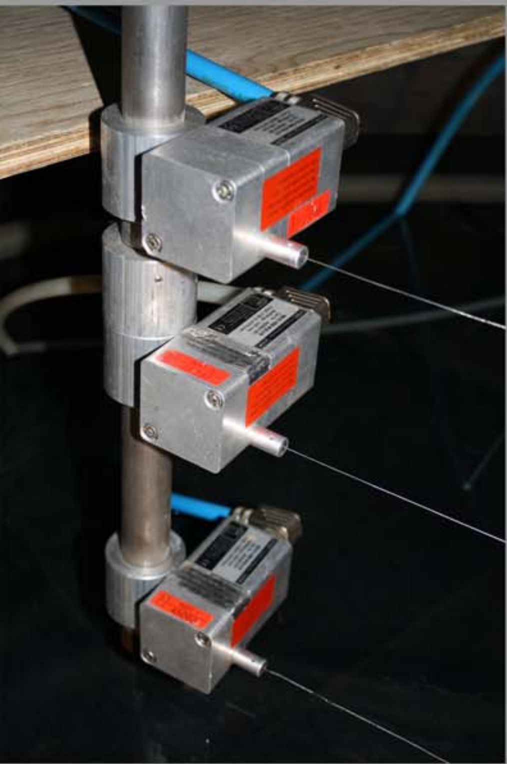

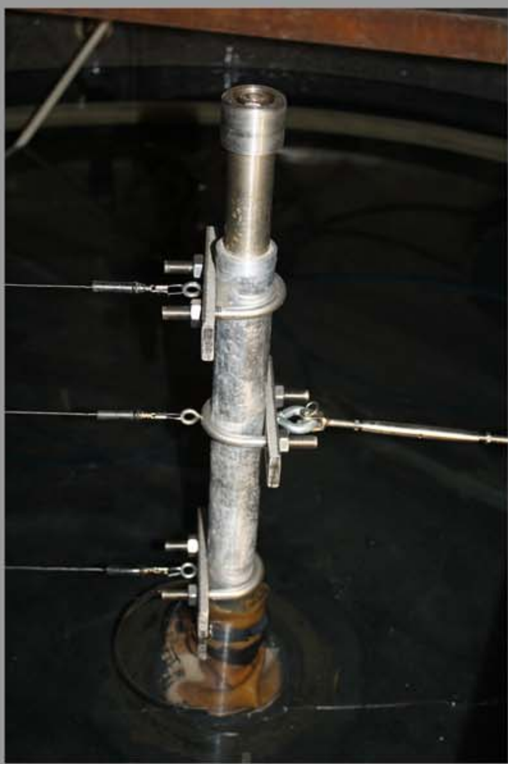

Master's Thesis

Hanne R. Roesen
Kristina Thomassen

Aalborg University
M.Sc. in Civil and Structural Engineering

June 2010

4th semester – M.Sc.
Sohngårdsholmsvej 57
9000 Aalborg
+45 96 35 80 80
http://www.bsn.aau.dk

Title:
Small-Scale Laterally Loaded Non-Slender Monopiles in Sand

Written by:
Hanne R. Roesen
Kristina Thomassen

Graduate Students
Department of Civil Engineering,
Aalborg University, Denmark

Supervisors:
Professor Lars Bo Ibsen
PhD Fellow Søren P. H. Sørensen

Department of Civil Engineering,
Aalborg University, Denmark

Project Period: Spring 2010

Completed: 2010.06.10

Copies printed: 5

Number of pages: 76

Number of pages (appendix): 115

Hanne R. Roesen *Kristina Thomassen*

PREFACE

This thesis "Small-Scale Laterally Loaded Non-Slender Monopiles in Sand" is a Master's thesis conducted in the period February to June 2010 at the Faculties of Engineering, Science, and Medicine, Aalborg University, Denmark.

The thesis consists of two papers and a number of related appendices. A list of references is situated after each paper, after the concluding remarks, and after the last appendix. The appendices are numbered by letters. Figures, tables and equations are presented with consecutive numbers in each paper/appendix. The two articles are printed with individual page numbering. The page numbering of the appendices are consecutive with the rest of the thesis. Cited references are marked with author specifications and year of publication.

A pdf-script of the thesis and the used computational programs are included on the enclosed CD.

The project is associated with the EFP programme "Physical and numerical modelling of monopile for offshore wind turbines", journal no. 033001/33033-0039. The funding is sincerely acknowledged. The supervisors, Professor Lars Bo Ibsen and PhD Fellow Søren P. H. Sørensen are thanked for their assistance during the project. Assistant Engineers Kurt S. Sørensen and Jan Laursen are thanked for their assistance during the laboratory tests.

SUMMARY IN ENGLISH

In current design of offshore wind turbines, monopiles are often used as foundation. The design method for monopiles in sand is based on $p-y$ curves, which are derived from large-scale testing on two flexible, slender piles. The method has proven valid for piles with diameters up to approximately 2 m, but the effect of the diameter is not taken into account. Another assumption for the curves is that the piles have a flexible behaviour. The $p-y$ curves are developed with a main focus on the ultimate lateral resistance and, hence, little attention has been given to the initial stiffness of the pile-soil interaction.

Recently installed monopiles have diameters of 4 m to 6 m and a slenderness ratio less than 10. Thereby, the design curves are used outside the verified range as the pile diameters are much larger, and the piles have a more rigid than flexible behaviour. This rigidity causes the pile to rotate when subjected to lateral loading from wind and waves. As the efficiency of the wind turbine decreases if the tower obtains a rotation the initial stiffness of the $p-y$ curves is very important.

Six small-scale tests are conducted to evaluate the pile-soil interaction for non-slender monopiles in sand subjected to lateral loading. The tests are conducted on two closed-ended aluminium pipe piles with outer diameters of 40 mm and 100 mm and a slenderness ratio of 5. The tests are conducted with overburden pressures of 0 kPa, 50 kPa, and 100 kPa to avoid the problems with the non-linear yield surface at low stress levels. The piles are instrumented with a force transducer and displacement transducers located at three positions above the soil surface. By the measurements from these transducers load-deflection relationships for the piles are obtained.

The load-deflection relationships obtained from the tests are used to evaluate existing formulations for the soil resistance by means of a Winkler model approach. Furthermore, the relationships are used to calibrate six numerical finite difference models in FLAC^{3D}. $p-y$ curves representing the small-scale tests are computed from these models and compared to the $p-y$ curves recommended by the design regulations API (1993) and DNV (1992). From the small-scale tests and the evaluation of the test results the following conclusions are drawn.

Small-scale tests conducted at low stress levels gives inaccurate results, i.e. small-scale tests should be conducted at higher stress levels. When conducting tests on the 40 mm pile little disturbance of the soil caused large uncertainties of the

test results and, hence, piles with a larger diameter should be used in small-scale tests. In spite of these problems the test results indicated that the lateral load is proportional to the length squared times the diameter, $H \propto L^2 D$.

The results from the numerical models indicated that the initial stiffness of the $p-y$ curves increases with increasing diameter and varies non-linearly with the it. Furthermore, it is found that the piles behave more rigid than flexible, which cause a rotation and a toe-kick of the pile.

Replacing the linear expression for the initial stiffness of the $p-y$ curves given in the design regulations by a non-linear expression provides a better agreement with the small-scale test results.

SUMMARY IN DANISH (SAMMENDRAG)

Monopæle bruges ofte som funderingsmetode ved dimensionering af offshore vindmøller. Dimensioneringsmetoden for monopæle i sand er baseret på $p-y$ kurver, som er udledt på baggrund af fuldskala forsøg på to fleksible, slanke pæle. Kurverne har vist sig gyldige for pæle med diametre op til ca. 2 m, men diametereffekten er ikke taget i betragtning. En anden antagelse for kurverne er, at pælene har en fleksibel adfærd. $p-y$ kurverne er udviklet med fokus på det ultimative jordtryk, og der har ikke været fokus på initialstivheden af pæl-jordinteraktionen.

De monopæle, der installeres i dag, har diametre på 4 m til 6 m og et slankhedsforhold mindre end 10. Dermed anvendes $p-y$ kurverne udenfor det verificerede område, da pælenes diametre er meget større, og pælene opfører sig mere stift end fleksibelt. Stivheden af pælene bevirker, at de vil rotere, når de udsættes for tværbelastning fra vind og bølger. Da effektiviteten af vindmøllen falder, hvis tårnet opnår en rotation, er initialstivheden af $p-y$ kurverne meget vigtigt.

Seks modelforsøg er udført for at vurdere pæl-jordinteraktionen for ikke-slanke monopæle i sand udsat for tværbelastning. Forsøgene er udført på to aluminiumspæle med lukkede ender og et slankhedsforhold på 5. Pælene havde ydre diametre på 40 mm og 100 mm. Forsøgene er udført med en overfladebelastning på hhv. 0 kPa, 50 kPa og 100 kPa for at undgå problemer med den ikke-lineære brudbetingelse ved lave spændingsniveauer. Pælene er instrumenteret med en kraftmåler og flytningsmålere placeret i tre niveauer over jordoverfladen. Ud fra dataene fra kraft- og flytningsmålerne er kraft-flytningskurver for pælene fundet.

Kraft-flytningskurverne fra forsøgene anvendes til at evaluerede de eksisterende formuleringer for jordtrykket vha. en Winkler model. Kurverne er desuden brugt til at kalibrere seks numeriske finite difference modeller i FLAC^{3D}. Ud fra disse modeller er $p-y$ kurver for modelforsøgene fundet og sammenlignet med $p-y$ kurverne anbefalet i API (1993) og DNV (1992). Fra modelforsøgene og evalueringen af forsøgsresultaterne kan følgende konklusioner drages.

Modelforsøg udført ved lavt spændingsniveau giver unøjagtige resultater, dvs. modelforsøg bør udføres ved højere spændingsniveau. Små forstyrrelser af jorden forårsagede store usikkerheder for forsøgsresultaterne for 40 mm pælen. Ved yderligere modelforsøg bør pæle med større diametre derfor bruges. På trods af disse

usikkerheder indikerede resultaterne, at tværbelastningen er proportional med længden opløftet i anden multipliceret med diameteren, $H \propto L^2D$.

Resultaterne fra de numeriske modeller viste, at initialstivheden af $p-y$ kurverne øges med større pælediameter og varierer ikke-lineært med den. Desuden opfører pælene sig mere stift end fleksibelt, hvilket giver en rotation og en flytning af pælenes fod.

Erstatning af det lineære udtryk for initialstivheden af $p-y$ kurverne givet i dimensioneringsstandarderne med et ikke-lineære udtryk giver større overenstemmelse med forsøgsresultaterne.

CONTENTS

CHAPTER 1

INTRODUCTION

In the effort towards becoming independent of fossil fuels the development of renewable energy sources are in great focus. Wind power is a largely growing energy resource as the pollution-free power production contributes to the reduction of CO_2. During the last ten years an increase of installed wind capacity world wide of more than 800 % has happened, cf. Fig. 1.1. The installed wind capacity at the end of 2009 equals about thirteen times the total energy demand in Denmark and about 2 % of the global electricity consumption. (World Wind Energy Association, 2010)

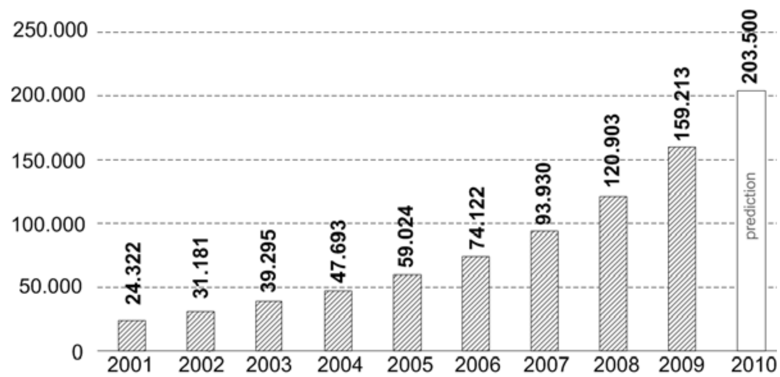

Figure 1.1: Amount of installed wind power word wide. The capacities are given in MW. After World Wind Energy Association (2010)

Since the seventies the Danish government has made several strategies toward securing the future energy supply and increase the amount of low-pollution energy. In 1996 the strategy *Energi 21* (Miljø- og Energiministeriet, 1996) was adopted. The specific goals required that by the year 2005 the total installed wind power should be 1500 MW and by the year 2030 it should be 5550 MW, which corresponds to approximately 50 % of the total Danish energy demand expected in 2030. 4000 MW of the total wind power is expected to originate from offshore installations. In 1999, six years before planned, the first goal was reached and by the end of 2009 the total wind capacity in Denmark was 3497 MW, in which the offshore share was 633 MW. (Offshore Center Danmark, 2010; World Wind Energy Association, 2010)

Due to the attention from the Danish government Denmark has become a pioneer within the field of offshore wind energy and the worlds first offshore wind farm was installed in Denmark north of Lolland in 1991. Until then all wind turbines were placed onshore, but dense populations, existing build-up areas, and preserved areas generated a problem finding suitable locations. Furthermore, the limit of the size of onshore wind turbines, hence efficiency, was nearly reached due to logistic problems when transporting the large components. (Offshore Center Danmark, 2010; Dong Energy, 2010)

By installing wind turbines offshore the above-mentioned problems are avoided, and it is possible to choose a location that does not visually mar the nature. The limitation regarding transport of the large components are also dealt with as the components can be sailed to the destination. Further, when installing wind turbines offshore the wind is more steady, which results in less turbulence. In average, a wind turbine placed offshore is able to produce up to 50 % more energy than an onshore wind turbine (Danmarks Vindmølleforening, 2010). However, it should be mentioned that the cost of energy is doubled by going offshore (Engels et al., 2010).

It is still a political strategy to enlarge the Danish offshore wind energy sector, and so far the largest offshore wind farm world wide is installed in the North Sea at Horns Rev II. This wind farm has a capacity of 209 MW. In Fig. 1.2 the five largest countries within the field of the offshore wind industry are shown, and it can be seen that Denmark is in the lead along with the United Kingdom.

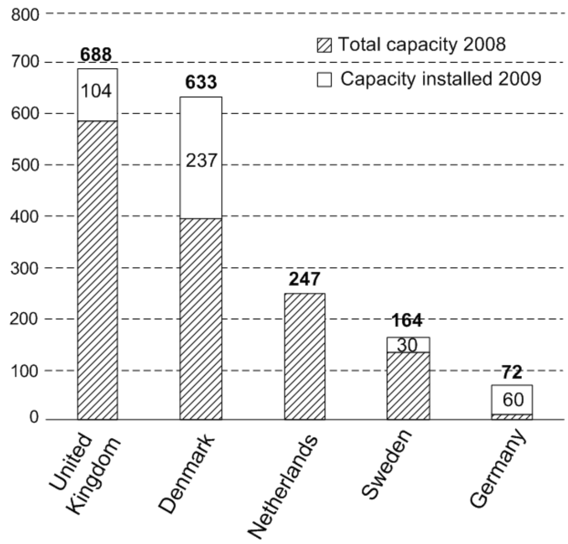

Figure 1.2: Top five countries in the offshore wind industry. The capacities are given in MW. After World Wind Energy Association (2010)

In the following offshore wind turbines and the different types of foundation are in focus.

1.1 Offshore Wind Turbine Foundation Designs

Generally, wind turbines are very sensitive towards rotation of the wind turbine tower. Even a small rotation affects the efficiency of the turbine and, therefore, the standard serviceability limit for rotation is approximately $\pm 0.5°$. This limit is often divided into a limit for allowable installation rotation and allowable accumulated rotation due to wind and wave influence, both with limits of $0.25°$. This demand sets requirements for the foundation and the transfer of forces to the surrounding soil. (Vattenfall, 2010)

Besides being sensitive towards rotation the wind turbines are sensitive towards vibrations. Thus, when choosing the stiffness and, thereby, the eigenfrequencies of the construction it is necessary to take the excitation from the wind, the waves, and the rotation of the blades into account.

The foundation of an offshore wind turbine is subjected to vertical, horizontal and moment forces. The vertical force originates from the weight of the wind turbine whereas the horizontal and moment forces originate from the wind and waves. The forces acting on the foundation must be transferred to the surrounding soil and the design challenge is to find the most economic and suitable solution. The choice of design depends on the type of loading, water depth, and soil conditions. In Fig. 1.3 four common foundation designs for relatively shallow waters are shown, and below the different concepts are described.

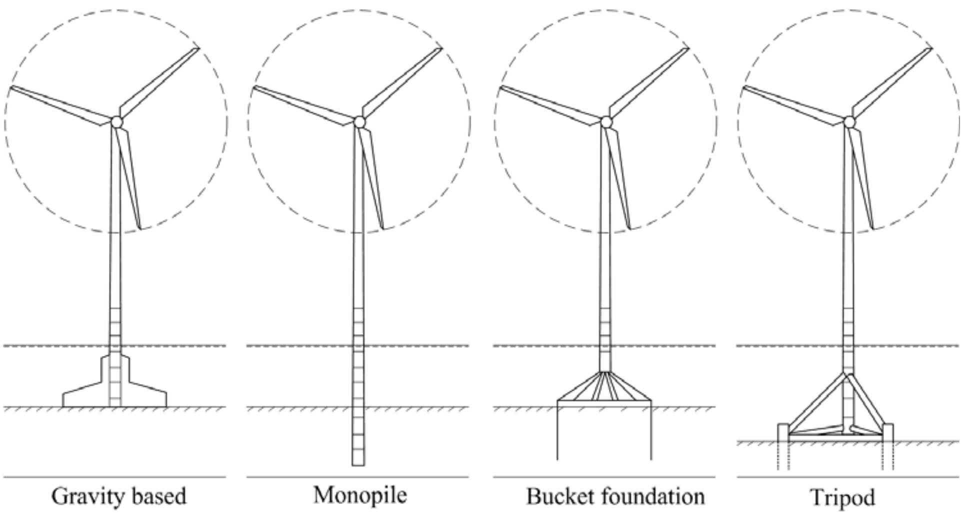

Figure 1.3: Commonly used foundation concepts at relatively shallow waters. After Haus Der Technic (2010)

The gravity based foundation is designed to have sufficient dead load such that tensile loads between the foundation and the seabed are avoided. Moreover, the foundation is designed to resist overturning and sliding. In shallow protected waters the gravity based foundation has shown to be cost effective because it can be installed without use of expensive installation vessels. The foundation is well suited for sites with water depths ranging from 0 to 25 m. (DNV, 2007)

The monopile foundation is the most widely applied concept in resent offshore wind farm development. The monopile is made of a cylindrical steel pipe pile which extends into the soil. The axial bearing capacity of the piles is governed by the shaft and toe resistances, whereas the lateral loads and bending moments are transferred to the surrounding soil by lateral earth pressure acting against the pile. The monopile foundation is well suited for sites with a water depth ranging from 0 to 25 m. (DNV, 2007)

The bucket foundation is a newer concept developed by the oil and gas industry. It is made of a large diameter steel cylinder which is closed at the top, and the length and the diameter is approximately the same size. Depending on the skirt length and diameter, the bucket foundation can have a bearing capacity similar to that of a monopile, a gravity foundation, or in between these two. The bucket is self penetrated by means of suction and, hereby, the use of expensive installations vessels can be avoided. Another advantage of the bucket foundation is that, at the end of the life time, it can be removed by reversing the installation method. The bucket foundation is well suited for sites with water depths ranging from 0 to 25 m. (DNV, 2007)

The tripod is a standard tree-legged structure made as a steel structure with three piles penetrating the soil. Due to the complexity of the structure the tripod requires extensive structural analyses as well as a demanding production phase. The tripod foundation is well suited for sites with water depth ranging from 20 to 50 m. It can, in principle, be constructed at greater depths than 50 m, but the costs become prohibitive. (DNV, 2007)

When designing foundations at seabed the risk of scour needs to be taken into account. The change of the water-particle flow will cause an increase of the shear stress on the seabed around the foundation causing an increase of the sediment transport capacity of the flow. If the seabed consists of friction material scour around the foundation might occur and will be a thread to the stability of the structure. (DNV, 2007)

The above described foundation solutions are only possible at relatively shallow waters. At greater depths alternative solutions concerning floating wind turbines moored to the seabed by catenary or taut lines have been investigated. The advantages of these structures are that they can be used at shores with large water depths or far away form the shore, where they are not visible from shore. Some of the disadvantages are the large costs and the problems of maintenance. Contrary to wind turbines at shallow water neither crane nor wind turbine are fixed to the seabed during installation and reparation. This limits the crane to operate only under very calm conditions. (Stiesdal, 2009)

As mentioned the monopile is the most widely used concept of offshore wind turbine foundation. Nevertheless, the shortcomings of the design method are not fully investigated. In this thesis the design method for lateral capacity of the monopile foundation will be evaluated. Only monopiles in sand will be considered. The problems concerning protection against scour will not be discussed.

1.2 Design Methods for Laterally Loaded Piles

When designing the monopiles the serviceability mode is very important because of the strict demands for the rotation and vibration. Therefore, not only the failure mode and, thereby, the ultimate soil resistance, p_u, is of interest. The soil resistance and, thus, the deflection of the pile at any given lateral load is important in the design.

The existing methods for analysing laterally loaded piles can in general be classified in five categories. (Fan and Long, 2005)

1. The limit state method
2. The subgrade reaction method
3. The $p-y$ curve method
4. The elasticity method
5. Numerical modelling

1. The limit state method is the simplest of these methods, but it considers only the ultimate soil resistance, p_u. In the method p_u is assumed to be directly proportional to the depth below seabed and the diameter of the pile. (Fan and Long, 2005)

2. If the soil resistance, p, for a given applied horizontal deflection is to be found the subgrade reaction method is the simplest method. In this method the soil resistance is assumed linearly dependent on the pile deflection, y. This is a rough assumption because full-scale tests has substantiated a non-linear relationship. Further, it is not possible to predict the ultimate soil resistance when using the subgrade reaction method. (Fan and Long, 2005)

3. The $p-y$ curve method is used to describe the non-linear relationship between the soil resistance and the pile deflection. The first semi-empirical expressions for $p-y$ curves in sand were formulated by Reese et al. (1974) including an expression for estimating the ultimate soil resistance.

Both the subgrade reaction method and the $p-y$ curve method employs the assumption that the pile deflection and internal forces can be calculated by use of the Winkler model approach. In this approach the pile is modelled as an elastic beam on an elastic foundation. The beam is supported by a series of uncoupled springs with spring stiffness given by the $p-y$ curves. Because the springs are considered uncoupled the continuity of the soil is not taken into account. (Fan and Long, 2005)

4. In the elasticity method the continuity of the soil is taken into account but the response of the soil is assumed to be only elastic. Because soil behaves elasto-plastic this method is only valid for small strains, i.e. the method is not valid for predicting the ultimate soil resistance. (Fan and Long, 2005)

5. When using numerical modelling soil continuity, elasto-plastic behaviour, pile-soil interface behaviour, and 3D boundary conditions can be taken into account. Of public available programs, which can be used for 3D modelling of soil, can be mentioned the FE based programs ABAQUS and PLAXIS as well as the finite difference program FLAC^{3D}. Because of the complexity of a 3D model, substantial computer power is needed and the calculations are often very time consuming. Further, the accuracy of the model is highly dependent on the constitutive soil model applied and the calibration of this.

1.2.1 Current Design Method: *p–y* Curves

Due to the simplicity and reasonable accuracy, the $p-y$ curve method is the most widely used method for analysing laterally loaded piles and the method is employed in the offshore design regulations API (1993) and DNV (1992). The method uses the Winkler model approach, which is illustrated in Fig. 1.4.

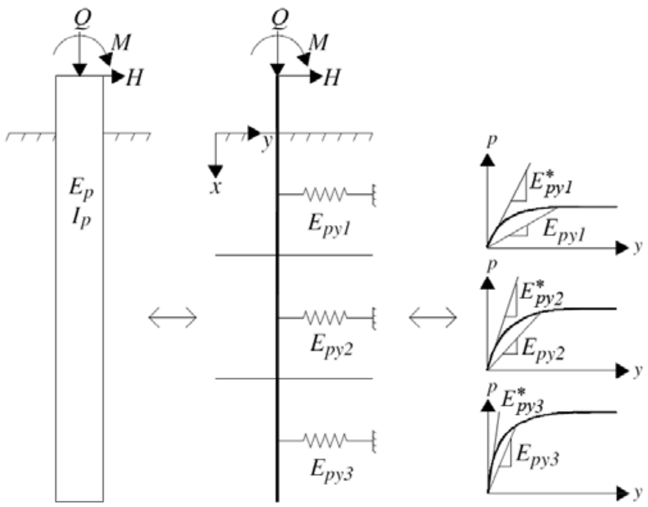

Figure 1.4: Winkler model approach and definitions of *p-y* curves. After Sørensen et al. (2009)

For sand, the employed $p-y$ curve formulation in API (1993) and DNV (1992) is given by Eq. 1.1.

$$p(y) = A \cdot p_c \cdot \tanh\left(\frac{k \cdot x}{A \cdot p_u}\right) \tag{1.1}$$

Where:

$p(y)$	is the soil resistance at a given depth x [F/L]
A	is a factor accounting for static or cyclic loading conditions [-]
p_c	is the theoretical ultimate soil resistance [F]
x	is the depth measured below soil surface [L]
y	is the lateral deflection [L]
k	is the initial modulus of subgrade reaction [F/L^3]
E^*_{py}	is the initial stiffness of the p-y curve [F/L^2]

The spring stiffness, E_{py}, denotes the modulus of subgrade reaction and is given as the secant modulus of the $p-y$ curve. When $y = 0$ E_{py} is equal to the initial stiffness, $E^*_{py} = k \cdot x$. In API (1993) and DNV (1992) k is determined based on the internal angle of friction or relative density of the sand. Hence, the initial stiffness of the $p-y$ curve is assumed independent of the pile properties.

1.2.2 Shortcomings in the *p–y* Curve Method

The $p-y$ curves is designed primarily to evaluate the ultimate lateral capacity of piles used as foundation of offshore platforms. Because of this, the initial stiffness of the $p-y$ curves has not been given much attention and the it is considered independent of the pile properties, e.g. the pile diameter. As described in the previous section the demands for the serviceability and the eigenfrequencies of the system are very strict when designing offshore wind turbines. Hence, the initial stiffness of the $p-y$ curves is very important for the design of the monopiles for the offshore wind turbines.

The $p-y$ curve method is based on a few large scale tests on two slender piles with slenderness ratio, L/D, of 34.4, where L is the embedded length and D is the pile diameter. These piles behaved flexible when subjected to lateral loads. The monopiles used for offshore wind turbine foundations today have a slenderness ratio less than 10 which causes the pile to behave more rigidly, cf. Fig. 1.5. Thus, the design method is used outside its verified range in the current design of monopiles.

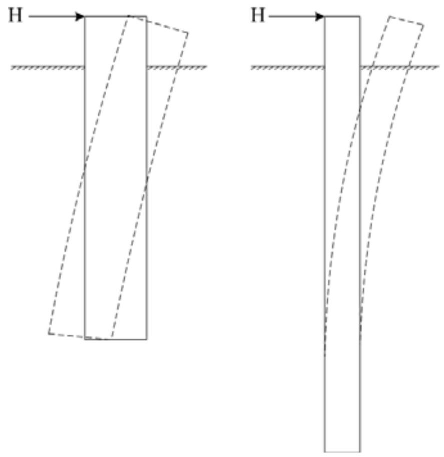

Figure 1.5: Behaviour of non-slender and slender pile.

1.3 Aim of the Thesis

The aim of the thesis is to evaluate the diameter effect on the initial stiffness of the $p-y$ curves for piles with a slenderness ratio $L/D < 10$, i.e. piles corresponding to the monopiles used in the offshore wind industry today. The piles are expected to behave rigidly when subjected to lateral loading.

The evaluation is based on six small-scale tests with piles installed in sand. The tests are conducted on two aluminium pipe piles with outer diameters of 40 mm and 100 mm, respectively, a slenderness ratio of 5 and a wall thickness of 5 mm.

The piles are instrumented with displacement transducers located above the soil surface, and a static lateral load is applied to the piles. Thereby, load-deflection relationships are obtained at the three levels above the soil surface. The tests are conducted with various overburden pressures in order to increase the stress level in soil. The tests are conducted in addition to six similar small-scale tests conducted by Sørensen et al. (2009) on piles with diameters of 60 mm and 80 mm, and a slenderness ratio of 5.

To achieve $p-y$ curves the tests are modelled in the finite difference program FLAC^{3D} with the correct pile and soil properties. The models are calibrated by means of the load-deflection relationships obtained in the laboratory tests. The computed $p-y$ curves are compared to the $p-y$ curves obtained by means of the current design regulations API (1993) and DNV (1992).

Besides the expression for the ultimate soil resistance given in API (1993) other expressions have been derived, e.g. Hansen (1961) and Gwizdala and Jacobsen (1992). The test piles are modelled with a Winkler model approach for which the different expressions for the ultimate soil resistances are evaluated by means of the obtained load-deflection relationships.

The thesis is divided into two papers; one describing and evaluating the laboratory tests and one comparing the test results with results obtained from the FLAC^{3D}-models and current design regulations. An illustration of the evaluation steps are shown in Fig. 1.6.

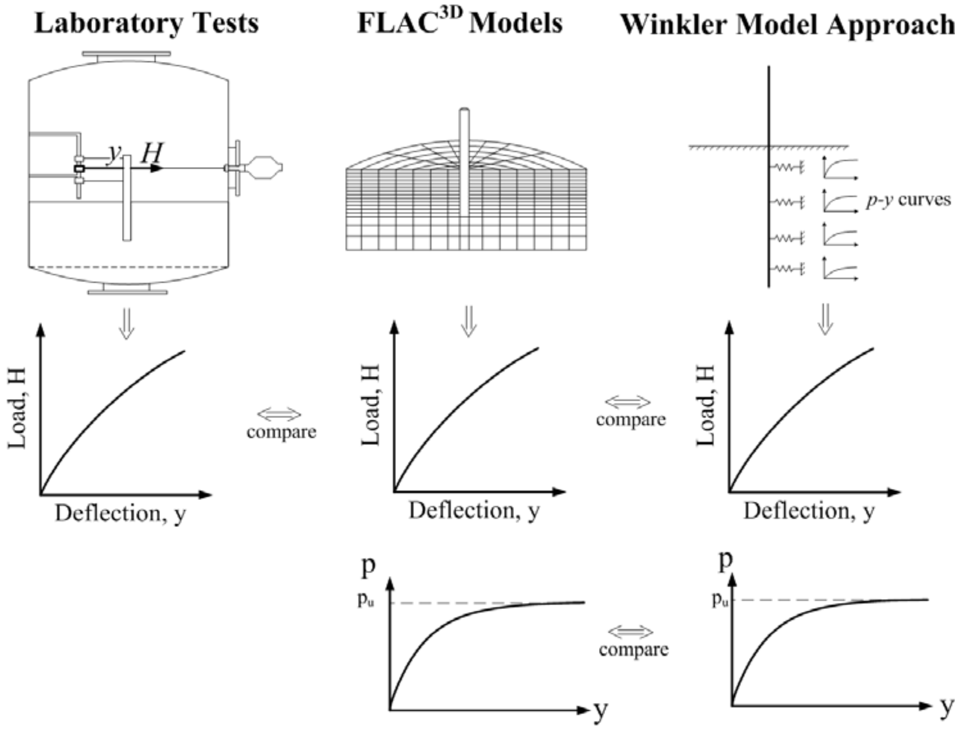

Figure 1.6: Evaluation of diameter effect on $p-y$ curves performed in this thesis.

CHAPTER 2

SMALL-SCALE TESTING OF LATERALLY LOADED NON-SLENDER MONOPILES IN SAND

This chapter contains an article describing six small-scale tests on laterally loaded non-slender monopiles in sand. The aim of of the tests was to evaluate the diameter effect on the pile-soil interaction. The tests were conducted in the Geotechnical Engineering Laboratory at Aalborg University.

Small-Scale Testing of Laterally Loaded Non-Slender Monopiles in Sand

K. Thomassen
H. R. Roesen
L. B. Ibsen
S. P. H. Sørensen

ISSN 1901-726X
DCE Technical Report No. 90

AALBORG UNIVERSITY
Department of Civil Engineering

Aalborg University
Department of Civil Engineering
Division of Water and Soil

DCE Technical Report No. 90

Small-Scale Testing of Laterally Loaded Non-Slender Monopiles in Sand

by

K. Thomassen
H. R. Roesen
L. B. Ibsen
S. P. H. Sørensen

June 2010

Scientific Publications at the Department of Civil Engineering

Technical Reports are published for timely dissemination of research results and scientific work carried out at the Department of Civil Engineering (DCE) at Aalborg University. This medium allows publication of more detailed explanations and results than typically allowed in scientific journals.

Technical Memoranda are produced to enable the preliminary dissemination of scientific work by the personnel of the DCE where such release is deemed to be appropriate. Documents of this kind may be incomplete or temporary versions of papers—or part of continuing work. This should be kept in mind when references are given to publications of this kind.

Contract Reports are produced to report scientific work carried out under contract. Publications of this kind contain confidential matter and are reserved for the sponsors and the DCE. Therefore, Contract Reports are generally not available for public circulation.

Lecture Notes contain material produced by the lecturers at the DCE for educational purposes. This may be scientific notes, lecture books, example problems or manuals for laboratory work, or computer programs developed at the DCE.

Theses are monograms or collections of papers published to report the scientific work carried out at the DCE to obtain a degree as either PhD or Doctor of Technology. The thesis is publicly available after the defence of the degree.

Latest News is published to enable rapid communication of information about scientific work carried out at the DCE. This includes the status of research projects, developments in the laboratories, information about collaborative work and recent research results.

Published 2010 by
Aalborg University
Department of Civil Engineering
Sohngaardsholmsvej 57,
DK-9000 Aalborg, Denmark

Printed in Aalborg at Aalborg University

ISSN 1901-726X
DCE Technical Report No. 90

Small-Scale Testing of Laterally Loaded Non-Slender Monopiles in Sand

K. Thomassen[1]; H. R. Roesen[1]; L. B. Ibsen[2]; and S. P. H. Sørensen[3]

Aalborg University, June 2010

Abstract

In current design of offshore wind turbines, monopiles are often used as foundation. The behaviour of the monopiles when subjected to lateral loading has not been fully investigated, e.g. the diameter effect on the soil response. In this paper the behaviour of two non-slender aluminium piles in sand subjected to lateral loading are analysed by means of small-scale laboratory tests. The six quasi-static tests are conducted on piles with diameters of 40 mm and 100 mm and a slenderness ratio, L/D, of 5. In order to minimise scale effects, the tests are carried out in a pressure tank at stress levels of 0 kPa, 50 kPa, and 100 kPa, respectively. From the tests load-deflection relationships of the piles at three levels above the soil surface are obtained. The load-deflection relationships reveal that the uncertainties of the results for the pile with diameter of 40 mm are large due to the small soil volume activated during failure. From the load-deflection relationships normalised as $H/(L^2D\gamma')$ and y/D indicates that the lateral load, H, is proportional to the embedded length square times the pile diameter, L^2D. Furthermore, by comparing the normalised load-deflection relationships for different stress levels it is seen that small-scale tests with overburden pressure applied is preferable.

1 Introduction

In the design of laterally loaded monopiles the $p-y$ curve method given in the design regulations API (1993) and DNV (1992) is often used. For piles in sand the recommended $p-y$ curves are based on results from two slender, flexible piles with a slenderness ratio $L/D = 34.4$ where L is the embedded length and D is the diameter. Contrary to the assumption of flexible piles for these curves the monopile foundations installed today has a slenderness ratio $L/D < 10$, and behaves almost as rigid objects. The recommended curves does not take the effect of the slenderness ratio into account. Furthermore, the initial stiffness is considered independent of the pile properties such as the pile diameter. The research within the field of diameter effects gives contradictory conclusions. Different studies have shown the initial stiffness to be either independent, linearly dependent, or non-linear dependent on the pile diameter, cf. Brødbæk et al. (2009).

This paper evaluates the effects of the pile diameter on the soil resistance through six small-scale tests.

[1]Graduate Student, Dept. of Civil Engineering, Aalborg University, Denmark.

[2]Professor, Dept. of Civil Engineering, Aalborg University, Denmark.

[3]PhD Fellow, Dept. of Civil Engineering, Aalborg University, Denmark.

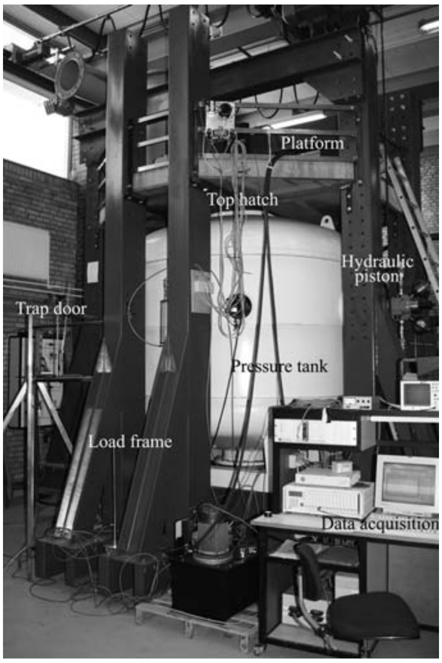

Figure 1: The pressure tank installed in the Geotechnical Engineering Laboratory at Aalborg University, Denmark.

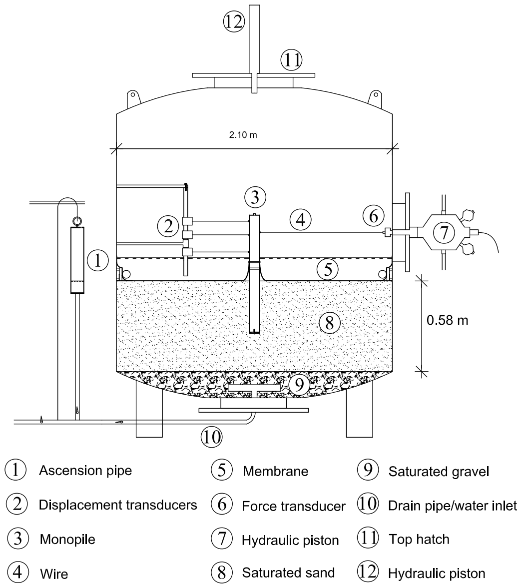

Figure 2: Cross sectional view of the pressure tank and the test setup.

2 Test Programme

Scale effects occur when conducting small-scale tests in sand at 1 g. At low stress levels the soil parameters, in particular the internal angle of friction, will vary strongly with the effective stresses. Therefore, it is an advantage to increase the effective stresses to a level where the internal angle of friction is independent of the stress variations. This increase in stresses will minimise the fluctuations of the measurements as well. To make the increase in stress level possible the tests are conducted in a pressure tank, cf. Fig. 1.

The tests are carried out at stress levels of 0 kPa, 50 kPa, and 100 kPa, and the results are presented in this paper. The tests are quasi-static tests on two closed-ended aluminium pipe piles with outer diameters of 40 mm and 100 mm and a slenderness ratio of 5, corresponding to embedded lengths of 200 mm and 500 mm, respectively. The wall thickness of the piles is 5 mm.

The test programme, cf. Tab. 1, is designed to investigate the soil resistance dependency of the pile diameter at different stress levels. The pile diameters in the test programme are chosen to supplement the tests described in Sørensen et al. (2009) where piles with diameters of 60 mm and 80 mm were tested. To some extent the results from these tests are included in this paper.

Table 1: The test programme.

	D [mm]	L/D [-]	P_0 [kPa]
Test 1	100	5	0
Test 2	100	5	50
Test 3	100	5	100
Test 4	40	5	0
Test 5	40	5	50
Test 6	40	5	100

Figure 3: The 40 mm pile installed in the sand in the pressure tank.

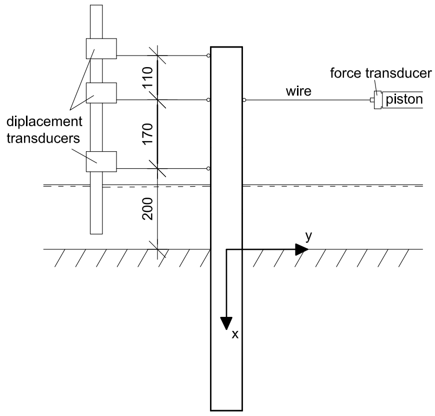

Figure 4: Setup for measuring the lateral deflection of the pile at three levels. The measurements are given in mm.

3 Tests in Pressure Tank

The tests are carried out in a pressure tank installed in the Geotechnical Engineering Laboratory at Aalborg University, Denmark, cf. Fig. 1. The tank has a height of 2.5 m and a diameter of 2.1 m. The tank is placed in a load-frame on a reinforced foundation separated from the rest of the floor in the laboratory.

3.1 Test Setup

Inside the tank a 0.58 m thick layer of fully saturated sand with a layer of highly permeable gravel underneath was located. A cross sectional view of the pressure tank and test setup can be seen in Fig. 2.

The test piles were installed in the sand layer, cf. Fig. 3. A lateral load was applied by means of a wire connected in series to a hydraulic piston through a force transducer. The deflection of the piles was measured by displacement transducers attached in three different levels above soil surface, cf. Fig. 4 and Fig. 5. Thereby, three load-deflection relationships were obtained. To make the soil preparation and pile installation possible the platform mounted on top of the pressure tank, cf. Fig. 1, was used.

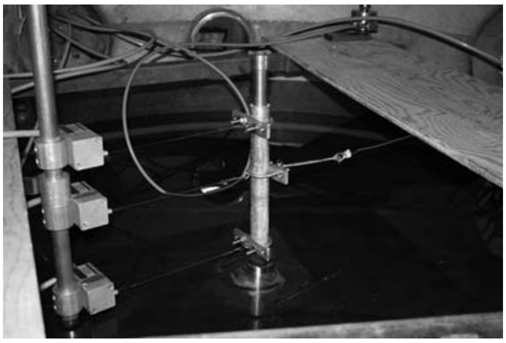

Figure 5: The 40 mm pile instrumented with three displacement transducers.

3.2 Increase of the Effective Stresses

The increase of the effective stresses in the soil was obtained by placing an elastic, rubber membrane on the soil surface. The membrane was sealed around the pile and against the side of the tank causing the fully saturated soil to be sealed from the air in the upper part of the tank, cf. Fig. 6. Water was poured in on top of the membrane to ensure fully saturated sand even if there were small gabs in the membrane or in the sealing between membrane and tank. Moreover, the dynamic viscosity of water is approximately 55 times greater than of air, and thereby the water minimised the flow through gabs.

Figure 6: The membrane placed on the soil surface and sealed around the pile by hose clips and sealed against the side of the tank by a fire hose.

Figure 7: The openings in the tank hermetically sealed.

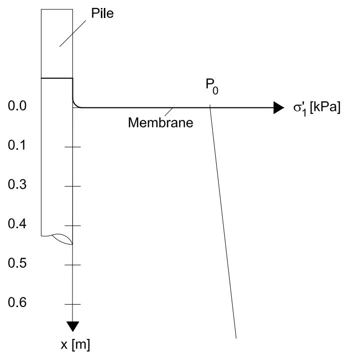

Figure 8: Variation of effective vertical stresses.

Figure 9: The ascension pipe connected to the tank to maintain hydrostatic pore pressure in the soil during the tests.

The effective stresses were then increased by closing the openings in the tank, as shown in Fig. 7, and applying an air pressure of 50 kPa and 100 kPa, respectively. Because the pressure in the upper part of the tank made the membrane resemble an applied surface load, a homogeneous increase of the effective stresses was obtained.

3.3 Hydrostatic Pore Pressure

To maintain a hydrostatic pore pressure in the soil, an ascension pipe was connected to the tank and, thereby, the water flowing through the gabs was led out of the tank. This way the soil remained fully saturated and the stresses were applied as effective stresses only. The variation of the effective vertical stresses in the soil layer is shown in Fig. 8, where P_0 denotes the applied overburden pressure. The ascension pipe can be seen in Fig. 9.

4 Measuring System

The hydraulic piston used to actuate the pile was controlled by a predefined displacement and it acted at a vertical eccentricity of 370 mm above the soil surface, cf. Fig. 4. The force transducer connecting the wire and the hydraulic system in series, cf. Fig. 2 6, was a HBM U2B 10 kN for tests on the 40 mm pile and a HBM U2B 20 kN for the 100 mm pile.

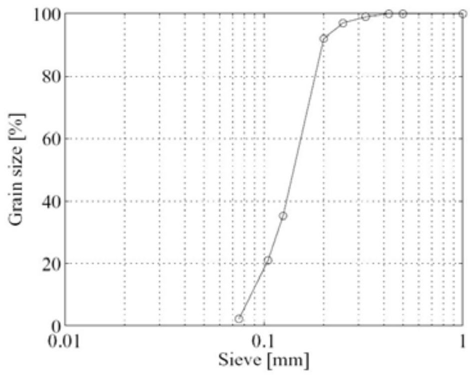

Figure 10: Distribution of Baskarp Sand No. 15 found by sieve analysis. (Ibsen and Bødker, 1994)

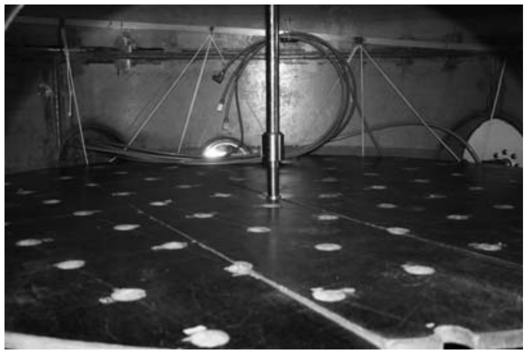

Figure 11: The pile fixed by the hydraulic piston.

The displacement transducers, cf. Fig. 2 ②, were of the type WS10-1000-R1K-L10 from ASM GmbH. For measuring the pressure in the tank a HBM P6A 10 bar absolute pressure transducer was employed in the first test, and a HBM P3MBA 5 bar absolute pressure transducer was employed in the remaining tests reducing the fluctuations of the measurements. The sampling frequency was 10 Hz.

5 Soil conditions

The sand used in the tank was Baskarp Sand No. 15. The material properties for Baskarp Sand No. 15 are well-defined from previous tests in the laboratory at Aalborg University. A representative distribution of the grains found by sieve analysis is shown in Fig. 10. The uniform grading of the grains makes it possible to obtain a homogeneous compaction of the soil. The hydraulic conductivity is $k \approx 6 \cdot 10^{-5}$ m/s. The loading velocity was $1 \cdot 10^{-5}$ m/s, thus, the soil was considered drained during the tests. The material properties are given in Tab. 2.

Table 2: Material properties for Baskarp Sand No. 15. (Andersen et al., 1998)

Specific grain density d_s [-]	2.64
Maximum void ratio e_{max} [-]	0.858
Minimum void ratio e_{min} [-]	0.549
d_{50} = 50%-quantile [mm]	0.14
$U = d_{60}/d_{10}$ [-]	1.78

5.1 Soil preparation

Prior to each test the soil was loosened by an upward gradient of 0.9. Hereafter, it was vibrated mechanically to ensure fully saturated soil and a homogeneous compaction.

The pile was installed in the centre of the tank. During installation, a gradient of 0.9 was applied to minimise the pressure on the closed end of the pile. Hereby, the toe resistance and the skin friction along the pile were minimised. After installation the soil was vibrated mechanically, cf. Fig. 12, to minimise disturbances in the soil emerged from the pile installation. While vibrating the pile was secured in its upright position by means of the hydraulic piston mounted through the top hatch of the tank, cf. Fig. 2 ⑪ and Fig. 11.

To control the homogeneity and the compaction of the soil, cone penetration tests (CPT) were conducted. The setup of the CPT-device can be seen in Fig. 13. A total

Figure 12: Vibration of the soil.

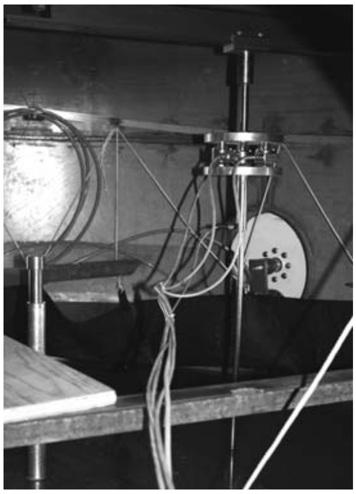

Figure 13: The setup of the CPT-device in the pressure tank.

of six CPT's were conducted prior to each test. Four were conducted in a distance of 500 mm from the centre of the pile, cf. Fig. 14. The remaining two CPT's were conducted 160 mm and 200 mm from the pile centre for the 40 mm and the 100 mm pile, respectively. Both were conducted on the neutral side of the pile. The probe diameter of the CPT-devise was 15 mm.

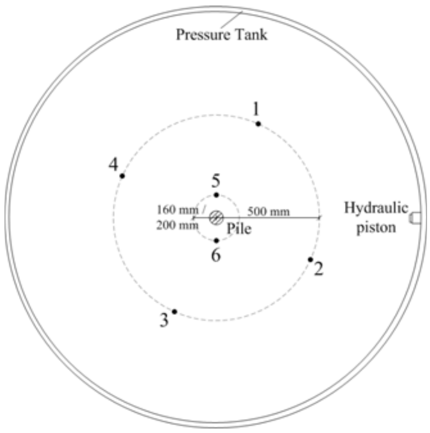

Figure 14: The positions of the six CPT's conducted prior to each test.

In Fig. 15 the cone resistance of the CPT's conducted prior to test 5 shows a homogeneous compaction of the soil. In Fig. 16 the mean value of the cone resistance, q_c, prior to each of the six tests described in this paper and the cone resistances obtained prior to the tests described in Sørensen et al. (2009) can be seen. The figure shows that the cone resistance of the soil was approximately the same for the six tests conducted on the 40 mm pile and the 100 mm pile. Though, compared to the CPT's conducted in Sørensen et al. (2009) they were higher.

In Tab. 3 the soil parameters derived on basis of the CPT's are presented. The parameters are derived in accordance to Ibsen et al. (2009), cf. Eqs. 1 to 5. The formulation for the tangential modulus of elasticity, E_0 cf. Eq. 6, is given by Brinkgreve and Swolfs (2007).

$$\varphi_{tr} = 0.152 \cdot I_D + 27.39 \cdot \sigma_3'^{-0.2807} + 23.21 \tag{1}$$

$$\psi_{tr} = 0.195 \cdot I_D + 14.86 \cdot \sigma_3'^{-0.09764} - 9.946 \tag{2}$$

$$I_D = c_2 \left(\frac{\sigma_1'}{(q_c)^{c_1}} \right)^{c_3} \tag{3}$$

$$\gamma' = \frac{d_s - 1}{1 + e_{in\text{-}situ}} \gamma_w \tag{4}$$

$$E_{50} = \left(0.6322 \cdot I_D^{2.507} + 10920\right) \cdot \left(\frac{c \cdot \cos\varphi_{tr} + \sigma_3' \cdot \sin\varphi_{tr}}{c \cdot \cos\varphi_{tr} + \sigma_3'^{\,ref} \cdot \sin\varphi_{tr}} \right)^{0.58} \tag{5}$$

$$E_0 = \frac{2 \cdot E_{50}}{2 - R_f} \tag{6}$$

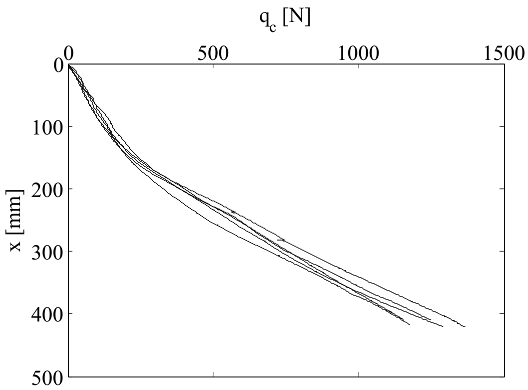

Figure 15: The cone resistance, q_c, from the CPT's conducted prior to test 5.

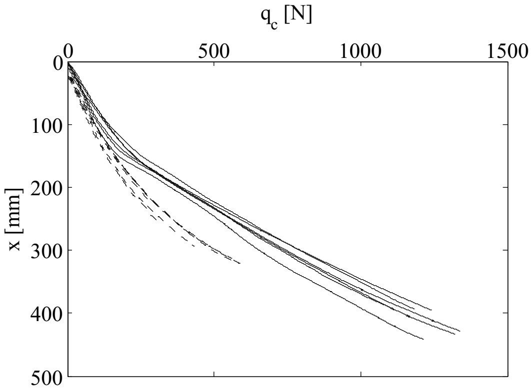

Figure 16: Mean values of the cone resistance, q_c, prior to each test. The solid curves are q_c obtained prior to the tests described in this paper. The dashed curves are q_c obtained prior to the tests described in Sørensen et al. (2009).

φ_{tr} is the internal angle of friction, I_D is the identity index, σ'_3 and σ'_1 are the effective horizontal and vertical stresses, respectively, and ψ_{tr} is the dilation angle. (c_1, c_2, c_3) = (0.75, 5.14, -0.42), γ' is the effective unit weight of the soil, d_s is the relative density of the soil, $e_{in\text{-}situ}$ is the insitu void ratio, and γ_w is the unit weight of water. E_{50} and secant is the modulus of elasticity, c is the cohesion, and R_f is the failure ratio, which is normally set to 0.9.

By comparing the obtained parameters to the ones derived in Sørensen et al. (2009), given in Tab. 4, it can be seen that the identity indeces, I_D, derived for the present tests are approximately 10 % higher. Because the internal angle of friction, φ_{tr}, and the effective unit weight of the soil, γ', are dependent on I_D these parameters are slightly higher as well. The tangential modulus of elasticity, E_0, is not calculated for the tests without overburden pressure because the low stress level leads to large uncertainties in the determination.

Table 3: Material properties determined from the CPT's conducted prior to the six tests.

D [mm]	P_0 [kPa]	φ_{tr} [°]	ψ_{tr} [°]	I_D [−]	γ' [kN/m^3]	E_0 [MPa]
100	0	53.8	19.6	0.86	10.3	-
100	50	50.3	19.0	0.89	10.4	38.2
100	100	47.7	18.3	0.90	10.4	55.6
40	0	54.4	20.4	0.91	10.4	-
40	50	50.4	19.1	0.89	10.4	38.6
40	100	48.0	18.6	0.91	10.4	57.2

Table 4: Material properties determined from the CPT's conducted prior to the six tests conducted in Sørensen et al. (2009).

D [mm]	P_0 [kPa]	φ_{tr} [°]	ψ_{tr} [°]	I_D [-]	γ' [kN/m^3]	E_0 [MPa]
60	0	52.6	18.1	0.79	10.2	-
60	50	48.5	16.9	0.79	10.2	25.4
60	100	45.9	16.2	0.79	10.2	41.1
80	0	52.2	17.5	0.76	10.1	-
80	50	48.3	16.7	0.78	10.1	24.9
80	100	45.1	15.3	0.75	10.1	37.4

6 Results

During the tests, prescribed displacements were applied to the pile and, thereby, the soil was brought to failure, then unloaded and reloaded. Hereby, an estimation of the ultimate soil resistance and the elastic behaviour of the soil can be obtained.

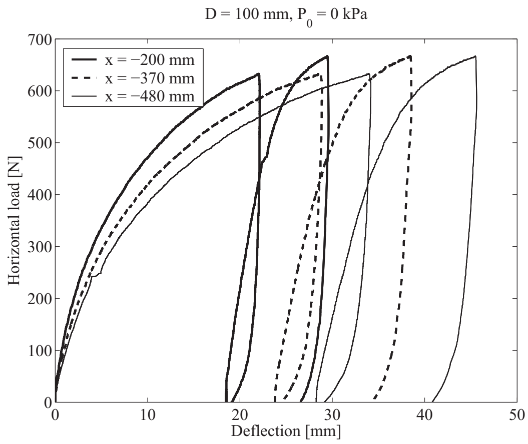

Figure 17: Load-deflection relationships for the 100 mm pile at P_0 = 0 kPa.

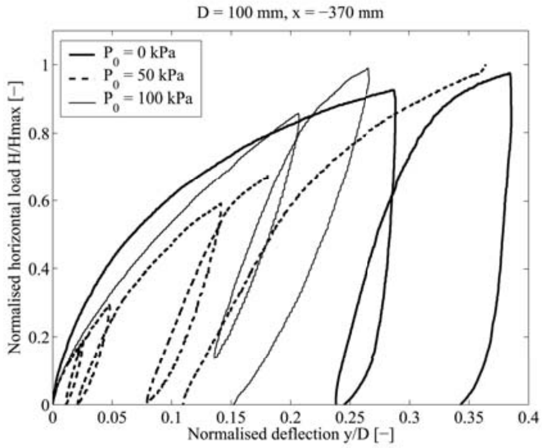

Figure 18: Normalised relationships between load (H/H_{max}) and deflection (y/D) measured at the height of the hydraulic piston (x = -370 mm) for the 100 mm pile.

In Fig. 17 the load-deflection relationships for test 4 are shown. Firstly, it can be seen that, when unloading and reloading, the load-deflection curves reaches the original curves. Secondly, the upper displacement transducer recorded the largest deflection, while the lower transducer recorded the smallest. This is in agreement with the expected results.

The normalised relationships between load, H/H_{max}, and deflection, y/D, at the level of the hydraulic piston ($x = -370$ mm) for test 1 to 3 are shown in Fig. 18. The test without overburden pressure gives a more curved graph than the tests with overburden pressures. This is caused by the low stress level, at which the dilation of the soil is larger.

6.1 Plastic Response and Pile Capacity

The plastic behaviour of the soil depends on the applied overburden pressure. For the case without overburden pressure the plastic deformation after the first unloading is approximately 85 % of the total deformation after the first loading. For the cases were overburden pressures of 50 kPa and 100 kPa were applied the plastic deformation is 50 % and 60 %, respectively, of the total deformation after the first loading, cf. Fig. 18.

In Fig. 18 it can be observed that several loading-reloading curves are present for the test at 50 kPa. The reason for this deviation compared to the remaining tests is that the test was run in three stages because of problems with the wire transferring the load to the pile. During the first run the wire was dragged out of its bracket. Therefore, the applied displacement was obtained in the extension of the wire, which resulted in very small deflections of the pile. During the second run the wire deformed, again leading to small deflections of the pile. A last run was conducted and the wanted deflection of the pile was obtained.

Figs. 19 and 20 present the dependency of the overburden pressure on the lateral load. As expected, the capacity of the soil increases with increasing overburden pressure. The difference between the lateral load for the tests without overburden pressure compared to the ones with overburden pressures of 50 kPa and 100 kPa, respectively, is determined for 10 mm de-

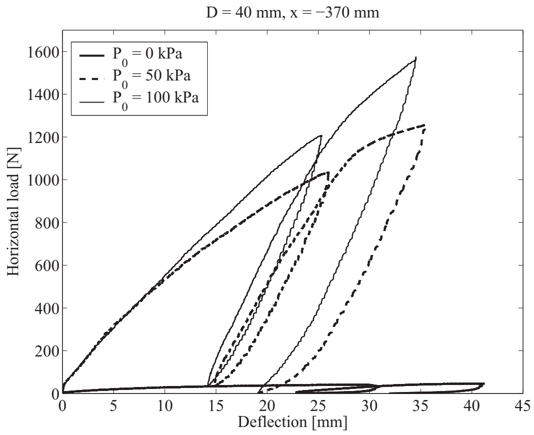

Figure 19: Load-displacement relationships at different overburden pressures measured at the level of the hydraulic piston ($x = -370$ mm) for the 40 mm pile.

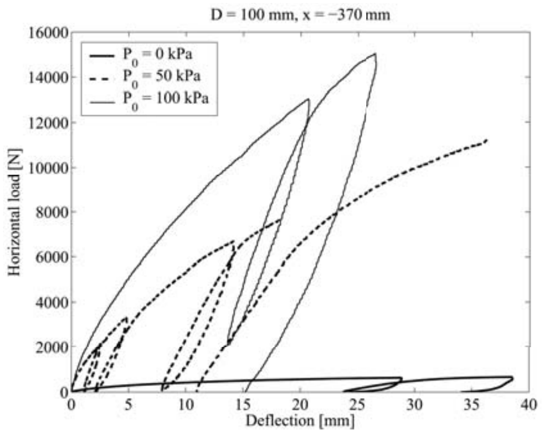

Figure 20: Load-displacement relationships at different overburden pressures measured at the level of the hydraulic piston ($x = -370$ mm) for the 100 mm pile.

flection at the level of the hydraulic piston, i.e. $x = -370$ mm. The lateral load increases with a factor of 17 for the 40 mm pile for 50 kPa and 15 for the 100 mm pile. For 100 kPa the load increases with a factor of 18 and 20 for the 40 mm pile and the 100 mm pile, respectively.

6.2 Uncertainties for the 40 mm Pile

Conducting tests on the 40 mm pile was difficult because little disturbance of the soil would cause large uncertainties for the obtained results due to the small soil volume activated during failure. Fig. 19 shows the load-deflections relationship for the 40 mm pile. The figure shows an unexpected appearance of the graph for the test at 100 kPa as the graph for the first loading describes nearly a straight line. Before this test the pile got stuck in the hydraulic piston and when releasing it the surrounding soil was disturbed. This disturbance might have caused a decrease of the strength in the soil. Thereby, the graph is straight till the point where the pile obtained a deflection large enough to activate the undisturbed soil further away from the pile. Therefore, the results from test 6 are not considered to represent the correct behaviour of an undisturbed soil.

6.3 Comparison of Test Results

In Fig. 21 the results for the tests without overburden pressure are compared to the results obtained by Sørensen et al. (2009) for 60 mm and 80 mm piles. As expected, the lateral load necessary to obtain a deflection of the pile increases with increasing pile diameter.

Figs. 22, 23, and 24 shows the normalised relationships between the lateral load, H, and the deflection, y, determined at the level of the hydraulic piston for the three stress levels. The normalised formulation for the load, Eq. 7, is chosen because the load is assumed dependent on the soil volume activated during failure, and the stresses in the soil. This assumption provides the expression $LD\sigma'$ that can be rewritten to $LD\gamma' L = L^2 D\gamma'$.

$$\text{Normalised load} = \frac{H}{L^2 D\gamma'} \tag{7}$$

$$\text{Normalised deflection} = \frac{y}{D} \tag{8}$$

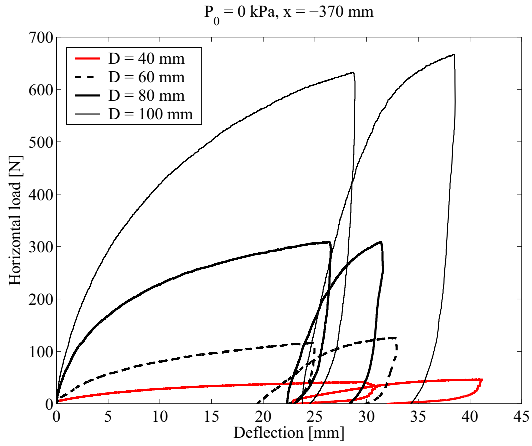

Figure 21: Load-deflection relationships for the four piles at P_0 = 0 kPa.

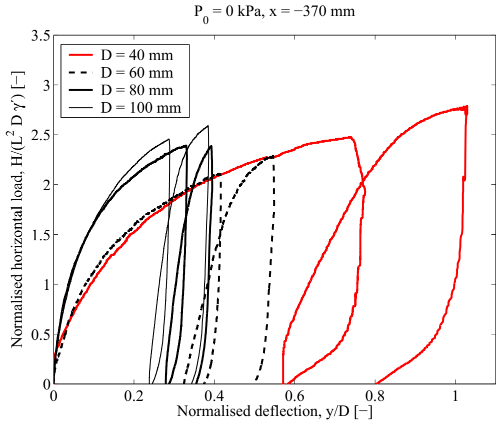

Figure 22: Normalised relationships between load (H/H_{max}) and defection (y/D) measured at the level of the hydraulic piston for the tests at P_0 = 0 kPa.

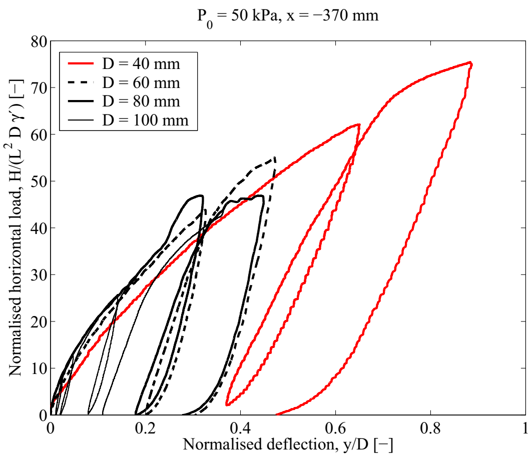

Figure 23: Normalised relationships between load (H/H_{max}) and deflection (y/D) measured at the level of the hydraulic piston for the tests at P_0 = 50 kPa.

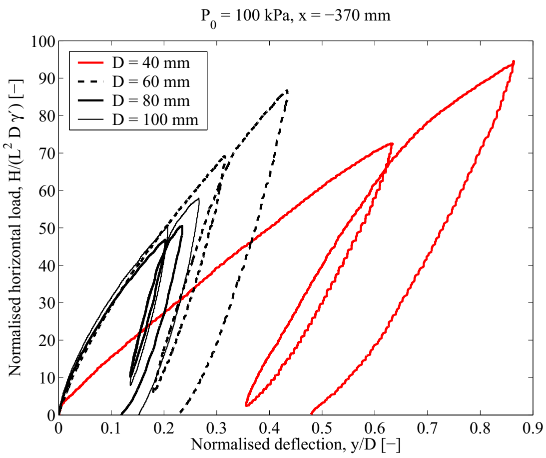

Figure 24: Normalised relationships between load (H/H_{max}) and deflection (y/D) measured at the level of the hydraulic piston for the tests at P_0 = 100 kPa.

Fig. 22 shows deviations between the normalised curves for the four piles without overburden pressure. The curves seems to be grouped in pairs. The 80 mm pile and the 100 mm pile are similar at the initial part of the curves, but deviates at larger deflections. The curves for the 40 mm and the 60 mm pile are similar, but this might be caused by the fact that the identity index for the soil was approximately 10 % larger for the test on the 40 mm pile than for the test on the 60 mm pile, cf. Tabs. 3 and 4.

The reason for the deviations could be the diffenrece in the soil volume activated during failure and the different embedded lengths for the four piles, which causes deviations of the reached stress levels.

In Fig. 23 it can be seen that when applying an overburden pressure of 50 kPa the initial part of the graphs are almost similar. The smaller deviations indicate that the accuracy of the results increases when overburden pressure is applied. For the tests with overburden pressure of 100 kPa the curves are coinciding for the tests on the 60 mm, 80 mm, and 100 mm piles. This implies that the accuracy of the test results increases with increasing overburden pressure. The deviation of the curve for the 40 mm pile is caused by the disturbance of the soil before the test.

In spite of the inaccurate results for the tests without overburden pressure and for the tests of the 40 mm pile, the normalised relationships indicate that the lateral load is proportional to the embedded length squared and the pile diameter, cf. Eq. 7. Furthermore, they indicate that the accuracy of small-scale testing increases with increasing overburden pressure. In future research it is therefore recommended to conduct similar tests with higher overburden pressure applied.

7 Conclusion

The paper presents results from six small-scale quasi-static tests on laterally loaded piles in sand. The aluminium piles had outer diameters of 40 mm and 100 mm, respectively, and a slenderness ratio, L/D, of 5. The tests were conducted in a pressure tank with effective stress levels of 0 kPa, 50 kPa, and 100 kPa.

By increasing the effective stresses in the soil the problems with the non-linear yield surface for small stress levels were avoided. The increase of the effective stress levels were succesfully obtained by separating the sand from the upper part of the tank by an elastic membrane.

The problems with the non-linear yield surface were seen in the results for the tests without overburden pressure, as the curves for the normalised relationships were not similar. The similarity for the normalised results were obtained for the tests with overburden pressure of 100 kPa, and it can be concluded that accuracy in small-scale testing increases with increasing overburden pressure. Therefore, in future research it is recommended to conduct small-scale tests with higher overburden pressure applied.

The uncertainties when conducting tests on the 40 mm pile were high, because small disturbances of the soil led to results in disagreement to the other test results. Thereby, it is difficult to draw reasonable conclusions from these tests. In further research small-scale tests should be conducted on piles with larger diameters.

Both the test results obtained for the 100 mm pile and the test results obtained by Sørensen et al. (2009) indicates that the lateral load acting on the pile is proportional to the embedded length squared times the pile diameter.

8 Acknowlegdements

The project is associated with the EFP programme "Physical and numerical modelling of monopile for offshore wind turbines", journal no. 033001/33033-0039. The funding is sincerely acknowledged.

Bibliography

Andersen, A., Madsen, E. and Schaarup-Jensen (1998), 'Eastern Scheldt Sand, Baskarp Sand No. 15', *Data Report 9701 Part 1* . Geotechnical Engineering Group, Aalborg University.

API (1993), *Recommended Practice for Planning, Designing and Constructing Fixed Offshore Platforms – Working Stress Design*, American Petroleum Institute.

Brødbæk, K., Møller, M., Sørensen, S. and Augustesen, A. (2009), 'Evaluation of p-y relationship in cohesionless soil', *DCE Technical Report No. 57* . Aalborg University.

Brinkgreve, R. B. J. and Swolfs, W., eds (2007), *PLAXIS 3D FOUNDATION, Material Models manual, Version 2*, PLAXIS b.v.

DNV (1992), *Foundations*, Det Norske Veritas. Classification Notes No. 30.4.

Ibsen, L. B., Hanson, M., Hjort, T. and Thaarup, M. (2009), 'MC-Parameter Calibration for Baskarp Sand No. 15', *DCE Technical Report No.62* . Department of Civil Engineering, Aalborg University.

Ibsen, L. and Bødker, L. (1994), 'Baskarp Sand No. 15', *Data Report 9301* . Geotechnical Engineering Group, Aalborg University.

Sørensen, S., Brødbæk, K., Møller, M., Augustesen, A. and Ibsen, L. (2009), 'Evaluation of the Load-Displacement Relationships for Large-Diameter Piles in Sand', *Civil-Comp Press* . Paper 244.

Recent publications in the DCE Technical Report Series

Brødbæk, K. T., Møller, M., Sørensen, S. P. H. and Augustesen, A. H. (2009) *Review of p-y relationships in cohesionless soil*, DCE Technical Report No. 57, Aalborg University. Department of Civil Engineering

Sørensen, S. P. H., Møller, M., Brødbæk, K. T., Augustesen, A. H. and Ibsen, L. B. (2009) *Evaluation of Load-Displacement Relationships for Non-Slender Monopiles in Sand*, DCE Technical Report No. 79, Aalborg University. Department of Civil Engineering

Sørensen, S. P. H., Møller, M., Brødbæk, K. T., Augustesen, A. H. and Ibsen, L. B. (2009) *Numerical Evaluation of Load-Displacement Relationships for Non-Slender Monopiles in Sand*, DCE Technical Report No. 80, Aalborg University. Department of Civil Engineering

ISSN 1901-726X
DCE Technical Report No. 90

CHAPTER 3

EVALUATION OF SMALL-SCALE LATERALLY LOADED NON-SLENDER MONOPILES IN SAND

This chapter contains an article evaluating the diameter effect on the pile-soil interaction by means of the six-small scale tests described in Chap. 2, numerical models of the same test-setup, and existing theory. The laboratory tests are modelled by means of the finite difference program FLAC^{3D} and the existing theory is incorporated in a Winkler model approach.

Evaluation of Small-Scale Laterally Loaded Non-Slender Monopiles in Sand

H. R. Roesen
K. Thomassen
S. P. H. Sørensen
L. B. Ibsen

ISSN 1901-726X
DCE Technical Report No. 91

AALBORG UNIVERSITY
Department of Civil Engineering

Aalborg University
Department of Civil Engineering
Division of Water and Soil

DCE Technical Report No. 91

Evaluation of Small-Scale Laterally Loaded Non-Slender Monopiles in Sand

by

H. R. Roesen
K. Thomassen
S. P. H. Sørensen
L. B. Ibsen

June 2010

Scientific Publications at the Department of Civil Engineering

Technical Reports are published for timely dissemination of research results and scientific work carried out at the Department of Civil Engineering (DCE) at Aalborg University. This medium allows publication of more detailed explanations and results than typically allowed in scientific journals.

Technical Memoranda are produced to enable the preliminary dissemination of scientific work by the personnel of the DCE where such release is deemed to be appropriate. Documents of this kind may be incomplete or temporary versions of papers—or part of continuing work. This should be kept in mind when references are given to publications of this kind.

Contract Reports are produced to report scientific work carried out under contract. Publications of this kind contain confidential matter and are reserved for the sponsors and the DCE. Therefore, Contract Reports are generally not available for public circulation.

Lecture Notes contain material produced by the lecturers at the DCE for educational purposes. This may be scientific notes, lecture books, example problems or manuals for laboratory work, or computer programs developed at the DCE.

Theses are monograms or collections of papers published to report the scientific work carried out at the DCE to obtain a degree as either PhD or Doctor of Technology. The thesis is publicly available after the defence of the degree.

Latest News is published to enable rapid communication of information about scientific work carried out at the DCE. This includes the status of research projects, developments in the laboratories, information about collaborative work and recent research results.

Published 2010 by
Aalborg University
Department of Civil Engineering
Sohngaardsholmsvej 57,
DK-9000 Aalborg, Denmark

Printed in Aalborg at Aalborg University

ISSN 1901-726X
DCE Technical Report No. 91

Evaluation of Small-Scale Laterally Loaded Non-Slender Monopiles in Sand

H. R. Roesen[1]; K. Thomassen[1]; S. P. H. Sørensen[2]; and L. B. Ibsen[3]

Aalborg University, June 2010

Abstract

In current design of offshore wind turbines, monopiles are often used as foundation. The behaviour of the monopiles when subjected to lateral loading has not been fully investigated, e.g. the diameter effect on the soil response. In this paper the diameter effect on laterally loaded non-slender piles in sand is evaluated by means of results from six small-scale laboratory tests, numerical modelling of the same test setup and existing theory. From the numerical models $p-y$ curves are conducted and compared to current design regulations. It is found that the recommendations in API (1993) and DNV (1992) are in poor agreement with the numerically obtained $p-y$ curves. The initial stiffness, E^*_{py}, of the $p-y$ curves, is found to be dependent on the pile diameter, i.e. the initial stiffness increases with increasing pile diameter. Further, the dependency is found to be in agreement with the suggestions in Sørensen et al. (2010). It is found that considerable uncertainties are related to small-scale testing, and the different evaluations clearly indicate that the accuracy of small-scale testing is increased when increasing the pile diameter and applying overburden pressure.

1 Introduction

In the design of laterally loaded monopiles the $p-y$ curve method, given by the design regulations API (1993) and DNV (1992), is often used. For piles in sand the recommended $p-y$ curves are based on results from two slender, flexible piles with a slenderness ratio of $L/D = 34.4$, where L is the embedded length and D is the diameter of the pile. Contrary to the assumption of flexible piles for these curves the monopile foundations installed today have a slenderness ratio $L/D < 10$, and behave almost as rigid objects. The recommended curves does not take the effect of the slenderness ratio into account. Furthermore, the initial stiffness is considered independent of the pile properties such as the pile diameter. The research within the field of diameter effects gives contradictory conclusions. Different studies have found the initial stiffness to be either independent, linearly dependent, or non-linear dependent on the pile diameter, cf. Brødbæk et al. (2009).

The aim of this paper is to evaluate the diameter effect on the pile-soil interaction. Six small-scale tests on laterally loaded monopiles in sand have been conducted, cf. Thomassen and Roesen (2010). The diameter effect is evaluated by comparing results from these tests with calibrated numerical models of the same test setup and existing theory. Furthermore, $p-y$ curves

[1]Graduate Student, Dept. of Civil Engineering, Aalborg University, Denmark

[2]Professor, Dept. of Civil Engineering, Aalborg University, Denmark.

[3]PhD Fellow, Dept. of Civil Engineering, Aalborg University, Denmark.

recommended in the current design regulations API (1993) and DNV (1992) are compared to curves obtained from the numerical models. As the foundations for offshore wind turbines are sensitive towards rotation and vibrations, strict demands for the stiffness of the foundation are induced. Therefore, the diameter effect is evaluated with focus on the initial stiffness of the $p-y$ curves.

2 Laboratory Test Setup

Six quasi-static tests on two closed-ended aluminium piles with a wall-thickness of 5 mm and outer diameters of 40 mm and 100 mm, respectively, have been conducted. The piles had a slenderness ratio, L/D, of 5 corresponding to embedded lengths of 200 mm and 500 mm. The piles were installed in 580 mm fully saturated sand. The aim of the tests was to obtain load-deflection relationships for the piles. Therefore, the piles were loaded laterally 370 mm above the soil surface, and the deflection of the pile was measured at three levels, cf. Fig. 1.

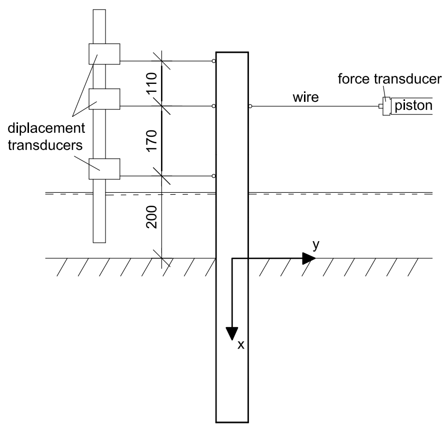

Figure 1: Setup for measuring the lateral deflection of the pile at three levels. The measurements are given in mm.

In order to minimize errors such as small non-measurable stresses and a non-linear failure criterion, the tests were conducted in the pressure tank shown in Fig. 2. The

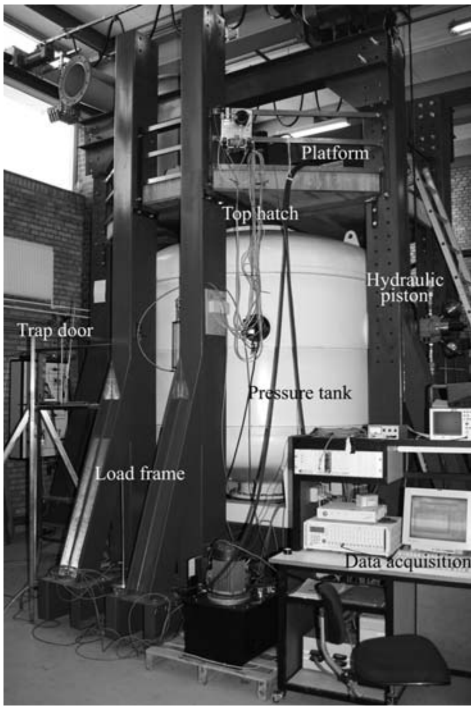

Figure 2: The pressure tank installed in the Geotechnical Engineering Laboratory at Aalborg University, Denmark.

effective stresses in the soil were increased by placing an elastic membrane on the soil surface sealing the soil from the upper part of the pressure tank. When increasing the pressure in the upper part of the tank the membrane was pressed against the soil leading to an increase of the stresses in the soil. The lower part of the tank was connected to an ascension pipe ensuring that the load was applied as contact pressures between the grains only, i.e. an increase of the effective stresses. The tests were conducted at stress levels of 0 kPa, 50 kPa, and 100 kPa.

The soil parameters were determined from cone penetration tests in accordance to Ibsen et al. (2009). A detailed description of the laboratory tests can be found in Thomassen and Roesen (2010).

3 Numerical 3D Models

The six laboratory tests are modelled in FLAC^{3D}, which is a commercial explicit finite difference program. Because of axis symmetry in the tests, only half the test setup is modelled. The modelling programme is chosen to match the testing programme in Thomassen and Roesen (2010), cf. Tab. 1.

Table 1: Modelling programme for the FLAC^{3D} models.

		D [mm]	L/D [-]	P_0 [kPa]
Model 1	(Test 1)	100	5	0
Model 2	(Test 2)	100	5	50
Model 3	(Test 3)	100	5	100
Model 4	(Test 4)	40	5	0
Model 5	(Test 5)	40	5	50
Model 6	(Test 6)	40	5	100

The generation of the models and the finite difference calculations are carried out stepwise as described in the following.

3.1 Geometry of the 3D Models

The model geometry is set to match the condition in the pressure tank. Therefore, the outer boundaries are given as the volume of the soil mass in the tank, i.e. a diameter of 2.1 m and a soil depth of 0.58 m. The soil and pile are generated by use of predefined zone elements to which different material models and properties can be assigned. Each zone element is automatically discritised into five tetrahedron subelements, which are first order, constant rate of strain elements. Because large variations in strain and stresses occur in the soil near the pile a finer zone mesh is generated in this area.

In order to model a correct pile-soil interaction an interface is generated between the pile and the soil by use of standard FLAC^{3D} interface elements. The elements are triangular and by default two interface elements are generated for each zone face. The interfaces are one-sided and attached to the soil. The constitutive model for the interface is defined by a linear Coulomb shear-strength criterion that limits the shear force acting at an interface node after the shear strength limit is reached.

Firstly, the soil is generated, secondly, the interface is generated and attached to the soil elements and, thirdly, the pile is generated. Initially, the pile grid is generated separately and later moved into the soil and in contact with the interface. Hereby, it is possible to group the pile elements and specify pile nodes for the computation of bending moment. As a simplification, the piles are modelled as solid cylinders in contrast to the closed-ended pipe piles used in the laboratory tests. The solid piles are modelled with a reduced modulus of elasticity and reduced density based on equivalence with the pipe piles used in the laboratory tests, cf. Sec. 3.5. The zone geometry for the 100 mm pile is shown in Fig. 3. Note that the shown coordinate system is in agreement with the coordinate system employed for laterally loaded piles in the design regulations and does not represent the system used in FLAC^{3D}.

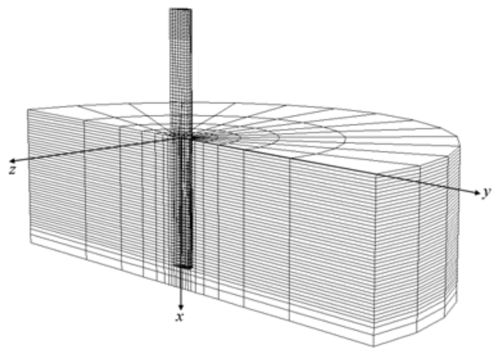

Figure 3: Zone geometry in the models with the 100 mm pile.

3.2 Boundary and Initial Conditions

When the geometry is generated the boundary and initial conditions are assigned. At the outer perimeter of the soil the element nodes are restrained in the y- and z-direction, cf. Fig. 3. At the bottom surface of the model the nodes are restrained in all directions. Because only half the laboratory setup is modelled the nodes at the symmetry line are restrained in the z-direction.

The initial stresses are initialised based on the density of the material, the gravitational loading, and the overburden pressure. The horizontal stresses are generated by use of a K_0-procedure in which $K_0 = 1 - \sin\varphi_{tr}$.

3.3 Calculation Phase

In order to prevent stress concentrations near the pile the model is brought to equilibrium with both the pile and the soil having the material properties of the soil. Further, the pile is assumed smooth by setting the interface friction equal to zero. Hereafter, the pile and interface are assigned the material properties for the pile and interface, respectively, cf. Sec. 3.5. Again, the model is brought to equilibrium. This second equilibrium ensures a correct generation of the initial interface stresses. When equilibrium is reached all displacements are reset to zero.

The lateral load is applied as lateral velocities at $x = -370$ mm. The velocities are applied to the nodes at the centre of the pile corresponding to $y = 0$. Hereby, no additional bending moment is introduced in the pile. In order to avoid a dynamic response of the system the velocity is applied in small increments.

During the calculations the total lateral force, H, and the displacement, y, along the pile are recorded. The bending moment, M, and soil pressure, p, are calculated based on the recorded stresses in the pile and the interface, respectively, cf. Sec. 3.6.

3.4 Material Models

To describe the constitutive relations in the soil an elasto-plastic Mohr-Coulomb model is employed. As the soil is considered cohesionless no tension forces are allowed. Thus, tension cut-off is employed in the model. The yield function of the model defines the stress for which plastic flow takes place and is controlled by a non-associated flow rule. The piles are modelled by use of an elastic, isotropic model.

3.5 Material and Interface Properties

The soil properties in the six models are defined equal to the findings of the six laboratory tests, cf. Tab. 2. (Thomassen and Roesen, 2010)

Table 2: Soil properties determined by the six laboratory tests and employed in the FLAC^{3D} models. The elasticity moduli written in parentheses are found by means of the numerical model.

	φ_{tr} [°]	ψ_{tr} [°]	γ' [kN/m^3]	E_0 [MPa]
Model 1	53.7	19.6	10.3	(4.0)
Model 2	50.3	19.0	10.4	38.24
Model 3	47.7	18.3	10.4	55.61
Model 4	54.4	20.4	10.4	(2.0)
Model 5	50.4	19.1	10.4	38.6
Model 6	48.0	18.6	10.4	57.2

For the tests without overburden pressure the low stresses lead to large uncertainties in the calculation of the initial tangential elasticity modulus, E_0. Thus, in the numerical models without overburden pressure E_0 is calibrated as described in Sec. 3.7. Due to the small variations in effective stresses through the soil layer the soil parameters are assumed to be constant with depth for all the models. A cohesion, c, of 0.1 kPa and Poissons ratio, ν, of 0.23 are applied for the soil in all six models.

Because the piles are modelled as solid cylinders instead of hollow piles, as the ones used in the laboratory, an equivalent bending stiffness and density is required. Based on this equivalence a reduced elasticity modulus, E_{solid}, for the modelled piles are found.

$$E_{solid} = \frac{E_{hollow} \cdot I_{hollow}}{I_{solid}} \tag{1}$$

I is the second moment of inertia, and the subscripts $_{hollow}$ and $_{solid}$ denote the parameters derived for the pipe piles in the laboratory tests and the parameters employed in FLAC^{3D}, respectively. In the same way the density is equated with the cross-sectional area. The elasticity modulus and density of the pipe piles are set to the values for aluminium; $7.2 \cdot 10^4$ MPa and 2700 kg/m^3, respectively.

The interface properties are calibrated by means of the numerical models as described in Sec. 3.7. When using the interface properties listed in Tab. 3 the load-deflection curves are found to be similar to the curves obtained in the laboratory tests.

Table 3: Interface properties calibrated by means of the numerical models. E_0 is the initial tangential elasticity modulus of the soil, cf. Tab. 2.

Friction	φ_{int}	30°
Cohesion	c_{int}	0.1 kPa
Dilation	ψ_{int}	0°
Normal stiffness	k_n	$100 \times E_0$
Shear stiffness	k_s	$100 \times E_0$

3.6 Calculation of the Pile Bending Moment and Soil Resistance

The bending moment of the pile at a given level is calculated by use of Naviers formula, Eq. 2. In order to eliminate the average vertical stress, corresponding to the axial force acting on the pile, the bending moment in each level is calculated by two points $(y,z) = (\pm D/2,\ 0)$.

$$M = \frac{\sigma_{xx,i} \cdot I_{zz}}{y_i} \tag{2}$$

$\sigma_{xx,i}$ is the vertical normal stress at point i, I_{zz} is the second moment of inertia around the z-axis, and y_i is the y-coordinate for the point, cf. Fig. 3. The soil resistance per unit length along the pile, p_y, is computed directly by integrating the stresses in the interface nodes along the interface circumference C.

$$p_y = \int T_y dC \tag{3}$$

T_y is the y-component stress in a node i positioned in the interface.

3.7 Calibration of the Numerical Models

The calibration of the numerical models is based on a comparison between the modelled load-deflection curves and the load-deflection curves obtained from the small-scale tests in the laboratory.

For the models without overburden pressure E_0 is calibrated in relation to the initial stiffness of the load-deflection curves. In Figs. 4 and 5 the calibrated curves for $P_0 = 0$ kPa are shown. In the figures it is seen that the capacity of the calibrated models exceeds the capacity of the laboratory tests. This indicates that the internal angle of friction, φ_{tr}, inserted in the models are overestimated. φ_{tr} is based on the CPT's conducted prior to each laboratory test. At low stress levels φ_{tr} varies significantly with the stresses and it is difficult to determine φ_{tr} with sufficient accuracy.

The agreement between the capacity in the calibrated and the measured load-deflection relationship are found to increase with increasing pile diameter and

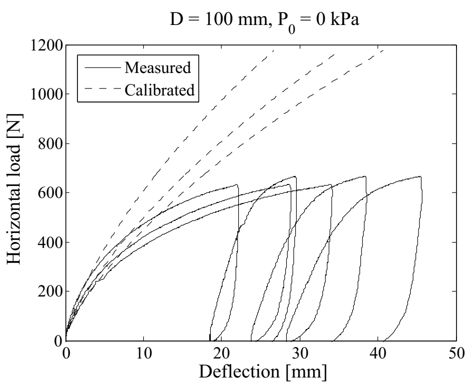

Figure 4: Calibrated and measured relationships at three levels above the soil surface for the test 100 mm with P_0 = 0 kPa.

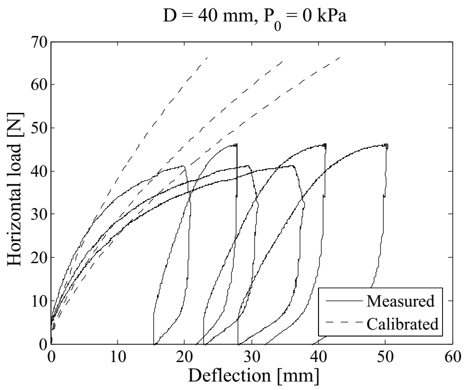

Figure 5: Calibrated and measured relationships at three levels above the soil surface for the 40 mm pile with P_0 = 0 kPa.

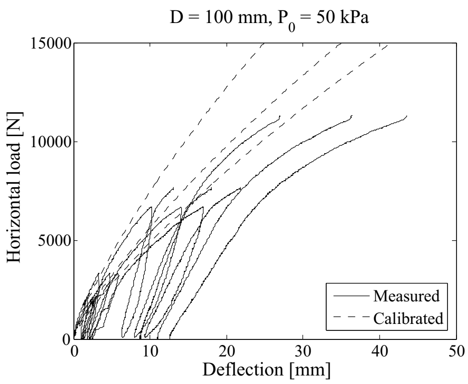

Figure 6: Calibrated and measured relationships at three levels above the soil surface for the 100 mm pile with P_0 = 0 kPa.

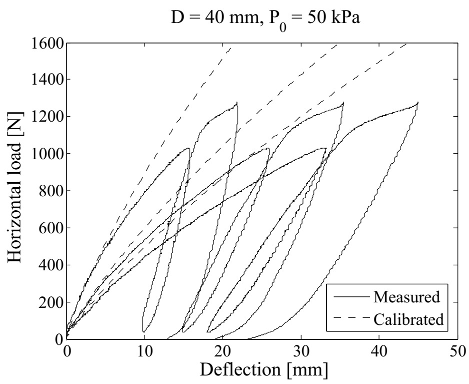

Figure 7: Calibrated and measured relationships at three levels above the soil surface for the 40 mm pile with P_0 = 0 kPa.

increasing overburden pressure, cf. Figs. 4 to 9. Thus, the best agreement is found for the 100 mm pile with an overburden pressure of 100 kPa, cf. Fig. 8.

Considerable uncertainties are related to the test results for the 40 mm pile, cf. Thomassen and Roesen (2010). This can also be concluded from the calibration of the model with the 40 mm pile and $P_0 = 100$ kPa as significant disagreement between the calibrated and the measured values are found, cf. Fig. 9. This disagreement is explained by a disturbance of the soil prior to the test as described in Thomassen and Roesen (2010).

The calibration of the six models clearly indicates that the accuracy in small-scale testing is increased when increasing the pile diameter and applying overburden pressure.

4 Evaluation of Results from the Numerical Models

Prior to the evaluation of the bending moment and deflection of the pile a convergence of the stresses in the numerical models is checked by a comparison between the

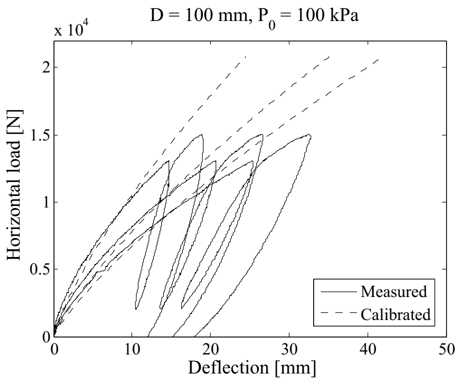

Figure 8: Calibrated and measured relationships at three levels above the soil surface for the 100 mm pile with P_0 = 100 kPa.

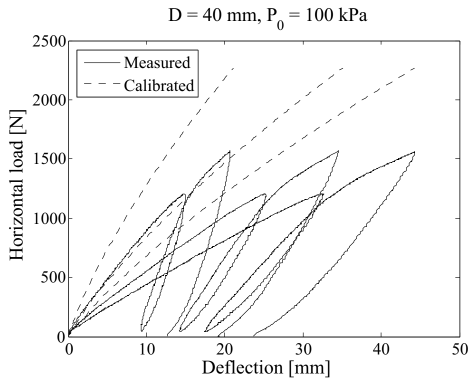

Figure 9: Calibrated and measured relationships at three levels above the soil surface for the 40 mm pile with P_0 = 100 kPa.

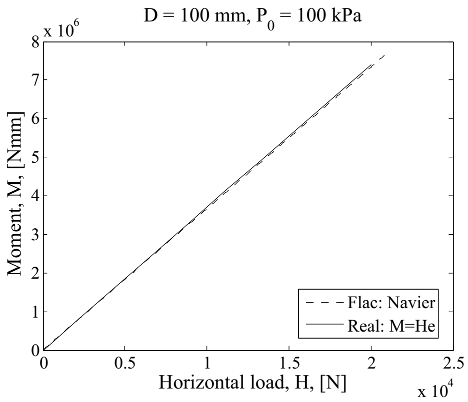

Figure 10: Comparison of the applied moment (applied load H multiplied with the load eccentricity, e, with the computed bending moment at soil surface for the 100 mm pile with P_0 = 100 kPa.

applied moment and the computed bending moment, cf. Fig. 10. In all the models the computed bending moment is in agreement with the applied moment.

4.1 Evaluation of Bending Moment and Lateral Deflection

In Figs. 11 and 12 the bending moment distribution along the piles below the soil surface is shown. For both models the prescribed displacement at $x = -370$ mm is 35 mm. In the figures it is seen that the maximum bending moment occurs at different locations depending on the overburden pressure. When overburden pressure is applied, the point of maximum bending moment is located closer to the soil surface. This indicates that the relative increase in soil resistance with overburden pressure is most significant at the soil surface.

In Figs. 13 and 14 the lateral deflection with depth at three different overburden pressures is shown. The prescribed deflection at $x = -370$ mm is 35 mm. Below the soil surface the deflection is recorded in 21 levels for the 40 mm pile and 26 levels for the 100 mm pile. Above the soil surface the deflection is recorded in two levels: $x = -200$ mm and $x = -370$ mm.

When applying overburden pressure the pile exhibits a more flexible behaviour than without overburden pressure, cf. Figs. 13 and 14. This is in accordance with Poulos and Hull (1989), who proposed a criterion for the pile-soil interaction in which an increase in the soil stiffness compared to the pile stiffness will lead to a more flexible behaviour of the pile. When applying overburden pressure the effective stress level increases, leading to an increase in the soil stiffness.

Although the piles behave more flexible when overburden pressure is applied, the primary deflection is caused by rigid body

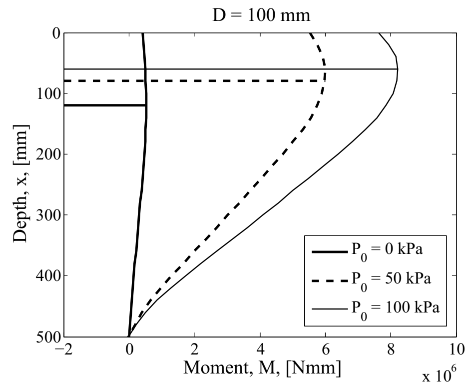

Figure 11: Bending moment distribution at different overburden pressures for the 100 mm piles. The horizontal lines indicate the depth of maximum moment.

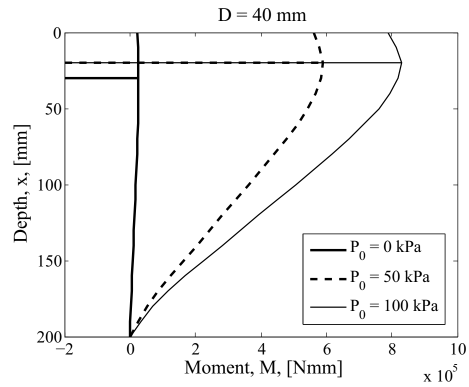

Figure 12: Bending moment distribution at different overburden pressures for the 40 mm piles. The horizontal lines indicate the depth of maximum moment.

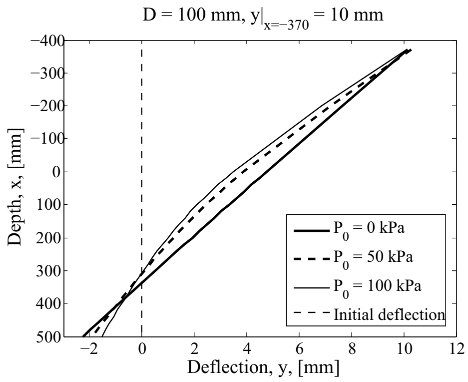

Figure 13: Lateral deflection with depth for different overburden pressures for the 100 mm piles.

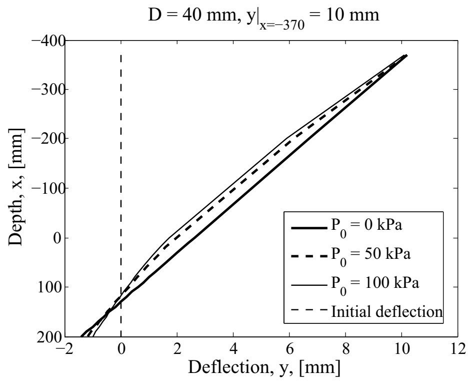

Figure 14: Lateral deflection with depth for different overburden pressures for the 40 mm piles.

rotation, which is evident because only a single point of rotation and a negative deflection at pile toe is present, cf. Figs. 13 and 14.

4.2 Evaluation of Diameter effect on the p–y Curves

The $p - y$ curves from the models with 40 mm and 100 mm piles without overburden pressures are compared at three different depths; 20 mm, 40 mm and 60 mm, cf. Fig. 15.

At the depth of 20 mm the ultimate soil resistance for the 100 mm pile is higher than for the 40 mm pile. At the depth of 40 mm the opposite is the case. For the depth of 60 mm it seems the curve for the 40 mm pile is approaching the ultimate soil resistance for the 100 mm pile. Which of the two curves that reaches the highest ultimate resistance is not possible to predict because of the limited displacement applied. Based on Fig. 15 the diameter is not thought to have an influence on the ultimate soil resistance.

From Fig. 15 it can be seen that the initial stiffness of the curves are dependent on the pile diameter, i.e. the larger pile diameter the higher initial stiffness. This is in contrast to API (1993) and DNV (1992) in which the initial stiffness is considered

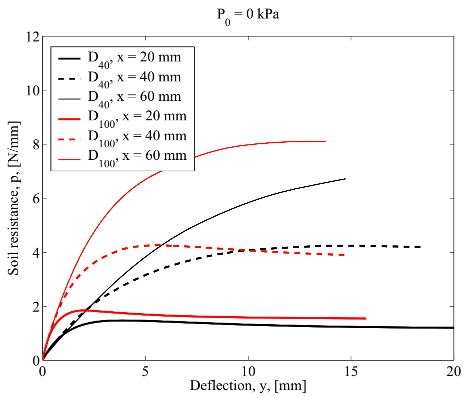

Figure 15: $p-y$ curves at three different depths for models with 40 mm and 100 mm piles and P_0 = 0 kPa.

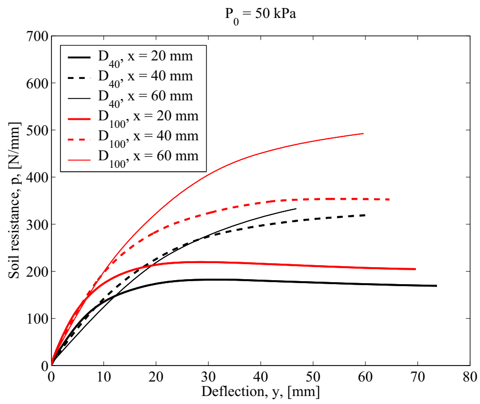

Figure 16: $p-y$ curves at three different depths for models with 40 mm and 50 mm piles and P_0 = 100 kPa

independent on the pile diameter. The dependency of the diameter on the initial stiffness is further evaluated in Sec. 7.

For the models with overburden pressure the three $p-y$ curves at same levels are shown in Figs. 16 and 17. As in the models without overburden pressure the initial stiffness of the $p-y$ curves is found to be dependent on the pile diameter.

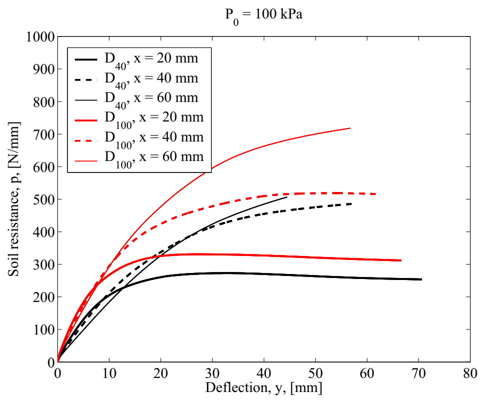

Figure 17: $p-y$ curves at three different depths for models with 40 mm and 100 mm piles and P_0 = 100 kPa.

4.3 Evaluation of the p–y Curves Dependency on Stress Level

In Figs. 18 to 20 the soil resistance along the 100 mm pile is shown for a prescribed deflection of 10 mm and 35 mm at $x = -370$ mm, respectively. The soil resistance is calculated at 24 levels along the pile and are shown for the pressures 0 kPa, 50 kPa, and 100 kPa. In Figs. 21 to 23 the $p-y$ curves for the 100 mm pile at the 24 levels are shown for the different overburden pressures. In the current theory concerning the initial stiffness, E^*_{py}, e.g. DNV (1992); API (1993); Lesny and Wiemann (2006); Sørensen et al. (2010), E^*_{py} is found to increase either linear or non-linear with depth. Therefore, the expected results from the obtained $p-y$ curves would be an increase in the E^*_{py} with depth as well.

Fig. 18 shows that the soil resistance increases with depth from the soil surface to a depth of approximately 150 mm. This increase is in agreement with the expected variation. When evaluating E^*_{py} of the $p-y$ curves in the same depth interval E^*_{py} is constant with depth, cf. Fig. 21. In the depth interval between 150 mm and the rotation point of the pile, at approximately 340 mm, the soil resistance is seen to decrease with depth. Concurrently, E^*_{py} is seen to decrease with depth in the same interval.

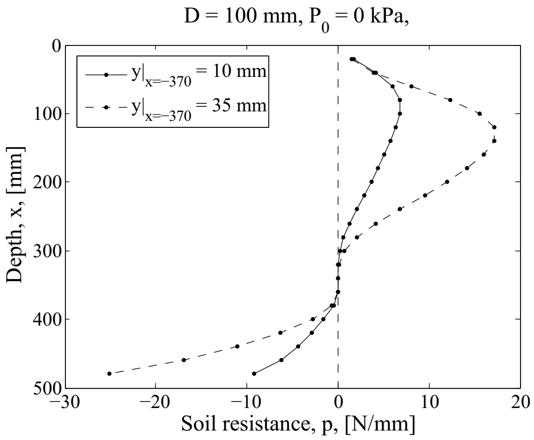

Figure 18: Soil resistance along the 100 mm pile with P_0 = 0 kPa.

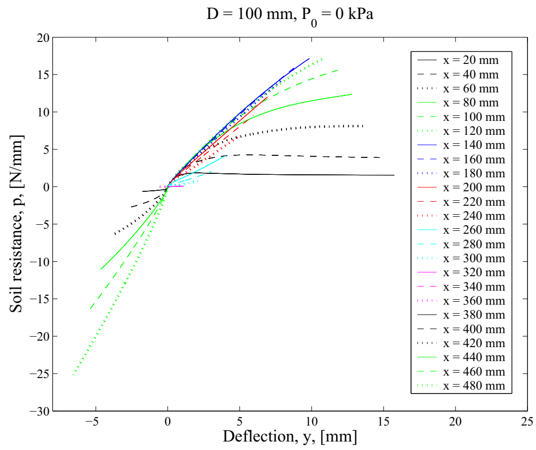

Figure 21: $p - y$ curves along the 100 mm pile with P_0 = 0 kPa.

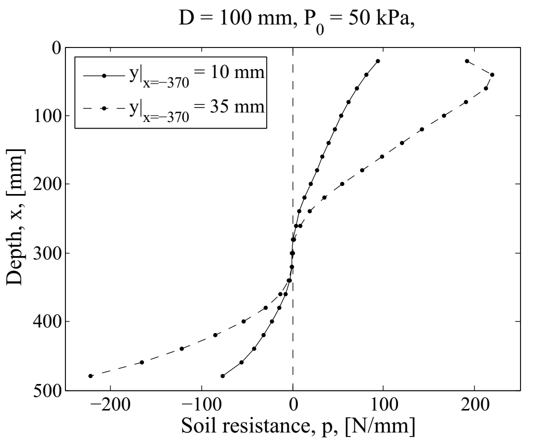

Figure 19: Soil resistance along the 100 mm pile with P_0 = 50 kPa.

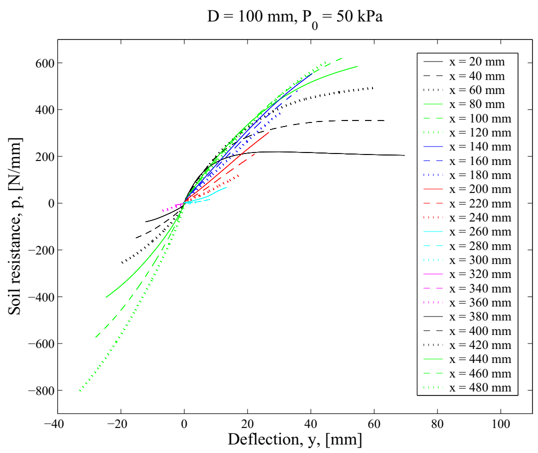

Figure 22: $p - y$ curves along the 100 mm pile with P_0 = 50 kPa.

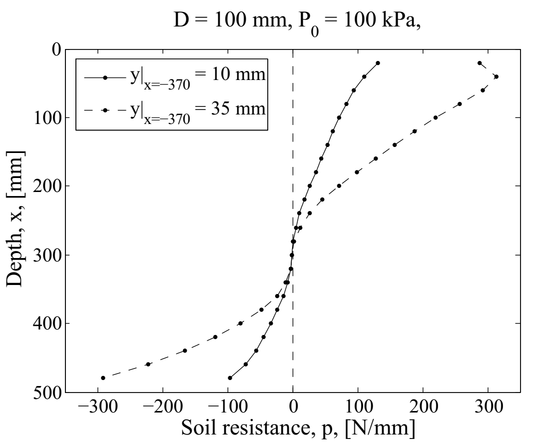

Figure 20: Soil resistance along the 100 mm pile with P_0 = 100 kPa.

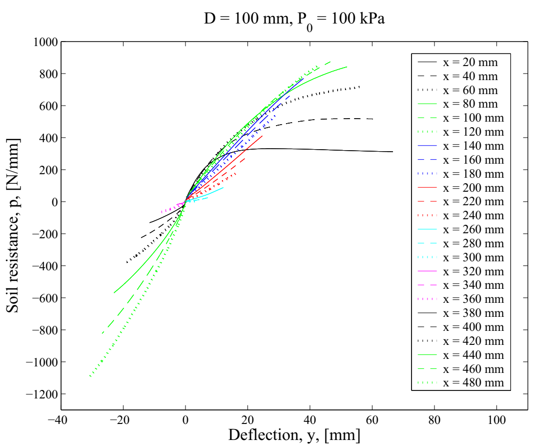

Figure 23: $p - y$ curves along the 100 mm pile with P_0 = 100 kPa.

Below the point of rotation, where the pile exhibit a negative deflection, a negative increase in the soil resistance is present. Below the point of pile rotation E^*_{py} is found to increase with depth.

In the models with overburden pressure applied, cf. Figs. 19 and 20, the soil resistance is mainly seen to decrease with depth from the soil surface to the point of pile rotation at approximately 310 mm. When evaluating the $p-y$ curves shown in Figs. 22 and 23 E^*_{py} is found to decrease with depth to the point of pile rotation. Similar to the finding for the test without overburden pressure the soil resistance below the point of rotation is seen to increase negatively with depth and E^*_{py} increases. The findings imply that E^*_{py} is dependent on the state of stress. Similar finding are found when evaluating the 40 mm pile.

The obtained results should be considered with reservations due to the fact that the soil stiffness is modelled constant with depth. Secondly, a more advanced constitutive model, in which the variation of the stiffness with the deflection is taken into account, could have been used. Hereby, the stiffness of the soil would increase at small deflections, leading to an increase of the initial stiffness of the $p-y$ curves instead of the decrease of E^*_{py} at small deflections as observed in Figs. 18 to 23. Thus, in future research a further evaluation of the initial stiffness of the $p-y$ curves is recommended. The evaluation should consist of laboratory tests on piles instrumented with strain gauges, and numerical modelling with more advanced constitutive models employed.

5 Comparison of Test Results and Theory

To compare the test results to the recommendations given by the design regulations, API (1993) and DNV (1992), a traditional Winkler model is made in MATLAB by using the finite element toolbox CALFEM. Furthermore, the model is used to evaluate different expressions for the ultimate soil resistance.

5.1 Evaluation of Tests with Overburden Pressure

To model the tests with overburden pressure, P_0, the formulation for the ultimate soil resistance must be able to take P_0 into account. Hansen (1961) and Georgiadis (1983) both proposed a formulation in which the overburden pressure is taken into account. Hansen (1961) incorporated the overburden pressure directly in the expression for the ultimate soil resistance at moderate depth. The approach by Georgiadis (1983) was developed to incorporate determination of the ultimate soil resistance for layered soils in a Winkler model. This is done by introducing an equivalent system with fictive depths, x', for each of the soil layers. In this paper the approach is used to employ an equivalent system with a fictive depth of the sand layer to describe the effect of the overburden pressure.

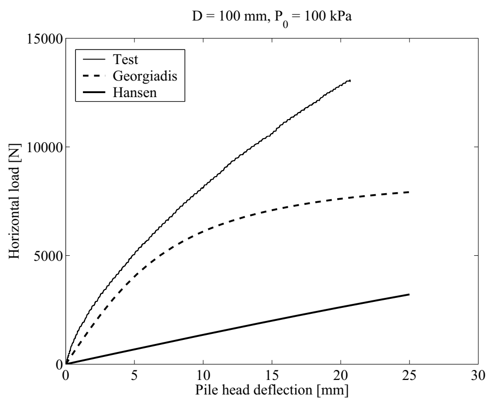

Figure 24: Load-deflection relationships measured at the level of the hydraulic piston ($x = -370$ mm) obtained from the tests and the Winkler model approach with the two expressions for the ultimate soil resistance accounting for the overburden pressure incorporated. D = 100 mm. P_0 = 100 kPa. The initial modulus of subgrade reaction, k, is set to 40000 kN/m^3.

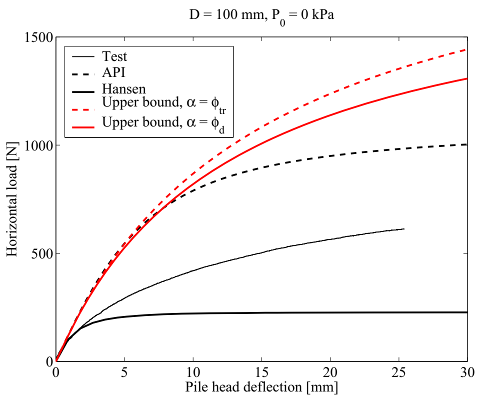

Figure 25: Load-deflection relationships measured at the height of the hydraulic piston ($x = -370$ mm) obtained from the tests and the Winkler model approach with the three different expressions for the ultimate soil resistance incorporated. $D = 100$ mm. $P_0 = 0$ kPa. The initial modulus of subgrade reaction, k, is set to 40000 kN/m^3.

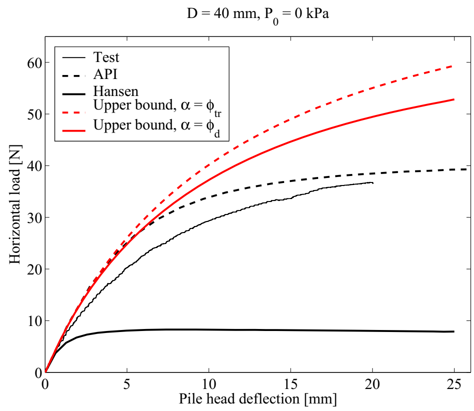

Figure 26: Load-deflection relationships measured at the height of the hydraulic piston ($x = -370$ mm) obtained from the tests and the Winkler model approach with the three different expressions for the ultimate soil resistance incorporated. $D = 40$ mm. $P_0 = 0$ kPa. The initial modulus of subgrade reaction, k, is set to 40000 kN/m^3.

In Fig. 24 the load-deflection relationship obtained by the two different methods are compared to the test results for the 100 mm pile with $P_0 = 100$ kPa. The figure shows that when employing the formulation given by Hansen (1961) the lateral load is significantly underestimated. The approach given by Georgiadis (1983) gives larger lateral load, but still, the load is underestimated. Thus, neither of the formulations are able to take the effect of the overburden pressure into account in a satisfactory way.

5.2 Evaluation of the Ultimate Soil Resistance

As none of the evaluated methods for incorporating the overburden pressure produced satisfactory results the evaluation of the ultimate soil resistance is based on the tests without overburden pressure. The expression for the ultimate soil resistance recommended by API (1993) is compared to two upper bound expressions given in Gwizdala and Jacobsen (1992) and Jacobsen (1989), respectively, and a lower bound solution given by Hansen (1961). The difference of the four expressions is the shape of the wedge formed in front of the pile, which is defined by the angle α. In API (1993), which is based on the formulation derived by Reese et al. (1974), $\alpha = \varphi_{tr}/2$. For the upper bound formulations $\alpha = \varphi_{tr}$ and $\alpha = \varphi_d$, the latter given by Eq. 4. For the lower bound formulation $\alpha = 0$.

$$\tan \varphi_d = \frac{\sin \varphi_d \cdot \cos \psi}{1 - \sin \varphi_{pl} \cdot \sin \psi} \quad (4)$$

φ_d is the reduced angle of friction, which takes the energy loss into account in the kinematic admissible solution. $\varphi_{pl} = 1.1 \cdot \varphi_{tr}$ is the plane angle of friction. The four expressions are incorporated in the Winkler model and the obtained load-deflection curves are shown in Figs. 25 and 26 together with the test results.

For the 100 mm pile with $P_0 = 0$ kPa, cf. Fig. 25, the ultimate soil resistance given by the horizontal asymptote of the curve is overestimated by both upper bound solutions. However the solution with the reduced angle of friction is seen to give the best estimate of the two. The lower bound solution is seen to underestimate the ulti-

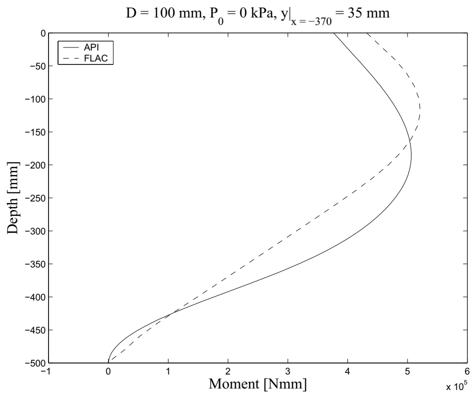

Figure 27: The moment curves obtained by means of the Winkler model approach with the ultimate soil resistance calculated by the design regulation formulation incorporated and the numerical model for D = 100 mm and P_0 = 0 kPa

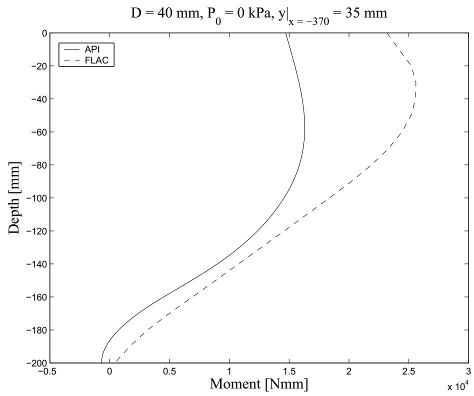

Figure 28: The moment curves obtained by means of the Winkler model approach with the ultimate soil resistance calculated by the design regulation formulation incorporated and the numerical model for D = 40 mm and P_0 = 0 kPa

mate soil resistance. The expression given in API (1993) predicts a lower capacity than the upperbound solutions but still the capacity is overestimated compared to the test results.

For the 40 mm pile the test results and the ultimate soil resistance determined according to API (1993) is found to be in better agreement, cf. Fig. 26. However, the deviation between the results for the 100 mm and the 40 mm pile must be seen in relation to the uncertainties when conducting the tests, where the largest uncertainties are related to the 40 mm pile, cf. Thomassen and Roesen (2010). Nevertheless, from the four expressions evaluated the expression given in API (1993) is found to give the best estimate of the ultimate soil resistance even though the results deviates from the laboratory tests.

6 Comparison of Design Regulations and Numerical Models

To establish whether the recommendations in the design regulations API (1993) and DNV (1992) gives good estimations of the pile-soil interaction for non-slender piles the design method and model results are compared. Again, only the results from the tests without overburden pressure are compared.

6.1 Evaluation of Bending Moment Distribution

The bending moment curves obtained from the numerical models are compared to the bending moment calculated by means of the Winkler model approach using the formulation for the ultimate soil resistances given by API (1993).

In Figs. 27 and 28 the moment curves for the 40 mm and 100 mm piles, respectively, are shown. Both curves are shown for a prescribed deflection of 35 mm at $x = -370$ mm. For both piles it can be seen that the maximum moment obtained by the numerical models is located approximately $1/5L$ below the soil surface. The maximum moment obtained from the Winkler approach is located approximately $2/5L$ below the soil surface. The maximum moments found by the numerical models are higher than the ones obtained by the Winkler model approach.

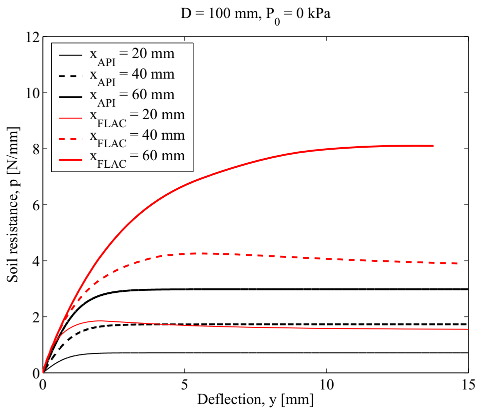

Figure 29: $p-y$ curves for three depths from the numerical model and the design regulation formulation for the 100 mm pile with P_0 = 0 kPa.

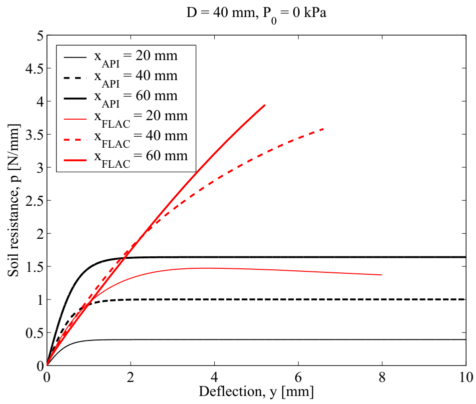

Figure 30: $p-y$ curves for three depths from the numerical model and the design regulation formulation for the 40 mm pile with P_0 = 0 kPa.

The maximum curvature of the moment-curves indicates the maximum soil pressure. At pile toe it can be seen that the moment obtained by means of API (1993) is curved whereas the modelled moment curve has no curvature. This indicates a difference in soil pressure and pile behaviour. Due to the differences between the measured and calculated moment distributions it is recommended that tests are carried out on piles instrumented with strain gauges in order to evaluate the correct behaviour of the pile.

6.2 Evalutation of p–y Curves

The $p-y$ curves recommended in the design regulations API (1993) and DNV (1992) are compared to the $p-y$ curves obtained by the numerical models. For the two tests without overburden pressure the comparison is shown in Figs. 29 and 30 for three different depths.

The figures show that the ultimate soil resistance recommended by API (1993) is significantly lower than the resistance obtained by the numerical models, most significant for the 40 mm pile, cf. Fig. 30. This large difference is believed to occur because the capacity in the numerical models are overestimated compared to the test results. Hence, the difference emerge from uncertainties when determining the soil parameters for low stress levels. In Fig. 30 the initial stiffness of the $p-y$ curves from the numerical models is seen to be in agreement with the calculated initial stiffness from the curve at a depth of 40 mm. In Fig. 29, however, the initial stiffness of the $p-y$ curves from the numerical models is in agreement with the calculated initial stiffness from the curve at 60 mm. Because the initial stiffness found by the numerical models are seen to be constant with depth, in the evaluated depth interval, and because of the difference in Fig. 29 and Fig. 30 it is difficult to draw any clear conclusions in relation to the recommendations other than the agreement between the curves are poor.

7 Evaluation of Initial Stiffness

In API (1993) and DNV (1992) the initial stiffness of the $p-y$ curves, E^*_{py} given by Eq. 5, is assumed to vary linearly with depth.

$$E^*_{py} = \frac{dp}{dy}|_{y=0} = k \cdot x \tag{5}$$

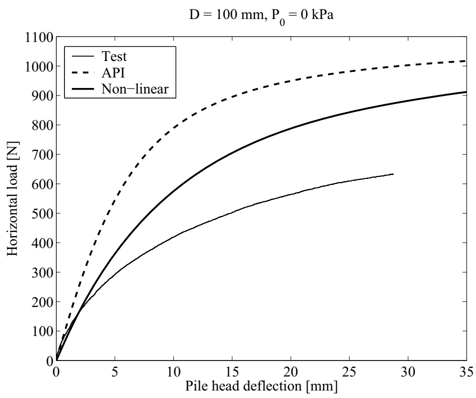

Figure 31: Load-deflection relation ships measured at the height of the hydraulic piston (x = -370 mm) obtained from the tests and the Winkler model approach with the expressions for the ultimate soil resistance with both linear and non-linear formulation of the initial stiffness incorporated. D = 100 mm. P_0 = 0 kPa. The initial modulus of subgrade reaction, k, is set to 40000 kN/m^3.

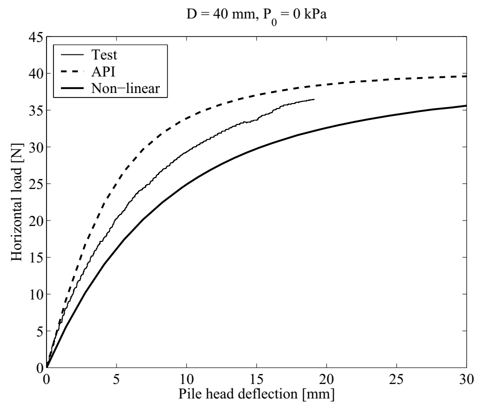

Figure 32: Load-deflection relation ships measured at the height of the hydraulic piston (x = -370 mm) obtained from the tests and the Winkler model approach with the expressions for the ultimate soil resistance with both linear and non-linear formulation of the initial stiffness incorporated. D = 40 mm. P_0 = 0 kPa. The initial modulus of subgrade reaction, k, is set to 40000 kN/m^3.

k is the initial modulus of subgrade reaction and x is the depth below soil surface. k is according to the design regulations dependent only on the relative density of the soil and, thus, independent of the pile properties.

Because of strict demands for the maximum rotation of the wind turbines and the resonance in serviceability mode the initial stiffness of the $p-y$ curves are of great importance. Therefore, it is of interest to find a correct expression for the initial stiffness in order to find the correct pile deflection. Sørensen et al. (2010) proposed a non-linear formulation for the initial stiffness, cf. Eq. 6, based on numerical simulations of full-scale monopiles in sand.

$$E_{py}^{*} = a\left(\frac{x}{x_{ref}}\right)^{b}\left(\frac{D}{D_{ref}}\right)^{c}\varphi_{tr}^{d} \qquad (6)$$

a is a factor determining E_{py}^{*} for (x,D,φ_{tr}) = (1 m, 1 m, 1 rad) and the constants (b,c,d) = (0.6, 0.5, 3.6), $a = 50000$ kN/m^2. x_{ref} and D_{ref} are reference values both of 1 m.

Similar to API (1993) the initial stiffness increases with increasing internal angle of friction, however, with a slightly different variation. Contrary to API (1993) the initial stiffness increases with increasing pile diameter and varies non-linearly with depth when using Eq. 6.

7.1 Comparison of Load-Deflection Relationships

Eq. 6 is inserted in the formulation for the soil resistance given in API (1993) and employed in the Winkler model. Thereby, the load-deflection relationships shown in Figs. 31 and 32 for the two piles without overburden pressure are obtained.

For the 40 mm pile, cf. Fig. 32, it is difficult to determine, which of the formulations gives the best fit to the test results as these results are positioned in between the two. Moreover, because of the large uncertainties for this test, the results may not be representative for the correct pile-soil behaviour.

The uncertainties for the test results with the 100 mm pile are smaller, and the results are considered more accurate. Fig. 31 shows that the formulation by API (1993) overestimates the lateral capacity. When using the non-linear formulation for the initial stiffness the lateral capacity is closer to the measured results, however, still overestimated. For the initial part of the curves, the non-linear expression is seen to be in better agreement with the results obtained in the laboratory tests and therefore the non-linear expression is believed to give the best estimate of the variation of the initial stiffness.

7.2 Comparison of p–y Curves

In order to evaluate the diameter effect the non-linear formulation, Eq. 6, for the initial stiffness is evaluated against the initial stiffness found from the $p-y$ curves from the six numerical models. The factor c is evaluated by the ratios:

$$\frac{E^*_{py}|_{D=100}}{E^*_{py}|_{D=40}} = \left(\frac{D_{100}}{D_{40}}\right)^c \tag{7}$$

The initial stiffness of the numerically obtained $p-y$ curves, cf. Figs. 15, 16, and 17, is found by linear regression of the data until a deflection of approximately 0.2 mm. The slope of the linear regression is assumed representative for the initial stiffness, and the obtained values for the six models are shown in Tab. 4.

Table 4: The initial stiffness in N/mm^2 read of the $p-y$ curves obtained from the FLAC^{3D}-models for the two piles at different overburden pressures, cf. Figs. 15, 16, and 17.

	0 kPa	50 kPa	100 kPa
$E^*_{py}\|_{D=100}$	2.9	42.3	79.2
$E^*_{py}\|_{D=40}$	1.3	30.0	48.9

Table 5: Ratio of the initial stiffness of the $p-y$ curves obtained in the numerical models for the different overburden pressures.

	0 kPa	50 kPa	100 kPa
$\frac{E^*_{py}\|_{D=100}}{E^*_{py}\|_{D=40}}$	2.3	1.4	1.6

With $c = 0.5$, as proposed by Sørensen et al. (2010), the right side of Eq. 7 gives approximately 1.6. If this value of c is correct the ratio on the left side of the equation should give values of approximately 1.6 as well. In Tab. 5 the ratios of the initial stiffness from the numerical models are given. It can be seen that the ratio for the models without overburden pressure deviates the most. The ratios for the models with overburden pressure indicates that $c = 0.5$ is an appropriate value for the diameter effect on the initial stiffness. Again, this indicate that larger uncertainties are related to the tests without overburden pressure and, hence, low stress levels in the soil.

8 Conclusion

In this paper the diameter effect on the pile-soil interaction is evaluated by means of results from small-scale laboratory tests, numerical models of the same test setup, and existing theory. In total six tests were carried out on piles with outer diameters of 40 mm and 100 mm, respectively, and a slenderness ratio L/D of 5. In four of the tests overburden pressures of 50 kPa and 100 kPa were applied. The tests were modelled in the numerical finite difference program FLAC^{3D}, and the models were calibrated against the obtained load-deflection relationships from the laboratory tests. From the numerical models $p-y$ curves for the six tests were obtained and used in a comparison with the recommended curves in the current design regulations. From the evaluations, the following conclusions can be drawn:

From the numerical models the recorded deflection along the pile when subjected to lateral loading showed an increase in flexible behaviour when overburden pressure was applied. However, the primary deflection of the piles were caused by rigid body rotation.

To take the overburden pressure into account in the Winkler model approach formulations proposed by Hansen (1961) and Georgiadis (1983) was evaluated. However, none of the formulations produced results in agreement with the test results.

By means of the Winkler model approach the formulations for the ultimate soil resistance given by API (1993), Hansen (1961), Gwizdala and Jacobsen (1992), and Jacobsen (1989) were compared to the load-deflection relationships obtained from the laboratory tests without overburden pressure. The comparison showed that the formulation given by the current design regulation API (1993) provided the best agreement to the test results even though the ultimate resistance was overestimated even though the ultimate soil resistance was overestimated.

Based on a comparison of the $p-y$ curves for the two pile diameters it was found that the initial stiffness, E^*_{py}, is dependent on the pile diameter, i.e. the initial stiffness increases with increasing pile diameter. Further, the $p-y$ curves obtained in the numerical models indicated that E^*_{py} is dependent on the stress state as E^*_{py} increases with increasing soil pressure along the pile and decreases with decreasing soil pressure.

The dependency of the diameter was evaluated by means of E^*_{py} obtained in the numerical models and by the non-linear formulation suggested in Sørensen et al. (2010). The models with overburden pressure indicated that a value of $c = 0.5$ for the diameter dependency is an appropriate value. By employing the formulation in a Winkler model approach the non-linear formulation was compared to the tests results and it was found that this formulation was in better agreement with the results than the formulations given in API (1993) and DNV (1992) where E^*_{py} is assumed independent of pile diameter.

From the calibration of the numerical models, the evaluation of $p-y$ curves, and the evaluation of E^*_{py} it was found that considerable uncertainties are related to small-scale testing and the different evaluations clearly indicates that the accuracy in small-scale testing is increased when increasing pile diameter and applying overburden pressure.

9 Acknowlegdements

The project is associated with the EFP programme ”Physical and numerical modelling of monopile for offshore wind turbines”, journal no. 033001/33033-0039. The funding is sincerely acknowledged.

Bibliography

API (1993), *Recommended Practice for Planning, Designing and Constructing Fixed Offshore Platforms – Working Stress Design*, American Petroleum Institute.

Brødbæk, K., Møller, M., Sørensen, S. and Augustesen, A. (2009), ‘Evaluation of p-y relationship in cohesionless soil’, *DCE Technical Report No. 57* . Aalborg University.

DNV (1992), *Foundations*, Det Norske Veritas. Classification Notes No. 30.4.

Georgiadis, M. (1983), ‘Development of p-y curves for layered soils’, *Proceedings of the Conference on Geotechnical Engineering* pp. 536–545.

Gwizdala, K. and Jacobsen, M., eds (1992), *Bearing capacity and settlements of piles*, Aalborg University. ISBN 87-88787-10-9.

Hansen, J. B. (1961), 'The Ultimate Resistance of Rigid Piles Against Transversal Forces', *Bulletin No. 12* . Geoteknisk Institut.

Ibsen, L. B., Hanson, M., Hjort, T. and Thaarup, M. (2009), 'MC-Parameter Calibration for Baskarp Sand No. 15', *DCE Technical Report No.62* . Department of Civil Engineering, Aalborg University.

Jacobsen, M. (1989), *Lærebog i videregående Geotektik 1, Brud i Jord.*

Lesny, K. and Wiemann, J. (2006), 'Finite-Element-Modelling of Large Diameter Monopiles for Offshore Wind Energy Converters', *Geo Congress* .

Poulos, H. and Hull, T. (1989), 'The Role of Analytical Geomechanics in Foundation Engineering', *Foundation Engineering: Current principles and practice, 2* pp. 1578–1606.

Reese, L. C., Cox, W. R. and Koop, F. D. (1974), 'Analysis of Laterally Loaded Piles in Sand', *Offshore Technology Conference* . Paper Number OTC 2080.

Sørensen, S., Ibsen, L. and Augustesen, A. (2010), 'Effects of diameter on initial stiffness of p-y curves for large-diameter piles in sand'. Aalborg University.

Thomassen, K. and Roesen, H. R. (2010), 'Small-Scale Testing of Laterally Loaded, Non-Slender Monopiles in Sand', Short Candidate Project.

Recent publications in the DCE Technical Report Series

Brødbæk, K. T., Møller, M., Sørensen, S. P. H. and Augustesen, A. H. (2009) *Review of p-y relationships in cohesionless soil*, DCE Technical Report No. 57, Aalborg University. Department of Civil Engineering.

Sørensen, S. P. H., Møller, M., Brødbæk, K. T., Augustesen, A. H. and Ibsen, L. B. (2009) *Evaluation of Load-Displacement Relationships for Non-Slender Monopiles in Sand*, DCE Technical Report No. 79, Aalborg University. Department of Civil Engineering.

Sørensen, S. P. H., Møller, M., Brødbæk, K. T., Augustesen, A. H. and Ibsen, L. B. (2009) *Numerical Evaluation of Load-Displacement Relationships for Non-Slender Monopiles in Sand*, DCE Technical Report No. 80, Aalborg University. Department of Civil Engineering.

Thomassen, K., Roesen, H. R., Ibsen, L. B. And Sørensen, S. P. H. (2010) *Small-Scale Testing of Laterally Loaded Non-Slender Monopiles in Sand*, DCE Technical Report No. 90, Aalborg University. Department of Civil Engineering.

ISSN 1901-726X
DCE Technical Report No. 91

CHAPTER 4

CONCLUDING REMARKS

The aim of this thesis was to evaluate the diameter effect on the initial stiffness of the $p-y$ curves when using piles with a slenderness ratio $L/D < 10$. This slenderness ratio corresponds to the monopiles used as foundation for offshore wind turbines today. The evaluation was conducted by three approaches on piles installed in cohesionless soil.

- **Small-scale testing:** Six small-scale tests were conducted in a pressure tank in the Geotechnical Engineering Laboratory at Aalborg University, Denmark. The test programme was chosen to supplement the tests conducted in Sørensen et al. (2009), and the obtained load-deflection relationships were compared with the previous findings.
- **Numerical modelling:** The six small-scale tests were modelled in the finite difference program FLAC^{3D}. The material properties found in the laboratory tests were employed, and the tests were calibrated by evaluating the load-deflection relationships. $p-y$ curves representative for the small-scale tests were obtained by the numerical models.
- **Existing theory:** By means of a Winkler model approach the load-deflection relationships, when using the $p-y$ curve formulation in the current design regulations, were compared to the small-scale tests. Two formulations for incorporating the overburden pressure were evaluated and four different expressions for evaluating the ultimate soil resistance were employed.

Based on the evaluations some conclusions were drawn. In the following sections summaries of the three approaches are given and the conclusions are outlined.

4.1 Small-Scale Testing

The six small-scale tests were conducted on two test piles with a wall thickness of 5 mm and outer diameters of 40 mm and 100 mm, respectively. The slenderness ratio for both piles were $L/D = 5$, resulting in embedded length of 200 mm and

500 mm. The lateral load was applied 370 mm above the soil surface, and three displacement transducers were mounted at levels of 200 mm, 370 mm, and 480 mm above the soil surface. Thereby, load-deflection relationships for the piles were achieved.

Prior to each test the soil was vibrated to ensure fully saturated soil and a homogeneous compaction. The soil parameters were then derived based on results from cone penetration tests. The six tests were conducted in a pressure tank in order to control the confining pressure, and pressures of 0 kPa, 50 kPa, and 100 kPa, respectively, were applied. An elastic membrane was placed on the soil surface sealing the upper part of the tank from the soil. When increasing the pressure in the upper part of the tank, the membrane was pressed against the soil leading to an increase of the stresses in the soil. The lower part of the soil was connected to an ascension pipe leaving the applied load to be stresses between the grains only, i.e. an increase in effective stresses. Hereby, problems with the non-linear yield surface at low stress levels were overcome.

The tests on the 40 mm pile was found to be subject to a large amount of uncertainties. Only a little disturbance of the soil lead to large inaccuracies of the test results.

4.2 Numerical Modelling

The numerical modelling of the six laboratory tests was conducted by means of the explicit finite difference program FLAC^{3D}. In the models the correct soil properties found from the laboratory test were used. For the tests without overburden pressure the low stresses lead to large uncertainties in the calculation of the initial tangential elasticity modulus of the soil, E_0. Thus, in the models without overburden pressure E_0 was calibrated by means of the model. Further, the soil parameters were assumed to be constant with depth for all the models due to small variations in the effective stresses because of the limited thickness of the sand layer. In order to model the interaction between the pile and the soil an interface was employed.

The numerical models were calibrated by varying the interface properties. To be consistent the same interface properties were used in all the models. The calibration of the models was based on a comparison between the modelled load-deflection curves and the load-deflection curves obtained from the small-scale tests in the laboratory. For the initial part of the curves the calibrated load-deflection relationships was found to be in good agreement with the measured relationships. The similarity between the measured and the calibrated capacity was found to increase with increasing pile diameter and overburden pressure. Thus, the best agreement was found for the test with the 100 mm pile and an overburden pressure of 100 kPa. This indicates that the accuracy in small-scale testing is increased when increasing the pile diameter and applying overburden pressure. The FLAC^{3D}-models were assumed to be representative for the laboratory tests, and the bending moment distribution, pile deflection, and soil resistance were evaluated based on the findings in the FLAC^{3D}-models.

4.3 Evaluation of Existing Theory

For the tests with overburden pressure an attempt was made to compare the load-deflection relationships obtained by the tests to theoretical formulations taking the overburden pressure into account. By use of the Winkler model approach two formulations were evaluated. Firstly, a method incorporating layered soil, suggested by Georgiadis (1983), was modified to take the overburden pressure into account and secondly, the formulation given by Hansen (1961), in which the overburden pressure is taken into account, were evaluated. Both formulations resulted in significantly underestimated loads compared to the laboratory tests. Thus, it is concluded that none of the existing formulations are able to take the effect of overburden pressure into account in a satisfactory way.

When evaluating the ultimate soil resistance only the tests without overburden pressure were considered. The load-deflection relationships achieved from the laboratory tests were compared to the load-deflection relationships obtained by the Winkler model approach with different formulations for the ultimate soil resistance incorporated. The evaluated formulations were the current design regulations API (1993) and DNV (1992), two upper bound formulations given by Gwizdala and Jacobsen (1992) and Jacobsen (1989), respectively, and the lower bound formulation derived by Hansen (1961). The formulation in the design regulations were found to give the best fit to the measured load-deflection relationships, however, the load was overestimated by the formulation.

The design regulations, API (1993) and DNV (1992), assume that the initial stiffness varies linearly with depth. Sørensen et al. (2010) suggested an expression were the initial stiffness, E^{*}_{py}, varies non-linearly with both depth and pile diameter. This expression was employed in the Winkler model and the obtained load-deflection relationships were compared to the test results for the tests without overburden pressure and the relationships achieved by API (1993). For the 100 mm pile it was found, that the initial part of the measured load-deflection relationship was in best agreement with the non-linear variation of E^{*}_{py}. For the 40 mm pile it could not be concluded, which of the two formulations were in best agreement with the test results.

The $p-y$ curves obtained by the numerical models without overburden pressure were compared to the $p-y$ curves recommended in the design regulations at three different depths. Because of the rigid behaviour of the test piles deviations between the compared $p-y$ curves were expected. However, the total disagreement found between the curves were unexpected. The large deviations are believed to be caused by the large internal angle of friction, φ_{tr}, inserted in the numerical models.

4.4 Major Findings

Through the evaluation of the results obtained by the laboratory tests, the numerical modelling and existing theory conclusions regarding the following subjects were drawn.

4.4.1 Lateral Pile Deflection

The current design regulations are based on very few experiments on slender piles with a slenderness ratio, L/D, of 34.4. Recently installed monopiles have a slenderness ratio less than 10, which causes an almost rigid behaviour of the piles when subjected to lateral loads. The tested and modelled piles had a slenderness ratio of 5, and the behaviour of the piles, when subjected to lateral load, was evaluated based on the recorded deflection along the piles in the numerical models. The evaluation showed an increase in flexible behaviour when overburden pressure was applied. However, the primary deflection of the piles was caused by rigid body rotation, which was evident as only a single point of rotation was present and because of a negative deflection at pile toe.

4.4.2 Diameter Effect on Pile-Soil Interaction

Firstly, the diameter effect was evaluated based on the load-deflection relationships obtained from the laboratory tests. It was found that the load increased for increasing pile diameter and embedded length. The normalised load-deflection relationships implied that the horizontal load is proportional to the embedded length squared times the pile diameter, $H \propto L^2D$. This is in agreement with the findings in Sørensen et al. (2009).

Secondly, the diameter effect was evaluated based on the $p-y$ curves obtained in the numerical models without overburden pressure and the recommended curves in API (1993) and DNV (1992). In a comparison between these curves it was found that the recommended curves was in poor agreement with the numerically obtained curves as the ultimate soil resistance was significantly lower. Moreover, the initial stiffness of the curves, E^*_{py}, were not consistent. One reason for the poor agreement must be found in the calibration of the numerical models where the soil capacity was overestimated. Another factor of importance is that E^*_{py} obtained in the numerical models was found to increase with increasing soil resistance and decrease with decreasing soil resistance. This is in contrast to the assumptions in both the design regulations, where E^*_{py} is assumed to vary linearly with depth, and to Lesny and Wiemann (2006) and Sørensen et al. (2010) who propose a non-linearly variation with depth. The findings indicate that the E^*_{py} is dependent on the stress state.

Based on a comparison of the $p-y$ curves from the numerical models it was found that E^*_{py} is dependent on the pile diameter, i.e. E^*_{py} increases with increasing diameter. The dependency was evaluated by means of the formulation given in Sørensen, Ibsen, and Augustensen (Sørensen et al.) and the E^*_{py} found from the numerical models. The models with overburden pressure indicated that a value of $c = 0.5$ for the diameter dependency is an appropriate value. This is in concordance with the suggestion of Sørensen et al. (2010).

4.4.3 Effects of Low Stress Level

Conducting small-scale tests at low stress levels produce large uncertainties of the test results. These uncertainties arise because the internal angle of friction, φ_{tr}, is highly dependent on the stress at low stress levels. At low stress levels the yield surface describes a curved line in the σ'-τ coordinate system. Small inaccuracies of the CPT readings obtained prior to the tests without overburden pressure leads to inaccurate calculations of the identity index, I_D, again leading to an incorrect calculated value of φ_{tr}. The problems of conducting small-scale tests at low stress levels can be seen both in the laboratory test results and in the calibration of the numerical models.

When normalising the load-deflection relationships for the laboratory tests the curves were not similar due to the stress variations along the piles. Increasing the effective stresses produced normalised load-deflection relationships where the curves were similar. This indicates that by increasing the stress level more accurate results are produced.

The calibration of the numerical models, by means of the results for the tests without overburden pressure, showed similarity of the initial part of the load-deflection curves due to the adjustment of the modulus of elasticity of the soil. The remaining part of the curves showed no resemblance likely because of an overestimated value of φ_{tr}. The dependency on the value of φ_{tr} was not examined.

From the small-scale test results and the numerical results it can be concluded that small-scale testing should be conducted at higher stress levels to achieve accurate results.

4.5 Directions for Future Research

The evaluation of $p-y$ curves in this thesis considers only monopile foundations of offshore wind turbines in homogeneous, dense cohesionless sand. Similar analyses should be conducted for different soil types and sand with various modulus of elasticity and internal angle of friction. Moreover, the effect of layered soil should be analysed. To validate the conclusion of the diameter affect on the pile-soil interaction tests of more diameters and load cases should be conducted. The present evaluation treats only static loading. Offshore wind turbines are subjected to cyclic loads due to the wind and the waves. An examination of the effects of cyclic loading should be performed in order to choose the stiffness of the entire wind turbine system. Moreover, cyclic loading leads to scour holes and the effect on the pile-soil interaction should be investigated.

4.5.1 Small-Scale Testing

In spite of the costs and the time consumption full-scale test should be conducted to extent the current $p-y$ curve method to apply to large-scale non-slender monopiles. Until such tests have been conducted small-scale testing at varying stress levels are important in the prediction of the pile-soil interaction for laterally loaded non-slender monopiles. In these small-scale tests the following aspects are omitted. The effect of the vertical load on the pile and the effect of the tests being conducted on closed-ended piles, which is in contrast to the open-ended piles installed as foundation for the offshore wind turbines. Because of the rigid behaviour of the piles the shear forces along the pile-toe might contribute significantly to the net soil resistance.

In further research small-scale tests should be conducted at even higher stress levels in order to resemble typical offshore wind turbine foundations. The piles should be instrumented with more strain gauges than used in Sørensen et al. (2009) to obtain more measurements of the moment along the pile and, thereby, more accurate $p-y$ curves. To avoid large uncertainties of the tests results, due to disturbance of the soil, piles with diameters larger than 40 mm should be used.

4.5.2 Numerical Modelling

In this thesis the numerical models are used only to resemble the six small-scale tests. These models should be used to make full-scale models in which the diameter effect and the effects of e.g. different slenderness ratios could be investigated in detail. The piles are modelled as massive piles, and models of open-ended piles should be made to analyse plugging, skin friction on the inside of the pile, and shear stresses along the pile-toe. The employed material model is the Mohr-Coulomb model. A more advanced material model should be employed in order to evaluate the variation of the initial stiffness of the $p-y$ curves along the pile.

BIBLIOGRAPHY

API (1993). *Recommended Practice for Planning, Designing and Constructing Fixed Offshore Platforms – Working Stress Design*. American Petroleum Institute.

Danmarks Vindmølleforening (2010, March). Vindmøller på havet. http://www.dvind.dk/fakta/pdf/p4.pdf.

DNV (1992, February). *Foundations*. Det Norske Veritas. Classification Notes No. 30.4.

DNV (2007, October). *Design of Offshore Wind Turbine Structures*. Det Norske Veritas. Offshore Standard DNV–OS-J101.

Dong Energy (2010, March). Horns Rev. http://www.hornsrev.dk/default.

Engels, W., T. Obdam, and F. Savenije (2010). Current developments in wind - 2009, Going to great lengths to improve wind energy.

Fan, C.-C. and J. H. Long (2005). Assessment of existing methods for predicting soil response of laterally loaded piles in sand. *Computers and Geotechnics 32*, 274–289.

Georgiadis, M. (1983). Development of p-y curves for layered soils. *Proceedings of the Conference on Geotechnical Engineering*, 536–545.

Gwizdala, K. and M. Jacobsen (Eds.) (1992). *Bearing capacity and settlements of piles*. Aalborg University. ISBN 87-88787-10-9.

Hansen, J. B. (1961). The Ultimate Resistance of Rigid Piles Against Transversal Forces. *Bulletin No. 12*. Geoteknisk Institut.

Haus Der Technic (2010, March). http://www.hdt-essen.de/domains/downloads/illus_thementexte/offshore_windenergieanlagen/04.gif.

Jacobsen, M. (1989, March). *Lærebog i videregående Geotektik 1, Brud i Jord*.

Lesny, K. and J. Wiemann (2006, February 26 to March 1). Finite-Element-Modelling of Large Diameter Monopiles for Offshore Wind Energy Converters. *Geo Congress*.

Miljø- og Energiministeriet (1996). *Energi 21 Regeringens energihandlingsplan 1996*. ISBN 87-7844-057-2.

Offshore Center Danmark (2010, May). Offshore vindmøller, Historisk udvikling. http://www.offshorecenter.dk/historisk-udvikling-141.asp.

Reese, L. C., W. R. Cox, and F. D. Koop (1974, May 6–8). Analysis of Laterally Loaded Piles in Sand. *Offshore Technology Conference*. Paper Number OTC 2080.

Sørensen, S., K. Brødbæk, M. Møller, A. Augustesen, and L. Ibsen (2009). Evaluation of the Load-Displacement Relationships for Large-Diameter Piles in Sand. *Civil-Comp Press*. Paper 244.

Sørensen, S., L. Ibsen, and A. Augustensen. Effects of Diameter on Initial Stiffness of p-y Curves of Large-Diameter Piles in Sand.

Sørensen, S., L. Ibsen, and A. Augustesen (2010). Effects of diameter on initial stiffness of p-y curves for large-diameter piles in sand. Aalborg University.

Sørensen, S. P., K. T. Brødbæk, and M. Møller (2009). *Evaluation of Load-Displacement Relationships for Large-Diameter Piles*. Faculties of Engineering, Science and Medicine, Aalborg University. Long Candidate Project.

Stiesdal, H. (2009, December). Hywind: The world's first floating MW-scale wind turbine. http://www.ewea.org/fileadmin/ewea_documents/documents/publications/WD/2009_december/Science_corner_-_December_2009.pdf.

Vattenfall (2010, March). Kriegers Flak Offshore Wind Farm - Design Basis Foundations. http://www.vattenfall.se/www/vf_se/vf_se/Gemeinsame.../P02131587.pdf.

World Wind Energy Association (2010, March). World Wind Energy Report 2009. http://www.wwindea.org.

APPENDIX

CONTENTS

APPENDIX A

TEST SETUP

Six small-scale tests are conducted in order to investigate the effect of the pile diameter on the soil resistance in sand for non-slender piles. The test are conducted in a pressure tank in the Geotechnical Engineering Laboratory at Aalborg University. In this appendix the test setup is described.

A.1 Test Setup in Pressure Tank

The tests are carried out on two piles with outer diameters of 40 mm and 100 mm, respectively, both with a wall thickness of 5 mm and closed at the pile toe. The slenderness ratio of the piles is $L/D = 5$ where L the embedded length D and is the diameter.

The piles are subjected to lateral loading by a hydraulic piston positioned 370 mm above the soil surface. The load-deflection relationship is found from measurements from three displacement transducers and a force transducer positioned above the soil surface. The setup is shown in Fig. A.1.

The strength parameters of the cohesionless soil is found by the Mohr-Coulomb failure criterion that describes a straight line in the τ - σ' - coordinate system. The internal angle of friction, φ_{tr}, is determined as the inclination of tangent of this line, cf. Fig. A.2. At higher stress levels, where the assumption of a linear failure criterion is correct, φ_{tr} is independent of the stress level in the soil. At low stress levels the correct failure criterion describes a curved line. When determining φ_{tr} as the inclination of the tangent of this part it is highly dependent on the stress level, and a very high value of φ_{tr} is obtained.

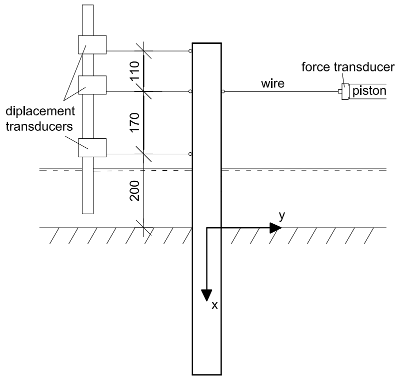

Figure A.1: Position of the four transducers on the pile. All measurements are in mm.

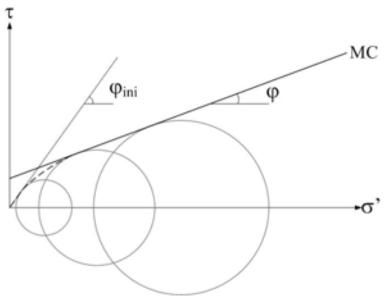

Figure A.2: The Mohr-Coulomb failure criterion and the curved failure line at low stresses in a τ - σ' - coordinate system.

By conducting the tests in a pressure tank it is possible to increase the effective stresses in the soil. The air pressure in the tank can be increased to 2 bar corresponding to the effective stresses at a depth of 20 m in the soil. Thereby the problem described above is minimized and more realistic values of the internal angle of friction can be found by means of correction formulas as described in App. B.

A.1.1 Pressure Tank

The pressure tank is manufactured by Bergla Maskinfabrik in Brønderslev, Denmark, and has a height and diameter of approximately 2.5 m and 2.1 m, respectively. The tank is installed in a load-frame placed on a reinforced foundation with no connection to the surrounding floor. On top of the tank a platform is mounted to ease the preparation of the tests, cf. Fig. A.3.

A trapdoor on the side of the tank is used to enter the tank while preparing the soil and installing the pile. A top hatch is used to mount a hydraulic piston, which is used to install the pile and conducting the cone penetration tests and fixing the pile in upright position during vibration, cf. App. B.2. Measuring devices are led out of openings in the tank side, cf. Fig. A.5, while a hydraulic piston used to induce the lateral load to the pile is led into the tank, cf. Fig. A.6.

A 580 mm thick layer of Baskarp Sand No. 15 is placed in the pressure tank above a layer of highly permeable gravel. During the tests the sand is fully saturated. A cross-sectional view of the test setup can be seen in Fig. A.4.

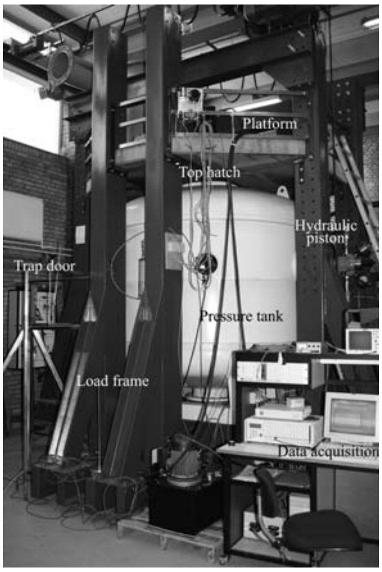

Figure A.3: The pressure tank in the Geotechnical Engineering Laboratory at Aalborg University.

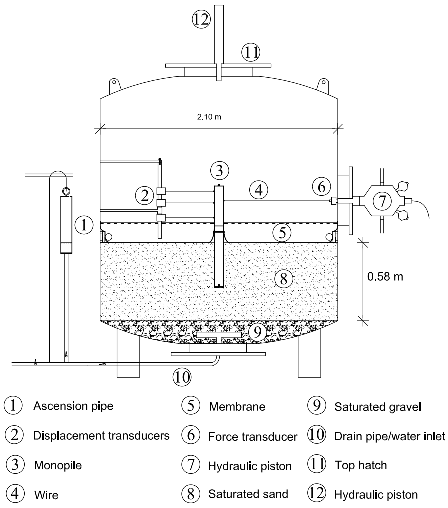

Figure A.4: Cross-sectional view of the test setup.

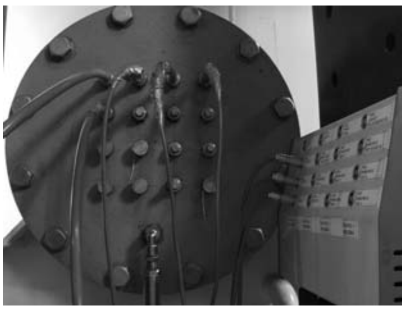

Figure A.5: measuring devices (displacement transducers, force transducer, and manometer) is led out of the tank.

Figure A.6: The hydraulic piston led into the tank.

A.1.2 Increase of the Effective Stresses

The effective stresses are increased by placing a rubber membrane on the soil surface and increasing the air pressure in the tank. This way the effective stresses are increased without increasing the pore pressure in the soil. The dimension of the membrane corresponds to the inner diameter of the pressure tank. The pile is led through a sealing in the middle of the membrane and sealed with two hose clips, cf. Fig. A.7.

Figure A.7: The pile led through the sealing in the membrane and sealed with two hose clips.

In order to minimize the risk of gabs between the membrane and the tank a vertical rubber band is mounted around the outer perimeter of the membrane. Two mouldings are attached to the rubber band to create a more elastic joint between the membrane and the tank, cf. Fig. A.8. Additionally, to reduce the risk of water flowing through this joint a skirt is glued to the side of the tank and placed above the rubber band, cf. Fig. A.10. The skirt is a modification to the test setup used in Sørensen et al. (2009), as the membrane was found to be less tight than wanted. The skirt and the rubber band is pressed against the tank side by means of a fire hose filled with water and air, cf. Fig. A.11. The pressure in the fire hose is increased to approximately 7 bar to ensure a tight sealing between the membrane and the tank. A cross-sectional view of the joint between the membrane and the pressure tank can be seen in Fig. A.9.

Figure A.8: The rubber band on the membrane and the attached mouldings.

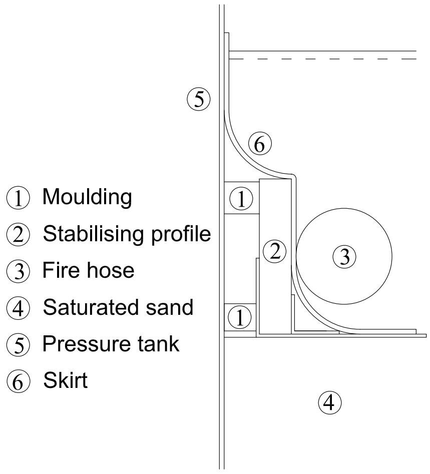

Figure A.9: Cross-section of the joint between the membrane and the pressure tank.

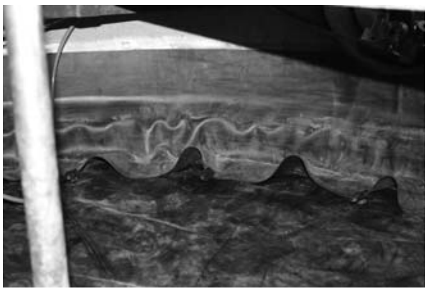

Figure A.10: The skirt glued to the tank side and placed above the rubber band.

Figure A.11: The fire hose pressing the rubber band and the skirt against the tank side.

A.1.3 Hydrostatic Pore Pressure

During the tests, a hydrostatic water pressure corresponding to a water table at the soil surface should be sustained. Two factors are preventing a hydrostatic pore pressure unless precautions are taken.

Since the membrane is not 100 % tight, air can flow through leaks in the membrane and thereby increase the pore pressure. The dynamic viscosity of water is approximately 55 times greater than for air. Therefore, water is filled in above the membrane to cover it during the tests, cf. Fig. A.12. This minimizes flow through leaks in the membrane eventhough it does not prevent it completely. The pore pressure in the soil will increase as a consequence of volumetric strains in the soil when the overburden pressure is applied.

To sustain the hydrostatic pore pressure an ascension pipe is connected to the tank, cf. Fig. A.13. When the water column in the ascension pipe increases, water is led out through a pipe in the bottom of the tank. Because of the volumetric strains a large amount of water is led out of the tank at the time the overburden pressure is applied. Afterwards, the water flow out of the tank corresponds to the water flow through leaks in the membrane. The flow through the membrane is determined to 5 - 10 l/h during the tests which results in an excessive pore pressure. However, it is a very limited amount of excessive pore pressure and, therefore, neglected in evaluation of the tests.

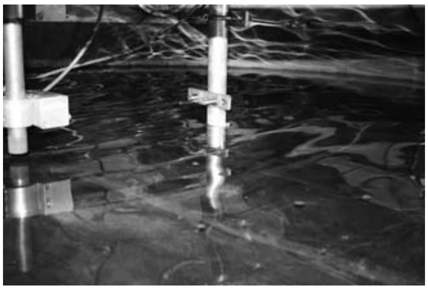

Figure A.12: Water covering the membrane during tests.

Figure A.13: The ascension pipe connected to the tank.

A.2 Soil Characteristics

The soil in the pressure tank is fully saturated Baskarp Sand No. 15. The sand is a graded sand from Sweden. The larger grains are round while the small grains have sharp edges. The sand consists primarily of quarts but contains feldspar and biotite as well. The material properties for Baskarp Sand No. 15 are well-defined from previous tests in the laboratory at Aalborg University. A representative distribution of the grains found by sieve analysis can be seen in Fig. A.14. The properties are given in Tab. A.1.

Table A.1: Material properties for Baskarp Sand No. 15. (Andersen et al., 1998)

Specific grain density d_s [-]	2.64
Maximum void ratio e_{max} [-]	0.858
Minimum void ratio e_{min} [-]	0.549
d_{50} = 50%-quantile [mm]	0.14
$U = d_{60}/d_{10}$ [-]	1.78

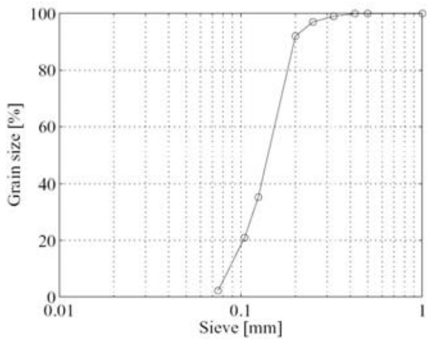

Figure A.14: Distribution of Baskarp Sand No. 15 found by sieve analysis. (Ibsen and Bødker, 1994)

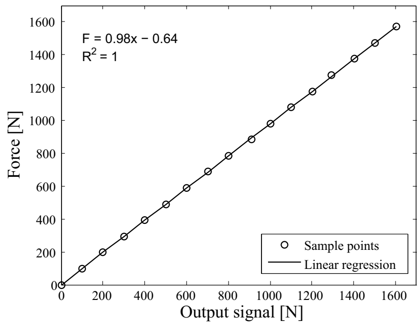

Figure A.15: Calibration of force transducer HBM U2B 20 kN.

A.3 Force Transducer

The force transducer used for the 40 mm pile is a HBM U2B 10 kN, and it connects the wire and the hydraulic system in series, cf. Fig. A.1. For the 100 mm pile the force transducer was changed to a HBM U2B 20 kN transducer because of the higher loads necessary to obtain the given deflection. Before using the new transducer it was calibrated cf. Fig. A.15.

A.4 Test Programme

The tests programme is designed to investigate the effect of the pile diameter on the soil resistance. The conducted tests are a supplement to the tests in Sørensen et al. (2009), where piles with diameters of 60 mm and 80 mm where investigated. In the present test programme aluminium pipe piles with outer diameters of 40 mm and 100 mm are investigated. The slenderness ratio is 5 for all the tests, and the wall thickness is 5 mm. The tests on each of the piles are conducted with different overburden pressures, P_0. The test programme can be seen in Tab. A.2.

Table A.2: Tests conducted in the laboratory.

	D [mm]	L/D [-]	P_0 [kPa]	e [mm]	Reference
Test 1	100	5	0	370	App. G
Test 2	100	5	50	370	App. H
Test 3	100	5	100	370	App. I
Test 4	40	5	0	370	App. J
Test 5	40	5	50	370	App. K
Test 6	40	5	100	370	App. L

When conducting the tests, the soil is brought to failure, unloaded and reloaded. Thereby, it is possible to get an estimate of the ultimate soil resistance and the elastic behaviour of the soil.

APPENDIX B

SOIL PREPARATION AND DERIVATION OF SOIL PARAMETERS

Prior to the testing of the piles in the pressure tank the soil is prepared by mechanical vibration. The vibration is conducted to ensure that the soil is fully saturated, i.e. no air is captured in the sand and to ensure a homogeneous compaction of the soil. The compaction of the soil and the soil parameters are determined by means of cone penetration tests (CPT). In this appendix the soil preparation and interpretation of the CPT readings are described.

B.1 Preparation Prior to the Test

Preparation of the soil is conducted in four different stages depending on the stage of the laboratory work:

- Initial preparation of the soil.
- Re-compaction of the soil near the pile after installation.
- Re-compaction of the soil between tests without removing the pile.
- Re-compaction of the soil between tests after removing the pile.

The following six-point procedure for vibration of the sand is used in each of the four preparation stages, though at times with small modifications as described in the following sections.

- The sand is loosened for at least five minutes by applying an upward gradient of 0.9.
- The holes indicated by the non-solid circles are vibrated, cf. Fig. B.1.

- The holes indicated by the solid circles are vibrated, cf. Fig. B.1.
- The sand is loosened for at least five minutes by applying an upward gradient of 0.9.
- The holes indicated by the non-solid circles are vibrated, cf. Fig. B.1.
- The holes indicated by the solid circles are vibrated, cf. Fig. B.1.

The sand is loosened by an upwards gradient of 0.9 as suggested by Kristensen and Pedersen (2007). A larger gradient may cause water channels in the sand, while a smaller gradient may not loosen the sand satisfactory. The gradient should be applied for at least five minutes. As the thickness of the sand layer is 580 mm the pressure difference in pressure head should be 520 mm, to obtain a gradient of 0.9.

To prevent air entering the soil during vibration the water table should be at least 50 mm above the soil surface. To ensure a homogeneous vibration of the soil a plate with holes large enough for the vibration device to enter is placed above the sand surface, cf. Figs. B.1, B.2, and B.3.

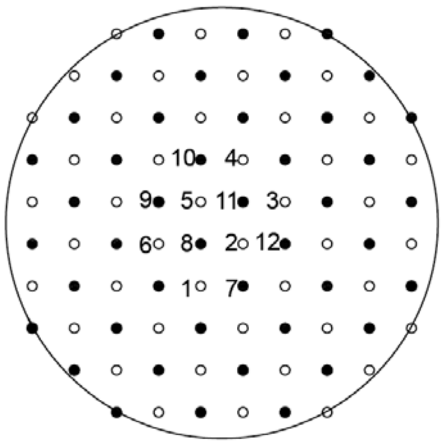

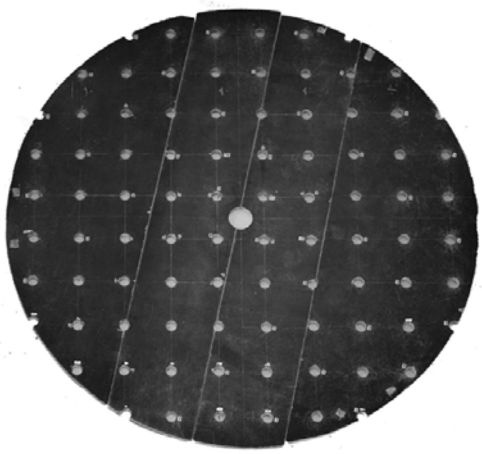

Figure B.1: The plate used for vibration of the soil. To the left: A principle sketch of the vibration plate. The non-solid circles are the holes vibrated first and afterwards the holes indicated by the solid circles are vibrated. The holes with numbers are used when re-compacting the soil near the pile after installation and between tests. To the right: A photo of the plate.

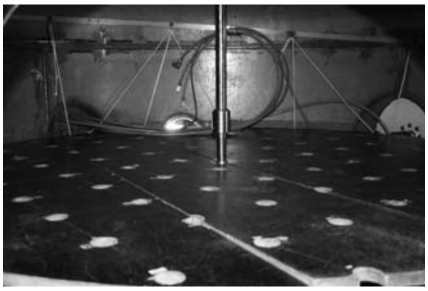

Figure B.2: The plate placed in the tank.

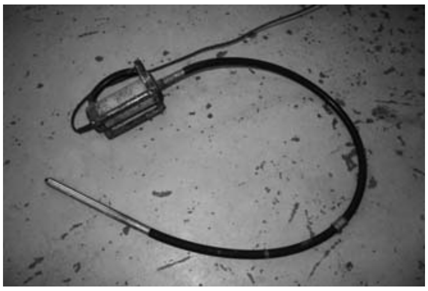

Figure B.3: The vibrator used to vibrate the soil.

B.1.1 Initial Preparation of the Soil

As described in App. A the setup used to ensure a tight membrane during the tests under pressure is slightly modified compared to the tests described in Sørensen et al. (2009). The modification consists of a rubber skirt glued to the side of the tank. To install the rubber skirt the water in the tank had to be let out and 200 mm of the sand layer had to be removed. After the modifications only 100 mm sand were re-installed in the pressure tank, giving the sand layer a final thickness of 580 mm thick.

The drainage, removal, and addition of sand in the tank made it necessary to vibrate the soil several times according to the six-point procedure before conducting the first test. After having vibrated the sand a few times, CPT's were carried out at four different positiones in the sand. The results from these CPT's where compared to results from the CPT's conducted in Sørensen et al. (2009). The six-point procedure and following CPT's where conducted until they showed a homogeneous compaction of the soil in the pressure tank and a cone resistance fairly equal to the results in Sørensen et al. (2009).

B.1.2 Installation of the Pile

The piles installed in the present tests are closed ended piles. To minimize the pressure on the pile during installation an upward gradient of 0.9 is applied. The piles are installed in one continuous motion by the hydraulic piston located at the top of the pressure tank, cf. Fig. A.4.

B.1.3 Re-compaction of the Soil near the Pile after Installation

After installation of a pile the 12 holes closest to the pile are vibrated before the vibration following the six-point procedure takes place. During the vibration the pile is fixed by the hydraulic piston mounted at the top hatch. The reason for vibrating close to the pile is to minimize the effects of the failure of the soil emerged from the installation. Due to this vibration, the coefficient of the horizontal earth pressure and the compaction of the soil near the pile become as similar as possible to those of the surrounding soil.

After the six-point procedure, six CPT's are carried out, cf. Fig. B.4. Four of the CPT's are conducted at a distance of 500 mm from the centre of the pile. The two remaining CPT's are conducted as close to the pile as possible. For the piles with diameters of 100 mm and 40 mm this distance is 200 mm and 160 mm, respectively. The two CPT's close to the pile are conducted at the neutral sides of the pile in relation to the direction of the applied load.

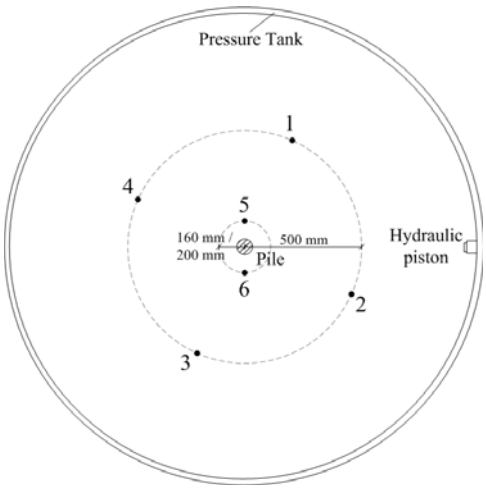

Figure B.4: The positions of the CPT's conducted prior to each test.

B.1.4 Re-compaction of the Soil between Tests

When a test of a pile is finished it is necessary to re-compact the soil. If the pile is to be tested again, it is brought back to its upright position and fixed by the hydraulic piston. Hereafter the soil is vibrated in the twelve holes near the pile and then the six-point procedure is followed. CPT's are conducted to verify the compaction and homogeneity of the soil.

If the pile is to be replaced with another pile, the procedure is the same as the initial procedure described in Sec. B.1.1.

B.2 Cone Penetration Tests

The CPT-device used in the laboratory can be seen in Fig. B.5. The dimensions of the device are given in Fig. B.6. The tip resistance is measured by strain gauges installed in a full bridge attached on a steel pipe behind the cone head. The total resistance, e.g. the sum of the tip resistance and the sleeve friction, is measured by means of three weight cells installed on top of the device. In cohesionless soils the sleeve friction is negligible and, therefore, the weight cells are not employed in the tests.

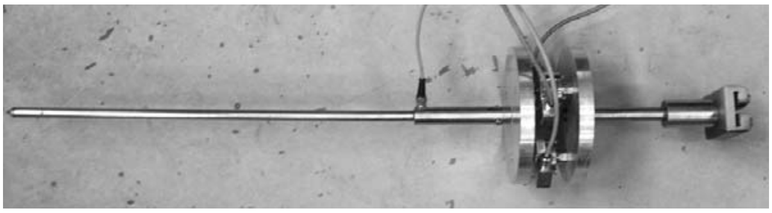

Figure B.5: The CPT device used in the laboratory.

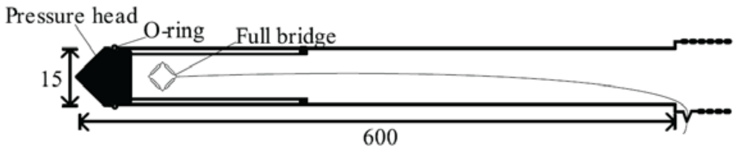

Figure B.6: Sectional view of the CPT-cone. Measures are in mm. After Sørensen et al. (2009)

The CPT-device is pressed into the soil by the hydraulic piston shown in Fig. A.4 with the penetration velocity of approximately 5 mm/s. The CPT-setup is shown in Fig. B.7.

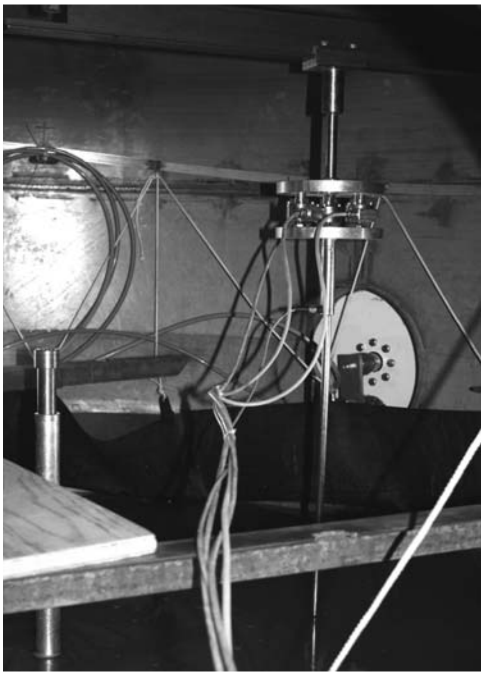

Figure B.7: Setup of the CPT-device.

The strain gauges in the pressure head is calibrated by applying known loads to the CPT-device. To protect the CPT-device from failure caused by instability of the setup the maximum load applied is 60 kg. The linear output from the gauges is shown in Fig. B.8. From linear regression a calibration factor of 1669 N/mV/V is found.

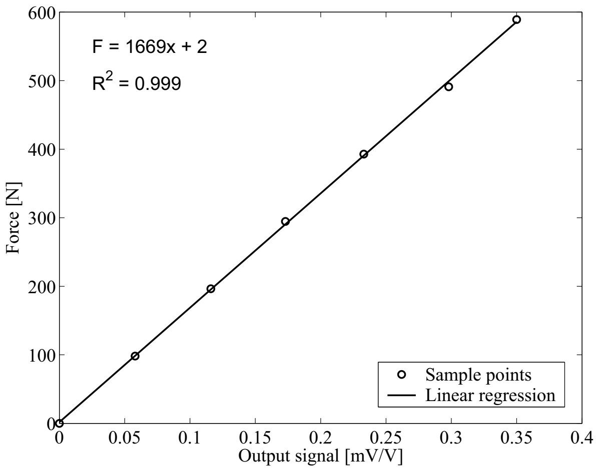

Figure B.8: Calibration output for the CPT-device.

B.3 Interpretation of CPT's

From the conducted CPT's the cone resistance, q_c, plotted against the depth, x, is used to verify a homogeneous compaction of the soil in the pressure tank. The spreading of the cone resistances obtained in the different positions should be small. Furthermore, the values of the cone resistance are similar to the values found by Sørensen et al. (2009).

From the CPT-results the following soil parameters should be determined:

- The internal angle of friction, φ_{tr} [$^{\circ}$].
- The angle of dilation, ψ_{tr} [$^{\circ}$].
- The density index, I_D [-].
- The effective unit weight of the sand, γ' [F/L^3].
- The initial stiffness of the sand, E_0 [F/L^2].

In Ibsen et al. (2009) expressions for the internal angle of friction and the dilation angle are based on results from triaxial tests on Baskarp Sand No. 15. The angles are considered dependent on the density index and the confining pressure. The triaxial tests were performed with two different density indices and nine different confining pressures. Plotting the internal angles of friction against the density index, cf. Fig. B.9, the expression given in Eq. B.1 was determined.

$$\varphi_{tr} = 0.152 \cdot I_D + 27.39 \cdot \sigma_3'^{-0.2807} + 23.21 \tag{B.1}$$

Where:
σ_3' is the confining pressure [kPa]

A similar expression was determined for the dilation angle, cf. Eq. B.2.

$$\psi_{tr} = 0.195 \cdot I_D + 14.86 \cdot \sigma_3'^{-0.09764} - 9.946 \tag{B.2}$$

The density index and the effective unit weight of the sand is found by an iterative procedure involving Eq. B.3 - Eq. B.6.

$$\gamma' = \frac{d_s - 1}{1 + e_{in\text{-}situ}} \gamma_w \tag{B.3}$$

$$\sigma_1' = \gamma' \cdot x \tag{B.4}$$

$$I_D = c_2 \left(\frac{\sigma_1'}{(q_c)^{c_1}} \right)^{c_3} \tag{B.5}$$

$$I_D = \frac{e_{max} - e_{in\text{-}situ}}{e_{max} - e_{min}} \cdot 100 \tag{B.6}$$

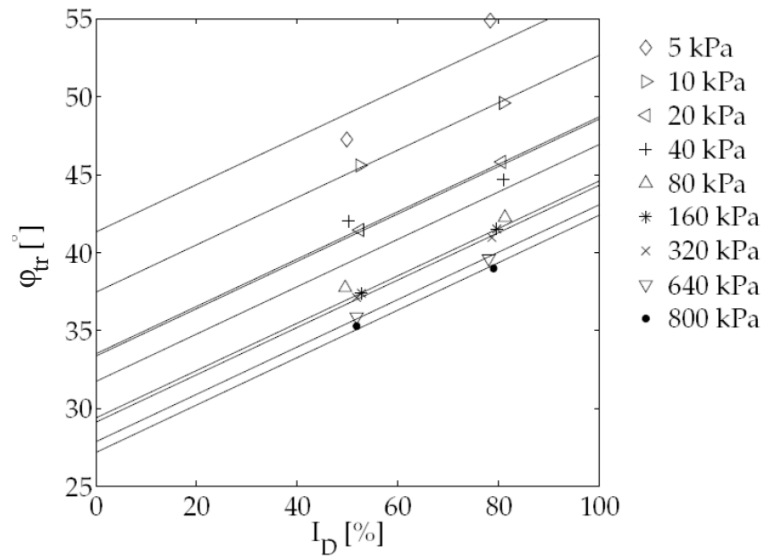

Figure B.9: Internal angle of friction versus density index (Ibsen et al., 2009)

Where:

γ'	is the effective unit weight of the soil [kN/m^3]
d_s	is the relative density, d_s = 2.64
$e_{in\text{-}situ}$	is the in-situ void ratio [-]
γ_w	is the unit weight of water, γ_w = 10 kN/m^3
σ_1'	is the effective vertical stress [MPa]
q_c	is the cone resistance [MPa]
x	is the depth [m]
c_1, c_2, c_3	are constants, (c_1, c_2, c_3) = (0.75, 5.14, -0.42)
e_{max}	is the maximum void ratio, e_{max} = 0.858
e_{min}	is the minimum void ratio, e_{min} = 0.549

As well as the unit weight of the soil and the density index are unknown so is the initial void ratio. To find the first two, a value of $e_{in\text{-}situ}$ is set into the formulas and the iteration is continued until the difference between the two successive values of $e_{in\text{-}situ}$ is less than 10^{-4}.

The effective horizontal stress, σ_3', is dependent on σ_1' and the horizontal earth pressure coefficient at rest, K_0. K_0 can be expressed in terms of φ_{tr}, cf. Eq. B.7 (Ovesen et al., 2007). Thereby, φ_{tr} is the only unknown in Eq. B.1 and can be found by iteration.

$$\begin{aligned}\sigma_3' &= \sigma_1' \cdot K_0 \\ &= \left(\gamma' \cdot x + P_0\right) \cdot K_0 \\ &= \left(\gamma' \cdot x + P_0\right) \cdot (1 - \sin\varphi_{tr}) \end{aligned} \tag{B.7}$$

Where:
K_0 is the earth pressure coefficient at rest [-]
P_0 is the overburden pressure [kPa]

From Eq. B.1 it is seen that $\varphi_{tr} \rightarrow \infty$ for $\sigma_3' \rightarrow 0$. Furthermore, it is seen from Fig. B.9 that Eq. B.1 does not fit the triaxial tests for σ_3' = 5 kPa very well. When conducting the CPT's the cone only reaches a depth of 0.45 m. Thereby, the stress levels in the σ_3' direction for the tests without overburden pressure lies in the interval 0 - 2.5 kPa. In order to use Eq. B.1 σ_3' is set to 5 kPa for these tests. This may result in a slightly lower value of the friction angle than the correct one, but the difference is considered tolerable.

The initial stiffness of the soil, E_0, is determined from the secant modulus of elasticity given in Eq. B.8 suggested by Ibsen et al. (2009). Eq. B.9 is given by Brinkgreve and Swolfs (2007).

$$E_{50} = \left(0.6322 \cdot I_D^{2.507} + 10920\right) \left(\frac{c \cdot \cos\varphi_{tr} + \sigma_3' \cdot \sin\varphi_{tr}}{c \cdot \cos\varphi_{tr} + \sigma_3'^{\,ref} \cdot \sin\varphi_{tr}} \right)^{0.58} \tag{B.8}$$

$$E_0 = \frac{2 \cdot E_{50}}{2 - R_f} \tag{B.9}$$

Where:
E_{50} is the secant modulus of elasticity [kPa]
$\sigma_3'^{\,ref}$ is the reference pressure here $\sigma_3'^{\,ref}$ = 100 kPa
E_0 is the tangential modulus of elasticity [kPa]
R_f is the ratio between q_f and q_a, the standard value is $R_f = 0.9$ cf. Brinkgreve and Swolfs (2007)
q_f is the ultimate deviatoric stress [kPa]
q_a is the asymptotic value of the shear strength [kPa]

Tab. B.1 gives the soil parameters derived from the CPT's conducted prior to the six tests. Because of high uncertainties when employing Eq. B.8 and B.9 to the results from tests at low stress levels, E_0 is not calculated for the tests without overburden pressure.

Table B.1: Material properties determined from the CPT's for the six tests.

	D [mm]	P_0 [kPa]	φ_{tr} [°]	ψ_{tr} [°]	I_D [-]	γ' [kN/m^3]	E_0 [MPa]
Test 1	100	0	53.7	19.6	0.86	10.3	-
Test 2	100	50	50.3	19.0	0.89	10.4	38.24
Test 3	100	100	47.7	18.3	0.90	10.4	55.61
Test 4	40	0	54.4	20.4	0.91	10.4	-
Test 5	40	50	50.4	19.1	0.89	10.4	38.6
Test 6	40	100	48.0	18.6	0.91	10.4	57.2

APPENDIX C

EVALUATION OF THE *p–y* CURVE METHOD FOR PILES IN SAND

Design of a monopile under lateral loading is difficult because the analyses are sensitive to the stress-strain characteristics of the surrounding soil. $p-y$ curves are used to describe the relation between the soil resistance acting against the pile, p, and the pile deflection, y, as a function of the depth during lateral loading. In this appendix the development of the $p-y$ curves for sand is described together with the advantages and limitations of the curves.

C.1 Pile-Soil Interaction

The idea of $p-y$ curves is presented in Fig. C.1. The figure shows a possible stress distribution before and during lateral loading of a circular pile at depth x_t. During the lateral loading, the deflection, y_t, will generate an unbalanced soil pressure against the pile leading to a net force, p_t, acting on the pile at the depth x_t. p_t is the soil resistance given as force per unit length. The deflection of the pile will also generate a vertical resistance, but it is assumed that such resistance is small compared to the lateral resistance and can be ignored in the analyses. (Reese et al., 1974)

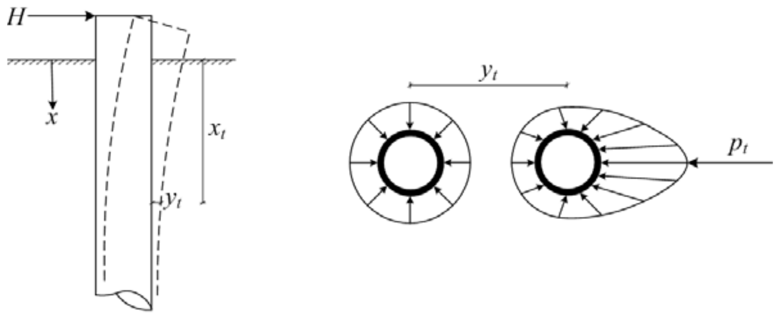

Figure C.1: Distribution of stresses before and during lateral loading of a circular pile. p_t denotes the net force acting on the pile at the depth x_t. After Reese et al. (1974)

In Fig. C.2 a typical $p-y$ curve is shown together with the definitions of the ultimate soil resistance, p_u, the subgrade reaction modulus, E_{py}, and the initial stiffness E^*_{py} .

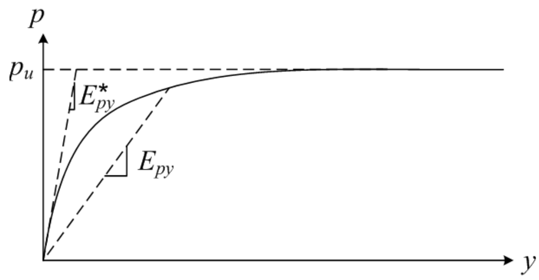

Figure C.2: Typical *p–y* curve with definitions of the ultimate soil resistance, p_u, the subgrade reaction modulus, E_{py}, and the initial stiffness, E^*_{py}. After Reese et al. (1974)

The ultimate soil resistance, p_u, is defined as the upper horizontal limit of the resistance. The horizontal line indicates the plastic behaviour of the soil where the shear strength is constant for increasing strain.

The subgrade reaction modulus, E_{py}, is defined as the secant stiffness of the $p-y$ curve. It describes the stiffness of the interaction between the pile and the soil and not the stiffness of the soil itself. Because E_{py} describes the interaction it is dependent on the pile type, geometry, installation procedure, pile rotation, soil conditions and type of loading. Further, E_{py} is a function of the lateral deflection, y, and the depth, x. As seen in Fig. C.2 the modulus decreases with increasing deflection. (Augustesen and Ibsen, 2008)

The initial stiffness of the $p-y$ curve is described by an initial tangent stiffness, E^*_{py}, cf. Fig. C.2. The initial stiffness represents the linear elastic behaviour of the soil and governs only small deflections. (Reese et al., 1974)

Assuming that the soil behaviour at a particular depth is independent of the soil behaviour at all other depths a set of $p-y$ curves, as shown in Fig. C.3, can be obtained. The curves can be used in design of a laterally loaded pile. The assumption is not strictly true, but experiments have shown that the soil reaction at a point is essentially dependent on the pile deflection at that point and not on the pile deflections above and below. (Reese and Van Impe, 2001)

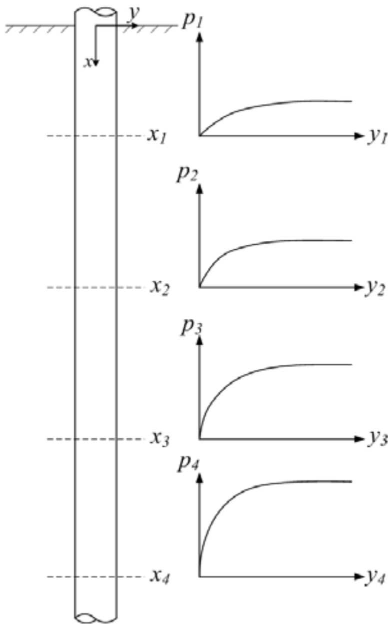

Figure C.3: Set of $p-y$ curves for different depths along the pile. After Reese et al. (1974)

Definitions of the used parameters and dimensions are presented in Tab. C.1.

Table C.1: Definition of parameters and dimensions.

Description	Symbol	Definition	Dimension
Soil resistance per unit length	p		F/L
Ultimate soil resistance (capacity) per unit length	p_u		F/L
Soil pressure	P	$P = p/D$	F/L^2
Pile deflection	y		L
Depth below seabed	x		L
Pile diameter	D		L
Embedded pile length	L		L
Second moment of inertia of the pile	I_p		L^4
Modulus of elasticity of the pile	E_p		F/L^2
Modulus of subgrade reaction	E_{py}	$E_{py} = p/y$	F/L^2
Initial stiffness	E^*_{py}	$E^*_{py} = k \cdot x$	F/L^2
Coefficient of initial subgrade reaction	k	P/y	F/L^3
Vertical load on pile	Q		F
Horizontal load on pile	H		F
Moment on pile	M		FL^2
Overburden pressure	P_0		F/L^2

C.2 Original *p–y* Curves

The original $p-y$ curve formulation for sand was formulated by Reese et al. (1974) and developed based on experiments on two identical laterally loaded full-sized piles at Mustang Island, Texas. The two piles were steel pipe piles with a diameter, D, of 0.61 m (24 in) and an embedded length, L, of 21 m (69 ft) giving a slenderness ratio L/D = 34.4. The piles were subjected to two types of known loading; static and cyclic. The piles were instrumented with strain gauges to measure the bending moment along the piles. In addition the pile head deflection and pile head rotation was measured.

The piles were driven open-ended into fully saturated sand. In order to simulate the conditions at an offshore location, the water table was maintained above the ground surface during loading. For both the static and the cyclic loading a series of lateral loads were applied. From the measurements along the piles, a set of bending moment curves was obtained along with the associated boundary conditions for each type of loading. From these bending moment curves and the known boundary conditions $p-y$ curves were obtained.

The sand at the test site varied from clean fine sand to silty fine sand, both having high relative densities. The sand particles were found to be subangular with a large percentage of flaky grains. (Cox et al., 1974)

C.2.1 Formulation of *p–y* Curves

The original $p-y$ curve formulation consists of four parts assembled to one continuous piecewise differentiable curve, cf. Fig. C.4.

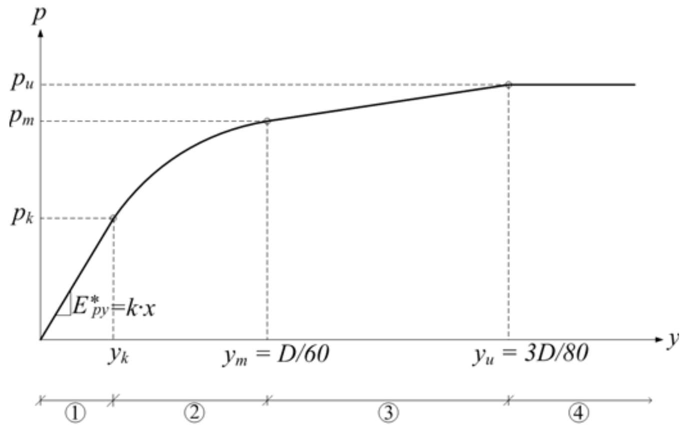

Figure C.4: *p-y* curve for static loading. After Reese et al. (1974)

The four parts of the $p-y$ curve is governed by:

1. Initial linear part; representing the elastic behaviour of the soil.
2. Parabolic part.
3. Sloping linear part.
4. Constant linear part; defined as the ultimate soil resistance and represents the plastic behaviour of the soil.

The establishment of a $p-y$ curve is described in the following and an illustration of the steps is shown in Fig. C.5.

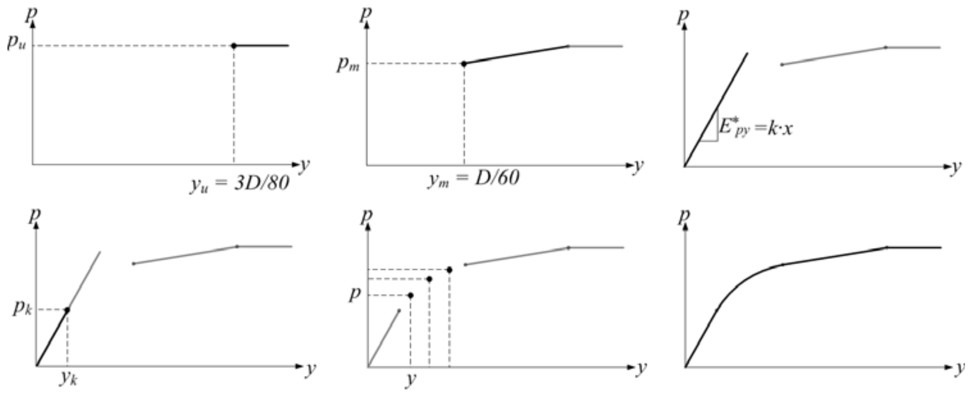

Figure C.5: Step by step procedure for creating a *p–y* curve.

Liniar Part of the *p–y* Curve

The ultimate soil resistance, p_u, can be calculated based on soil mechanics theory. The failure mode of the soil depends on the depth and therefore, p_u is calculated differently at shallow and deep depth. The tests at Mustang Island showed disagreement between the calculated ultimate soil resistance and the measured. The ultimate resistance is therefore adjusted according to Eq. C.1.

$$p_u = A \cdot p_c \tag{C.1}$$

Where:

- A is an empirical adjustment coefficient dependent on the type of loading, i.e. static or cyclic loading, cf. Fig. C.6. A was found as the ratio between the measured ultimate resistance and the calculated ultimate resistance for the Mustang Island tests. [-]
- p_c is the theoretical ultimate soil resistance [F/L]

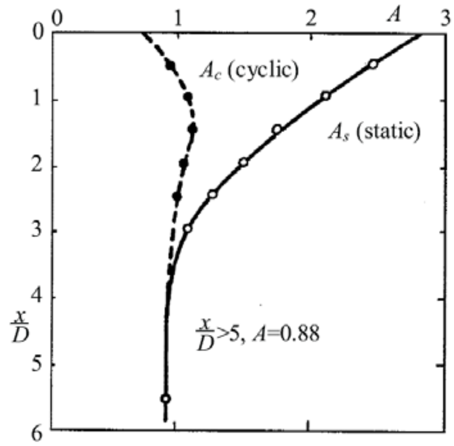

Figure C.6: A-coefficient. (Reese et al., 1974)

At shallow depth a wedge is assumed to form in front of the pile and the theoretical ultimate resistance, p_{cs}, is calculated using the free body shown in Fig. C.7. The total ultimate lateral resistance, F_{pt}, on the pile section is equal to the passive force, F_p, minus the active force, F_a.

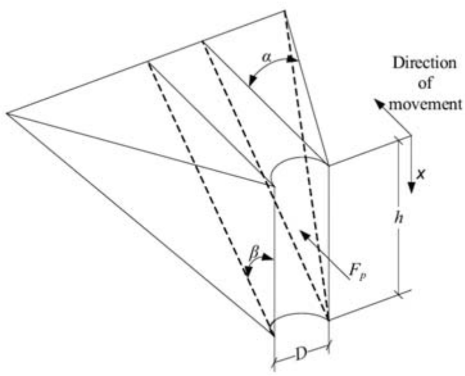

Figure C.7: Failure mode at shallow depth. After Reese et al. (1974)

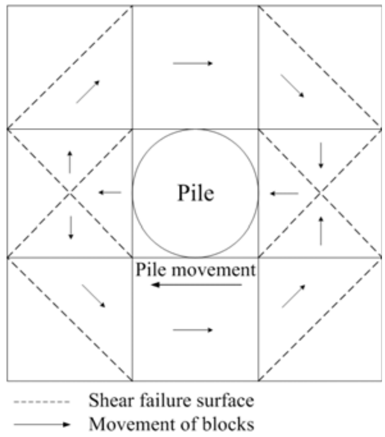

Figure C.8: Failure mode at deep depth. After Reese et al. (1974)

The passive force can be calculated from the geometry of the wedge when assuming that the Mohr-Coulomb failure theory is valid for the sand. The active force is computed from Rankine's theory using the minimum coefficient of active earth pressure. By using the Rankine theory the pile surface is assumed smooth, hence, no tangential forces occurs at the pile surface. The ultimate resistance per unit length of the pile at shallow depth, p_{cs}, is then found by differentiating the total force, F_{pt}, with respect to the depth, x, which gives Eq. C.2. (Reese et al., 1974)

$$\begin{aligned} p_{cs} = & \gamma' \cdot x \cdot \left(\frac{K_0 \cdot x \cdot \tan\varphi_{tr} \cdot \sin\beta}{\tan(\beta - \varphi_{tr}) \cdot \cos\alpha} \right. \\ & + \frac{\tan\beta}{\tan(\beta - \varphi_{tr})} \cdot (D + x \cdot \tan\beta \cdot \tan\alpha) \\ & \left. + K_0 \cdot x \cdot \tan\beta \cdot (\tan\varphi_{tr} \cdot \sin\beta - \tan\alpha) - K_a \cdot D \right) \end{aligned} \tag{C.2}$$

Where:

γ'	is the effective unit weight of the sand [F/L^3]
K_0	is the coefficient of horizontal earth pressure at rest, $K_0 = 0.4$
x	is the depth [L]
φ_{tr}	is the internal angle of friction based on triaxial tests [°]
β	is an angle of the wedge, cf. Fig. C.7 [°]
α	is an angle of the wedge, cf. Fig. C.7 [°]
D	is the diameter of the pile [L]
K_a	is the Rankine coefficient of minimum active earth pressure [-]

The angles, β and α, which describes the spread of the wedge, and the Rankine coefficient of minimum active earth pressure, K_a, are defined as:

$$\beta = 45^\circ + \frac{\varphi_{tr}}{2}$$
$$\alpha = \frac{\varphi_{tr}}{2}$$
$$K_a = \tan^2(45^\circ - \frac{\varphi_{tr}}{2})$$

At deep depth the soil failure mechanism is assumed to be a horizontal flow around the pile as shown in Fig. C.8. In this model it is assumed that the cylindrical pile can be simulated by a rigid block of material. Using the failure model shown in Fig. C.8 the ultimate soil resistance at deep depth, p_{cd}, can be calculated by Eq. C.3. (Reese et al., 1974)

$$p_{cd} = K_a \cdot D \cdot \gamma' \cdot x \cdot (\tan^8 \beta - 1) + K_0 \cdot D \cdot \gamma' \cdot x \cdot \tan \varphi_{tr} \cdot \tan^4 \beta \qquad \text{(C.3)}$$

The ultimate resistance as a function of depth for piles with diameters of 1 m and 4 m, respectively, are shown in Fig. C.9. The circles define the transition depth in which the ultimate resistance based on the two failure modes are identical. Above the transition depth Eq. C.2 for p_{cs} at shallow depth should be used and below the transition depth Eq. C.3 for p_{cd} should be used.

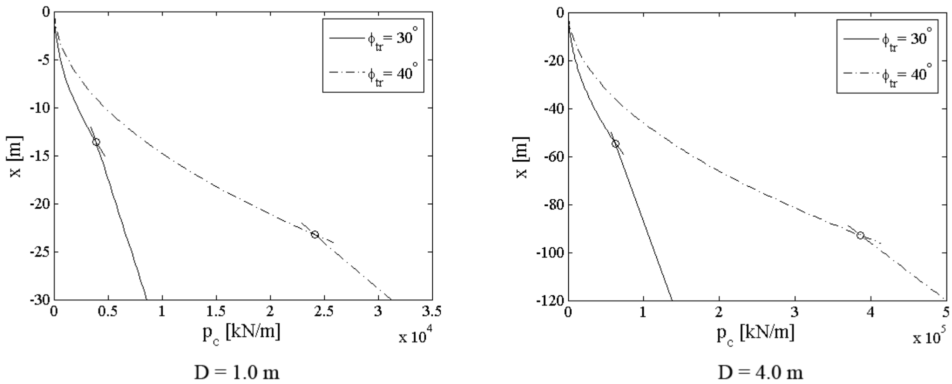

Figure C.9: Ultimate resistance, p_c, as a function of depth. $\gamma' = 10$ kN/m^3 has been used to plot the figures. The transition depths are marked with circles.

As can be seen in Fig. C.9 the transition depth increases with the pile diameter and the internal angle of friction. Therefore, for piles with small slenderness ratio the transition depth might appear far beneath the pile toe. The beginning of the ultimate linear part is defined by the deflection, y_u given by Eq. C.4.

$$y_u = \frac{3D}{80} \qquad \text{(C.4)}$$

Sloping Linear Part of the *p–y* Curve

The next step in creating the $p-y$ curve is to find the point (y_m,p_m), cf. Fig. C.5. The soil resistance per unit length, p_m, can be found using Eq. C.5.

$$p_m = B \cdot p_c \tag{C.5}$$

Where:
B is an empirical adjustment factor based on the Mustang Island tests, which varies for static and cyclic loading, cf. Fig. C.10 [-]

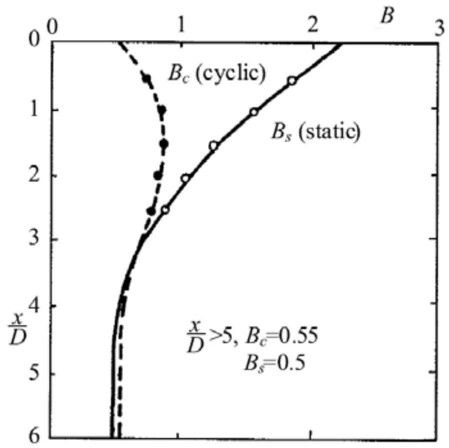

Figure C.10: B-coefficient. (Reese et al., 1974)

The corresponding deflection, y_m, is found by Eq. C.6.

$$y_m = \frac{D}{60} \tag{C.6}$$

Initial and Parabolic Parts of the *p–y* Curves

The initial linear part of the $p-y$ curve is generated with use of the initial modulus of subgrade reaction, k, cf. Eq. C.7.

$$p_1(y) = k \cdot x \cdot y \tag{C.7}$$

The line is thereby defined by the initial stiffness $E^*_{py} = k \cdot x$. Reese et al. (1974) suggested the value of k to be dependent on the internal angle of friction/relative density for the sand. The values of k are recommended for sands below the water table and based on large-scale experiments with static and cyclic loading. For loose sand k =5.4 MN/m^3 (20 lbs/in^3), for medium sands k =16.3 MN/m^3 (60 lbs/in^3), and for dense sands k =34 MN/m^3 (125 lbs/in^3).

The parabolic part of the $p-y$ curve is to be fitted between the points (y_k,p_k) and (y_m,p_m), cf. Fig. C.4, with the parabola in Eq. C.8.

$$p_2(y) = C \cdot y^{\frac{1}{n}} \tag{C.8}$$

The start and endpoint of the parabola must match the points (y_k,p_k) and (y_m,p_m), cf. Eqs. C.9 and C.10. Furthermore, it is required that the assembled $p-y$ curve must be differentiable in (y_m,p_m), cf. Eq. C.11.

$$p_1(y_k) = p_2(y_k) \tag{C.9}$$

$$p_2(y_m) = p_3(y_m) = p_m \tag{C.10}$$

$$\frac{\mathrm{d}p_2(y_m)}{\mathrm{d}y} = \frac{\mathrm{d}p_3(y_m)}{\mathrm{d}y} \tag{C.11}$$

When using that the soil resistance $p_3(y)$ can be expressed as a linear part with the slope $m = \frac{p_u - p_m}{y_u - y_m}$ the power of the parabola, n, and the coefficient C is calculated by Eqs. C.12 and C.13, respectively.

$$n = \frac{p_m}{m \cdot y_m} \tag{C.12}$$

$$C = \frac{p_m}{y_m{}^{\frac{1}{n}}} \tag{C.13}$$

The point of intersection between the initial straight part and the parabola (y_k,p_k) is then determined by Eqs. C.14 and C.15.

$$y_k = \left(\frac{C}{k \cdot x}\right)^{\frac{n}{n-1}} \tag{C.14}$$

$$p_k = C \cdot y_k{}^{\frac{1}{n}} \tag{C.15}$$

The rest of the parabola is computed using Eq. C.8 with values of y in the interval $y_k < y < y_m$.

C.3 *p-y* Curves in Design Regulations

Some modifications of the above described method for producing the $p-y$ curves are discussed in Murchison and O'Neill (1984). The validity of the modifications is verified by 14 static and cyclic tests on piles in cohesionless soils varying from very loose clayey sand to very dense clean sand. The piles were prismatic steel pipe, prismatic precast concrete, and tapered timber. The diameters varied between 0.05 m and 1.22 m and the internal angle of friction between 23^{o} and 42^{o}.

One of the modifications concerns the ultimate soil resistance. The ultimate soil resistance, given by Eqs. C.2 and C.3, is approximated using the dimensionless parameters C_1, C_2, and C_3, calibtated to match the results in Reese et al. (1974). Thereby, the minimum value of the resistance calculated by use of Eq. C.16 for shallow and deep depth, respectively, should be used. (Murchison and O'Neill, 1984)

$$p_c = \min \begin{cases} p_{cs} = (C_1 \cdot x + C_2 \cdot D) \cdot \gamma' \cdot x \\ p_{cd} = C_3 \cdot D \cdot \gamma' \cdot x \end{cases} \tag{C.16}$$

Where:

C_1, C_2 and C_3 are constants which are dependent on the internal angle of friction, φ_{tr}, and can be determined from Fig. C.11 or Eqs. C.17, C.18, and C.19 [-]

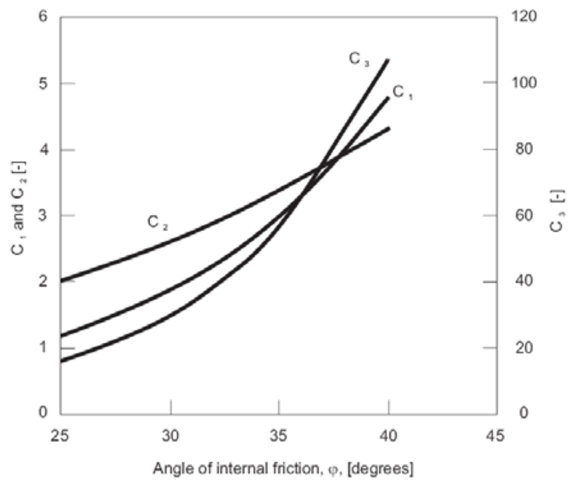

Figure C.11: Variation of the parameters C1, C2 and C3 as function of internal angle of friction. After (API, 1993)

The graphs for C_1, C_2, and C,3 have later been approximated by the following expressions (The University of Western Australia, 2000):

$$C_1 = 0.115 \cdot 10^{0.0405\varphi_{tr}} \tag{C.17}$$

$$C_2 = 0.571 \cdot 10^{0.022\varphi_{tr}} \tag{C.18}$$

$$C_3 = 0.646 \cdot 10^{0.0555\varphi_{tr}} \tag{C.19}$$

Another modification introduced by Murchison and O'Neill (1984) was to use a continuous hyperbolic tangent function to describe the $p-y$ curves, cf. Eq. C.20, instead of four different parts as the original curves. The equation is valid for circular piles.

$$p(y) = A \cdot p_c \cdot \tanh\left(\frac{k \cdot x}{A \cdot p_c} \cdot y\right) \tag{C.20}$$

Where:

$p(y)$	is the soil resistance per unit length [F/L]
p_c	is the calculated ultimate soil resistance given by Eq. C.16 [F/L]
A	is an empirical adjustment coefficient accounting for static or cyclic loading, cf. Eq. C.21, which is an approximation to the original graphs given in Fig. C.6 [-]
k	is the initial modulus of subgrade reaction [F/L^3]
x	is the depth [L]
y	is the lateral deflection [L]

$$A = \begin{cases} 0.9 & \text{for cyclic loading} \\ 3.0 - 0.8\frac{x}{D} \geq 0.9 & \text{for static loading} \end{cases} \tag{C.21}$$

By comparison of the original and different modified $p-y$ curves to results from various full-scale tests, Murchison and O'Neill (1984) proved, that the modifications gave more accurate $p-y$ curves than the original formulation. Therefore, in the design regulations API (1993) and DNV (1992) these modifications of the original formulations for the $p-y$ curves are employed.

In the design regulations the initial coefficient of subgrade reaction modulus, k, is recommended according to Fig. C.12. The curves only shows data for relative densities up to 80 % . This causes large uncertainties in the estimation of k for very dense sands, which is not a rare condition at offshore locations. The curve for soil below the water table is consistent with the findings of k in Reese et al. (1974) which is illustrated in Fig. C.12 with marked points. At offshore locations a relative density larger than 80 % is not rare.

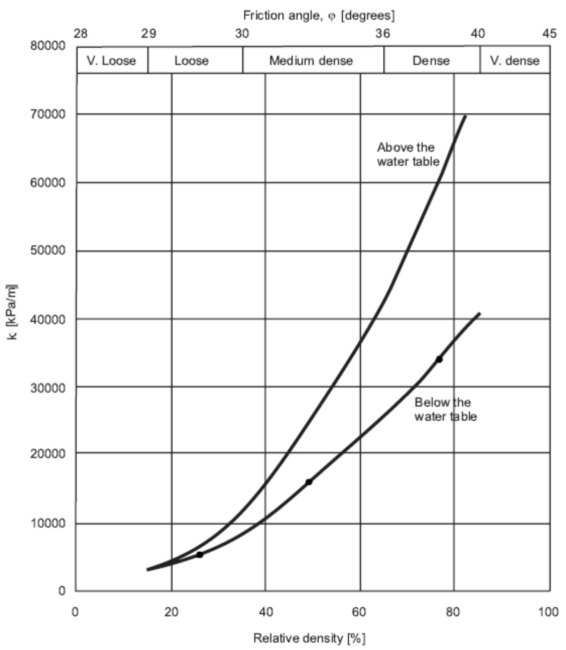

Figure C.12: Variation of the coefficient of subgrade reaction modulus, k, as a function of the relative density. The marked points on the curve below the water table represent the values of k recommended in Reese et al. (1974). After API (1993)

C.4 Alternative Formulation of the Ultimate Soil Resistance

Besides the expression for the ultimate soil resistance proposed by Reese et al. (1974), expressions for lower and upper bound solutions has been derived.

C.4.1 Lower Bound Solution for the Ultimate Soil Resistance

Hansen (1961) considers the state of equilibrium of a wedge moving forward and upward when the pile deflects horizontally corresponding to a Rankine failure at moderate depth for a smooth pile, cf. Fig. C.13. Contrary to the failure mode given by Reese et al. (1974) the wedge in the failure mode given by Hansen (1961) does not spread to the sides of the pile, cf. Fig. C.13. Thus, a smaller soil volume is assumed to fail and thereby, the calculated ultimate soil resistance is a lower bound value.

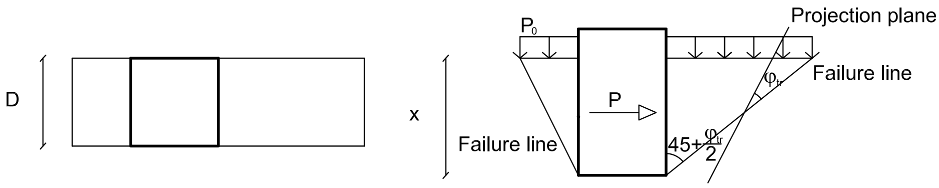

Figure C.13: Lower bound solution for smooth pile at moderate depth. After Hansen (1961); Gwizdala and Jacobsen (1992)

All acting forces is projected on the plane making an angle of φ_{tr} with the failure lines. This gives the expression for the passive horizontal resistance, p_p, given by Eq. C.22.

$$\begin{aligned} p_p =& P_0 \tan^2\left(45^\circ + \frac{\varphi_{tr}}{2}\right)\left(1 + \frac{x}{D}\frac{2K_0 \sin\varphi_{tr}}{\sin\left(45^\circ + \frac{\varphi_{tr}}{2}\right)}\right) \\ &+ \gamma' x \tan^2\left(45^\circ + \frac{\varphi_{tr}}{2}\right)\left(1 + \frac{x}{D}\frac{K_0 \sin\varphi_{tr}}{\sin\left(45^\circ + \frac{\varphi_{tr}}{2}\right)}\right) \\ &+ 2c \tan^2\left(45^\circ + \frac{\varphi_{tr}}{2}\right)\left(1 + \frac{x}{D} 2\sin\left(45^\circ + \frac{\varphi_{tr}}{2}\right)\right) \end{aligned} \tag{C.22}$$

Where:
p_p is the passive horizontal resistance [F/L^2]
c is the cohesion [F/L^2]

As the soil is cohesionless the expression can be reduced to contain only the first two terms. For the comparison of the tests without overburden pressure the first term can be neglected as well. To obtain the active horizontal resistance the sign of φ_{tr} is changed and for the case without overburden pressure the resistance is given by Eq. C.23. (Gwizdala and Jacobsen, 1992)

$$p_a = \gamma' x \tan^2\left(45^\circ - \frac{\varphi_{tr}}{2}\right)\left(1 - \frac{x}{D}\frac{K_0 \sin\varphi_{tr}}{\sin\left(45^\circ + \frac{\varphi_{tr}}{2}\right)}\right) \tag{C.23}$$

Where:
p_a is the active horizontal resistance [F/L^2]

The calculated ultimate soil resistance is then found as the passive earth pressure minus the active, cf. Eq. C.20.

$$p_c = p_p - p_a \tag{C.24}$$

Hereafter, the soil resistance $p(x,y)$ is calculated from the expression given in API (1993), cf. Eq. C.20.

C.4.2 Upper Bound Solution for the Ultimate Soil Resistance

An upper bound solution can be found by using a kinematic admissible solution. The only difference between this failure mode and the one considered by Reese et al. (1974) is the spread of the wedge to the sides of the pile. In Reese et al. (1974) the spread of the wedge, α, is considered to be $\varphi/2$. In the upper bound solution the spread is assumed to be φ_{tr}. Thus, the expression used to obtain the upper bound solution for the ultimate soil resistance is given by Eqs. C.2 and C.3 with $\alpha = \varphi_{tr}$.

? suggested to reduce the internal angle of friction in order to take the energy loss due to friction into account in the kinematic admissible solution, cf. Eq. C.25. In the upper bound solution $\alpha = \varphi_d$ is then used instead.

$$\tan\varphi_d = \frac{\sin\varphi_d \cdot \cos\psi}{1 - \sin\varphi_{pl} \cdot \sin\psi} \tag{C.25}$$

Where:

φ_{pl} is the plane angle of friction $\varphi_{pl} = 1.1 \cdot \varphi_{tr}$

C.5 Advantages and Limitations of the *p-y* Curve Method

The main advantage of using the current $p-y$ curve method is that it has a history of nearly 50 years and is implemented in computer programs such as PYGMY and SPLICE (The University of Western Australia, 2000; Clausen et al., 1984). The method has gained broad recognition due to the low failure rate of piles over several decades. The method is originally developed for the design of pile foundation of offshore platforms, but is now used in the design of monopiles as foundation of offshore wind turbines. This new use has led to awareness of the limitations of the design method.

C.5.1 Limitations of the *p–y* Curve Method

The $p-y$ curves for piles in cohesionless soils are based on very few full-scale tests conducted only on slender piles. The monopiles used today have diameters between 4 and 6 m, while the design method is only verified for piles with diameters up to 2 m. This means that when the $p-y$ curves are applied to the offshore wind turbine foundation, the design methodology is being used outside its verified range (Leblanc, 2009).

The slenderness ratio, L/D, for the full-scale test piles were 34.4 and for the monopiles installed today $L/D < 10$. This lower slenderness ratio causes the monopiles to have a more rigid than flexible behaviour in contrast to the full-scale test piles. This might have an effect on the initial stiffness of the curves. Another effect of the rigid behaviour compared to the flexible behaviour, is that the rigidity cause the pile to make a 'toe-kick' when rotating. This is in contradiction to the design method where the deflection at pile toe is considered to be zero. Further, the toe-kick produces shear stresses at the pile toe which will cause an increase of the total lateral resistance. A method for calculating the shear force as a function of the deflection is not developed.

For large-diameter monopiles the transition depth between the formulations for the ultimate soil resistance at shallow and deep depths, respectively, will most often be positioned under the pile toe. Hence, the ultimate soil resistance for shallow depths should be used, even though a large number of uncertainties are connected to the formulation inter alia because of the choice of failure mechanism. In the formulation given by Hansen (1961) a two dimensional case is analysed and the pile is assumed smooth, hence, no skin friction occurs and, thus, a Rankine failure mechanism is assumed. In reality the pile is neither smooth nor entirely rough as the assumption for a Prandtl failure mechanism. Therefore, the correct failure mechanism will be a combination of the two mechanisms. In Reese et al. (1974) the spread of the wedge in front of the pile is defined by the factor α. This factor is dependent of the void ratio, the internal angle of friction and the type of loading. However, in the formulation for the ultimate soil resistance only the dependency on the internal angle of friction is employed. Because of the rigid behaviour of the piles, the failure mode for the monopiles will be a combination of Rankine failure and stiff elastic zones as shown in Fig. C.14.

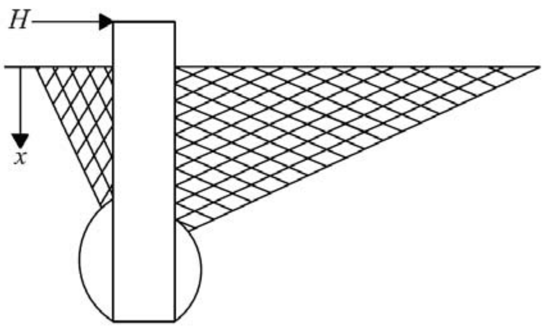

Figure C.14: Failure mode for the monopiles. A combination of Rankine failure and stiff elastic zones. (Brødbæk et al., 2009)

The $p-y$ curve method is designed primarily to evaluate the ultimate lateral capacity of the piles used in the foundation of offshore platforms. Because of this, the initial part of the $p-y$ curves has not been given mutch attention and the initial stiffness is considered independent of the pile properties, e.g. the pile diameter. According to API (1993) and DNV (1992) the initial stiffness is dependent on the internal angle of friction and varies linear with depth. However, Fan and Long (2005) and Sørensen et al. (2010) have proposed different expressions in which the initial stiffness also is dependent on the diameter of the pile and varies non-linear with the depth.

In the design regulations the effect of soil dilation is not considered and thereby, the effect of the volume changes of the the soil due to the deflection of the pile is not taken into account. Fan and Long (2005) analysed the effect of dilation on the ultimate soil resistance and found the dilation increases the strength of dense sand.

APPENDIX D

WINKLER MODEL APPROACH

The Winkler model approach is a widely used method for calculating the deflection of piles exposed to lateral loading and the approach is incorporated in the design regulations, e.g. API (1993) and DNV (1992). This appendix gives a description of the method and the application for the small-scale tests on laterally loaded piles carried out in the Geotechnical Engineering Laboratory at Aalborg University.

In the Winkler model approach the pile is modelled as an elastic beam on an elastic foundation. The soil is considered to consist of a series of independent soil layers with smooth horizontal boundaries. The soil response from each layer, i.e. from the elastic foundation, is represented by a spring with spring stiffness, E_{py}, given by means of non-linear $p-y$ curves. An Illustration of the Winkler model approach is shown in Fig. D.1. (Reese and Van Impe, 2001)

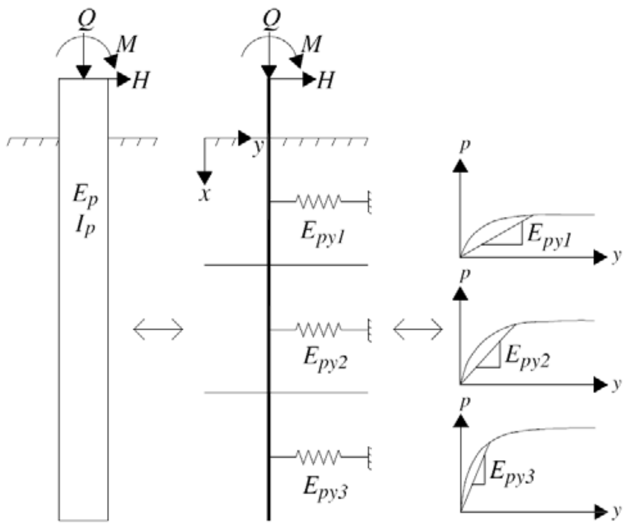

Figure D.1: The Winkler model approach with the pile modelled as an elastic beam element supported by non-linear uncoupled springs. After Sørensen et al. (2010)

The governing equation for solving the lateral deflection is derived from static equilibrium of an infinitesimal small element, dx, located at depth, x, subjected to lateral loading as shown in Fig. D.2. The sign convention shown in Fig. D.3 is employed. The applied loads and displacements are positive when acting to the right and applied moments and rotations are positive when acting clockwise.

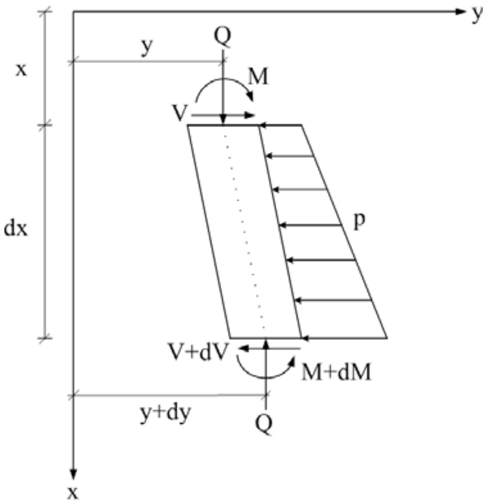

Figure D.2: Infinitesimal small element for deriving the governing equation. After Reese and Van Impe (2001)

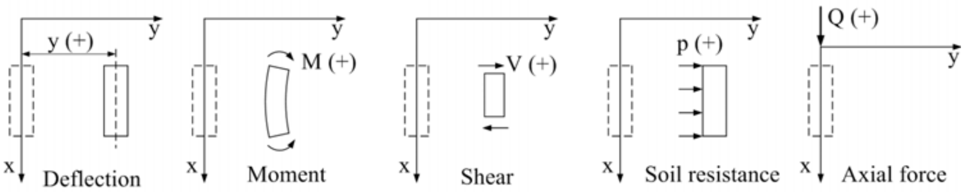

Figure D.3: Sign convention for deriving the governing equation. After Reese and Van Impe (2001)

Equilibrium of moments when the second order terms are neglected leads to Eq. D.1.

$$\begin{aligned} M + dM - M - V dx + Q dy &= 0 \\ \frac{dM}{dx} + Q\frac{dy}{dx} - V &= 0 \\ \frac{d^2M}{dx^2} + Q\frac{d^2y}{dx^2} - \frac{dV}{dx} &= 0 \end{aligned} \tag{D.1}$$

The following identities are noted:

$$M = E_p I_p \cdot \kappa \tag{D.2}$$

$$\frac{dV}{dx} = p \tag{D.3}$$

$$p = E_{py} \cdot y \tag{D.4}$$

When substituting Eqs. D.2 to D.4 into Eq. D.1, and using the kinematic assumption valid for the Bernoulli-Euler beam theory, $\kappa = \frac{d^2y}{dx^2}$, the governing differential equation is given by Eq. D.5. The equation describes the lateral deflection of the pile subjected to the lateral load, H, the moment, M, and the axial load, Q.

$$E_p I_p \cdot \frac{d^4y}{dx^4} + Q \cdot \frac{d^2y}{dx^2} - E_{py} \cdot y = 0 \tag{D.5}$$

Where:

y	is the lateral deflection of the pile at the depth x [L]
x	is the depth coordinate along the pile [L]
E_p	is the modulus of elasticity [F/L^2]
I_p	is the moment of inertia around the horizontal axis perpendicular to the pile axis [L^4]
Q	is the axial force [F]
E_{py}	is the modulus of subgrade reaction [F/L^2]

As the Bernoulli-Euler beam theory is used, shear strain, γ, is neglected in the governing equation (D.5). This is only admissible if the pile is relatively slender. For short and rigid piles the Timoshenko beam theory in which the shear strain is taken into account is preferable. However, comparison analysis performed by Sørensen et al. (2009) showed that when using the Bernoulli-Euler beam theory on a pile with a slenderness ratio of 5, the absolute difference in laterally deflection compared to the Timoshenko beam theory was approximately 0.18 % of the prescribed deflection. Due to this small difference, the use of Bernoulli-Euler beam theory is assumed valid when modelling piles with a slenderness ratio of approximately 5.

The three parts of Eq. D.5 are shown in Fig. D.4. The first part of Eq. D.5 accounts for the bending stiffness of the pile, and the second part includes the effects of the axial force. The arrows along the pile indicates the influence on the soil. The third part describes the pile-soil interaction, and the arrows along the pile indicates the influence of the soil on the pile.

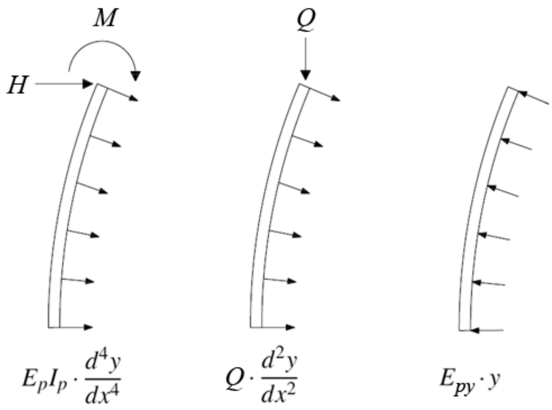

Figure D.4: The three parts of Eq. D.5.

The axial force, Q, may be a function of x depending on whether or not the load transfer in the axial direction is taken into account. The modulus of subgrade reaction, E_{py}, which describes the interaction stiffness between the pile and the soil depends on both the depth, x, and the deflection, y.

In the derivation of the governing equation the following assumptions have been used. (Reese and Van Impe, 2001)

- The pile is straight and has a uniform cross section.
- The pile has a longitudinal plane of symmetry in which loads and reactions are placed.
- The pile material is homogeneous and isotropic.
- The proportional limit of the pile material is not exceeded, i.e. only plastic deformation occurs in the pile.
- Young's modulus of the pile material is the same in tension and compression.
- The deflection of the pile is small.
- The pile is not subjected to dynamic loading.
- Deflections due to shearing stresses are small.

D.1 Winkler Model Set-Up

The model is set up in the program MATLAB version 7.0 with use of the finite element toolbox CALFEM version 3.4 described in Austrell et al. (2004). The different files for modelling the test setup with different formulations for the soil resistance can be seen on the enclosed CD in the folder "Winkler model".

In CALFEM defined system functions for the setting up, solving, and elimination of systems of equations are used. The system functions concern the linear system of equations $\underline{\underline{K}}\,\underline{a} = \underline{f}$ where $\underline{\underline{K}}$ is the global stiffness matrix, $\underline{a}$ is the global displacement vector, and $\underline{f}$ is the global load vector.

In the experiments the vertical force acting on the pile originating from the added pressure in the tank is neglected. Hence, the second part of the governing equation, Eq. D.5, regarding column effects is not taken into account, and the differential equation used in the Winkler model is given by Eq. D.6. This is considered an acceptable approximation because of the rigidity of the pile.

$$E_p I_p \frac{d^4 y}{dx^4} - E_{py} \cdot y = 0 \tag{D.6}$$

D.1.1 Element Geometry

In CALFEM prescribed routines for different element types are given. To model the pile two-noded beam elements with three degrees of freedom (d.o.f.) in each node are employed. An illustration of the element is shown in Fig. D.5 where four of the d.o.f. represent translation and the remaining two represent rotation.

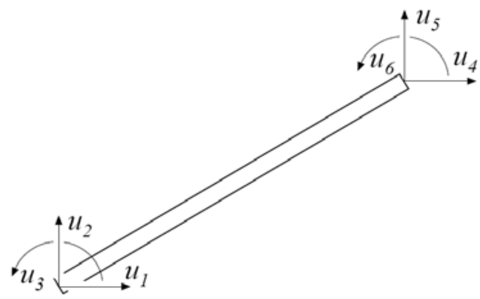

Figure D.5: Two-noded beam element with three d.o.f. in each node, two translational and one rotational respectively. (Austrell et al., 2004)

When using a beam element both Bernoulli-Euler and Timoshenko beam theory can be employed. In the model set-up only Bernoulli-Euler elements are used. Based on the comparison analysis preformed by Sørensen et al. (2009) a total of 100 elements along the pile below the soil surface are selected. The length of each element are identical along the pile. Above the soil surface the number of elements are chosen so the length of each element is equal in the entire pile.

The surrounding soil is modelled as horizontal beam elements. The joints between the pile and the beam elements are made with hinges where no bending moments can be transferred. This way, the supporting beam elements will represent the soil resistance because only the lateral resistance is transferred. The model geometry for the Winkler approach is shown in Fig. D.6.

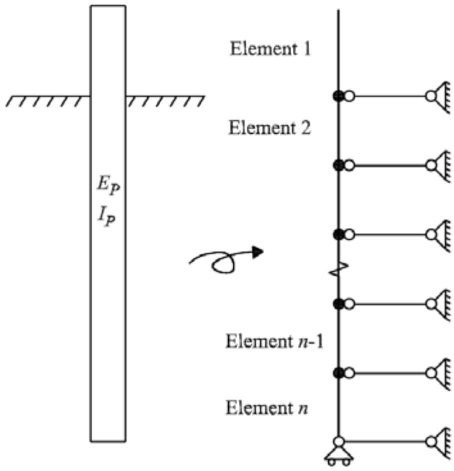

Figure D.6: Model geometry for the Winkler approach. The solid circles indicate the nodes and the non-solid circles indicate the hinges. After Sørensen et al. (2009)

In reality the soil resistance along the pile varies non-linearly. When using the Winkler model approach the soil resistance is calculated as distinct values for each node in the beam. This value is then assumed constant for half of each of the beam elements connected by the node, cf. Fig. D.7. This distribution is only a good approximation to the real non-linear distribution of the soil resistance if the pile is divided into a relatively large number of beam elements. The approximation of the soil resistance for the element at the soil surface and the element at the pile toe is highly inaccurate. However, these errors minimises when using a relative large number of elements.

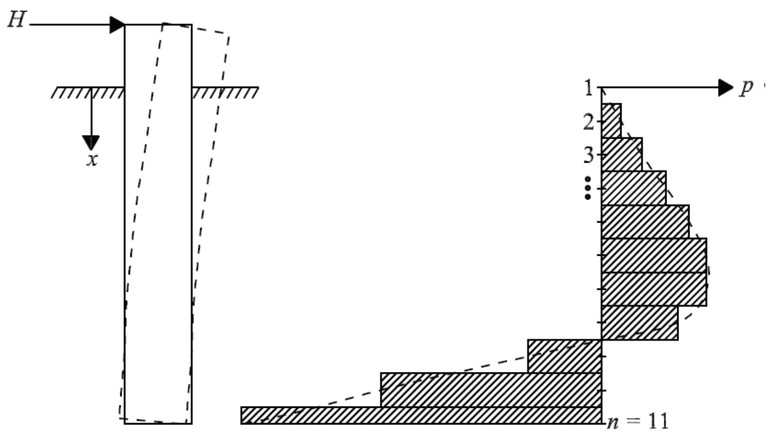

Figure D.7: Assumed soil resistance along the pile when the pile is divided into 11 elements. (Sørensen et al., 2009)

D.1.2 Procedures for Solving the Non-Linear Set of Equations

To find the correct spring stiffness in the Winkler model approach the non-linear expression for the $p-y$ curves are used. Because of the non-linearity it is necessary to incorporate an iterative procedure to find the spring stiffness when modelling the resistance of the soil.

In the laboratory tests the lateral deflection of the pile was achieved by applying a known deflection, Δy, at an eccentricity, e, cf. Fig. D.8. Therefore, an iterative procedure following the same procedure is used in the calculations.

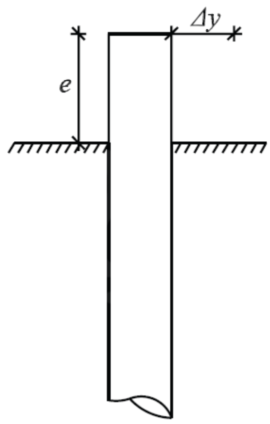

Figure D.8: Prescribed deflection, Δy, applied to the pile at the eccentricity, e. (Sørensen et al., 2009)

The modulus of subgrade reaction, E_{py}, is used to estimate the deflection of the pile. The first estimate of the pile deflection is calculated by using the initial stiffness of the $p-y$ curves, E^*_{py}, as spring stiffness. Hence, an estimate of the pile deflection is obtained, and a new value of E_{py} is derived from the expression for $p-y$ curves. The new E_{py} is used as spring stiffness and yet another estimate of the pile deflection is obtained. This procedure is repeated until the difference between two estimates of the pile deflection in all nodes is less than 0.005 ‰ of the prescribed deflection.

D.1.3 Overburden pressure

The overburden pressure is taken into account by the method proposed by Georgiadis (1983). Originally the method is proposed for calculating the soil resistance in layered soils. The different soil layers are incorporated in the Winkler model by introducing an equivalent system with fictive depths, x'. An example of the equivalence with two soil layers are shown in Fig. D.9.

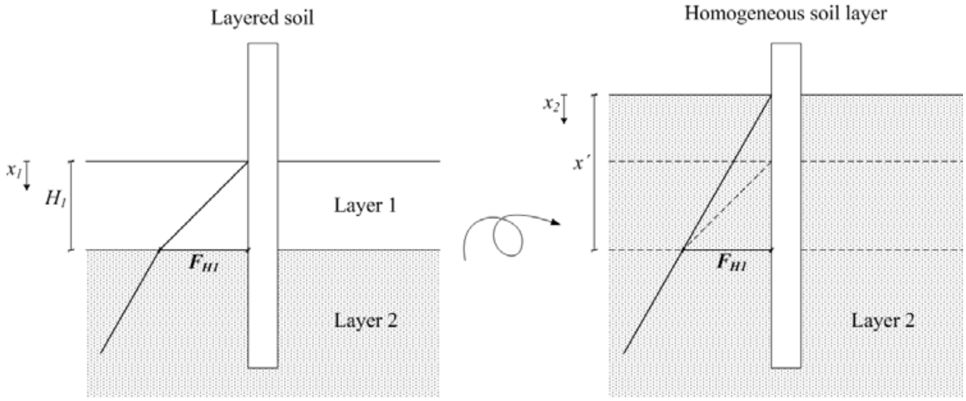

Figure D.9: Principle for calculation of soil resistance in the second layer in a two layered soil. After Georgiadis (1983)

To determine the soil resistance in the second layer correctly, the horizontal capacity, F_H, of the two systems should be equivalent. This is obtained by equating the ultimate soil resistance integrated with the depth for the two systems, cf. Eq. D.7.

$$F_{H1} = \int_0^{H_1} p_{u,layer1}\, dx_1 = \int_0^{x'} p_{u,layer2}\, dx_2 \tag{D.7}$$

Where:

H_1	is the thickness of layer 1 [L]
$p_{u,layer1}$	is the ultimate soil resistance calculated based on the soil parameters in layer 1 [F/L]
x_1	is the depth below soil surface for layer 1 [L]
x'	is the extra depth in the equivalent system [L]
$p_{u,layer2}$	is the ultimate soil resistance calculated based on the soil parameters in layer 2 [F/L]
x_2	is the depth below soil surface for layer 2 in the equivalent system [L]

By solving Eq. D.7 the extra depth, x', is found and the soil resistance in the second layer can be calculated based on the standard formulations in API (1993) including the added depth x'.

For the laboratory tests with overburden pressure the procedure for finding the fictive depth, x', is slightly modified. Because x' is calculated from the soil surface the ultimate soil resistance at the soil surface is equated directly instead of the ultimate soil resistance integrated with the depth, cf. Eq. D.8. When determining the fictive depth from Eq. D.8 no attention is attached to the equivalence of the effective stresses. The equivalent systems are shown in Fig. D.10.

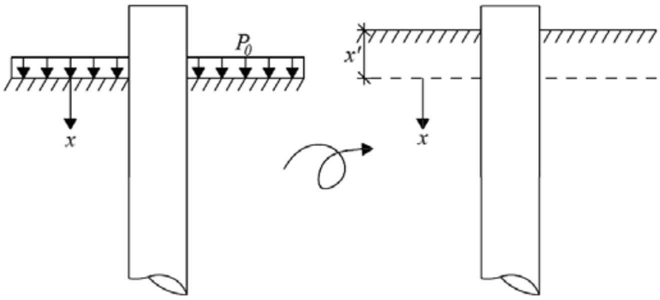

Figure D.10: To the left, the system with the overburden pressure, P_0, and to the right, the equivalent system with the fictive depth x'. (Sørensen et al., 2009)

$$
\begin{aligned}
p_{cs}^{P_0} &= p_{cs}^{x'} \\
C_2 \cdot D \cdot P_0 &= \left(C_1 \cdot x' + C_2 \cdot D\right) \cdot \gamma' \cdot x' \qquad \text{(D.8)}
\end{aligned}
$$

Where:

$p_{cs}^{P_0}$	is the ultimate soil resistance for the system with overburden pressure [F/L]
$p_{cs}^{x'}$	is the ultimate soil resistance for the equivalent system [F/L]
C_1, C_2	are constants given in API (1993) [-]
D	is the diameter of the pile [L]
γ'	is the effective unit weight of the soil [F/L^3]

After determination of the fictive depth the ultimate soil resistance can be approximated by entering $x + x'$ into the formula given in API (1993) for the ultimate soil resistance at shallow depth, cf. Eq. D.9.

$$
p_c = \min \begin{cases} p_{cs} = (C_1 \cdot (x + x') + C_2 \cdot D) \cdot \gamma' \cdot (x + x') \\ p_{cd} = C_3 \cdot D \cdot \gamma' \cdot (x + x') \end{cases} \qquad \text{(D.9)}
$$

The $p - y$ curves for sand are then found by Eq. D.10.

$$
p(y) = A \cdot p_c \cdot \tanh\left(\frac{k \cdot (x + x')}{A \cdot p_c} \cdot y\right) \qquad \text{(D.10)}
$$

Where:

A	is a factor accounting for static or cyclic loading [-]
y	is the lateral pile deflection [L]

Thereby, the initial stiffness of the $p-y$ curves, E^*_{py}, is estimated by Eq. D.11.

$$E^*_{py} = k \cdot (x + x') \tag{D.11}$$

Where:
k is the initial modulus of subgrade reaction [F/L^3]

When increasing the pressure in the upper part of the pressure tank, not only the soil under the membrane but also the part of the pile above the soil surface is influenced by the additional pressure. Thus, the pile is subjected to an even pressure at the circumference but because of the stiffness of the pile, this has no effect on the pile-soil interaction. The pressure will cause an axial pressure on the pile head acting like an added mass. This added mass will increase the effective stresses in the area near the pile. This effect is not included in the design regulations and therefore, it is not incorporated in the constructed Winkler model.

APPENDIX E

SMALL–SCALE TESTS MODELLED IN FLAC^{3D}

The piles used in the small-scale tests on laterally loaded non–slender monopiles in sand are instrumented with three displacement transducers and one load transducer, all located above soil surface. As no strain gauges were attached to the piles, an evaluation of the moment distribution, pile deflection, and soil resistance below soil surface is not possible from the measurements alone. Thus, FLAC^{3D}-models are set up to match the small-scale test and when the models are calibrated the output is used in the evaluation of the pile and soil behaviour. In this appendix the modelling of the tests are described including short descriptions of the basic features in FLAC^{3D}. The appendix is based on FLAC^{3D} 3.1 manual (2006)

In total six FLAC^{3D}-models are set up to match the small-scale tests carried out in the pressure tank at Aalborg University, cf. Thomassen and Roesen (2010). The modelling programme is shown in Tab. E.1. The six FLAC^{3D}-models can be found on the enclosed CD in the folder "FLAC models".

Table E.1: Programme for the FLAC^{3D} models.

		D [mm]	L/D [-]	P_0 [kPa]	Reference
Model 1	(Test 1)	100	5	0	App. M
Model 2	(Test 2)	100	5	50	App. N
Model 3	(Test 3)	100	5	100	App. O
Model 4	(Test 4)	40	5	0	App. P
Model 5	(Test 5)	40	5	50	App. Q
Model 6	(Test 6)	40	5	100	App. R

E.1 FLAC^{3D}

FLAC^{3D} is a commercial explicit finite difference program. It allows for numerical study of the mechanical behaviour of a continuous three-dimensional medium as it reaches equilibrium or steady plastic flow.

The mechanical behaviour is derived by using a mathematical model for setting up equations and using numerical implementation in order to solve the equations. In the mathematical model, the mechanics of the medium is derived from laws of motion, definition of strain, and use of constitutive equations for the material. The resulting expression for the behaviour is a set of partial differential equations relating mechanical (stress) and kinematic (strain rate, velocity) variables. These equations are to be solved for specific geometries, properties, boundary and initial conditions.

In the numerical formulation, the solution of the differential equations is characterized by the following three approaches:

- **Finite difference approach**: All first-order space and time derivatives of a variable are approximated by finite differences by assuming linear variations of the variables over time and space.
- **Discrete-model approach**: The continuous medium is replaced by a number of discrete elements in which all forces involved are concentrated at the nodes.
- **Dynamic-solution approach**: The inertial terms in the equation of motion are used as numerical means to reach the equilibrium state of the system, i.e. the program steps forward until equilibrium is reached in the nodes.

By means of these approaches the laws of motion for the continuum are transformed into discrete forms of Newton's law at the nodes. The resulting system of ordinary differential equations is then solved numerically using an explicit finite difference approach in time.

E.2 Modelling Procedure

The generation of the model and the finite difference calculations are carried out stepwise as listed below. In the following sections the different modelling steps are described in more detail.

1. The geometry of the model generated in the following order:
   - Generation of soil.
   - Generation of interfaces and attaching them to the soil.
   - Generation of pile and installation into the soil.
2. When the geometry is generated the boundary conditions are assigned and the initial stresses in the model are generated.
3. The model is brought to equilibrium with both the pile and the soil having the material properties of the soil and the pile modelled as smooth.
4. After equilibrium is reached the correct pile and interface properties are assigned and damping is employed in the model. Again the model is brought to equilibrium.
5. After the second equilibrium is reached all displacements are reset to zero.
6. The lateral load is applied as lateral velocities at the eccentricity $e = 370$ mm at the center nodes.
7. During the calculations, the total force, H, and displacement, y, along the pile are recorded along the pile. The bending moment M, and soil pressure, p, are calculated based on the recorded stresses.

E.3 Geometry and Material Properties

The geometry of the model is set to match the experimental setup in the laboratory. Because of axis symmetry, the model is simplified and only half of the test setup is modelled. When generating the geometry, a quarter of the test setup is defined and then reflected to generate the remaining model part. The soil and pile is generated by use of predefined zone elements to which different material models and properties can be assigned. In order to model a correct pile-soil interaction an interface is generated between the soil and the pile. The different dimensions used to set up the geometry in the FLAC^{3D}-models, enclosed on the CD, are shown in Fig. E.1.

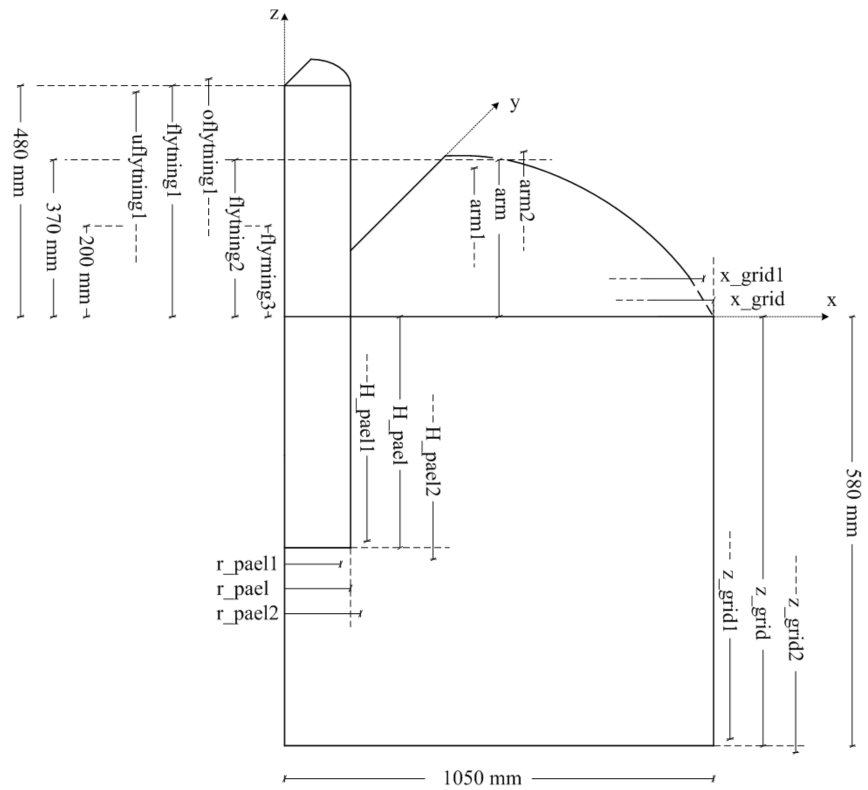

Figure E.1: Dimensions for the geometry in the models.

E.3.1 Generation of the Soil

The soil is generated by use of cylindrical shell zone elements, cf. Fig. E.2. Because large variations in strains and stresses will occur in the soil near the pile a finer mesh is employed in this area. For the models with a 40 mm pile the soil surrounding the pile is divided into 40 zone levels. To ensure that $p-y$ curves for the six models can be compared in the same levels, the soil in the models with a 100 mm pile is divided into 50 zone levels. Below the pile the soil is divided into three zone levels. The soil is divided into three plus seven elements along the radius and seven elements along the quarter of the perimeter. The generated soil zones for the model with a 100 mm pile is shown in Fig. E.3.

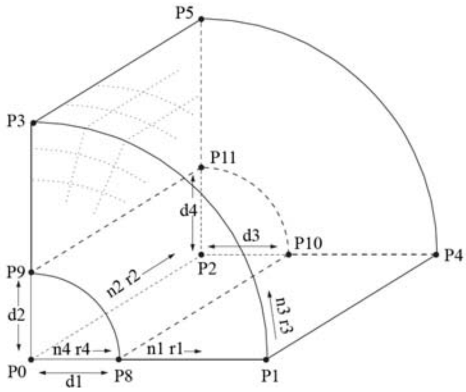

Figure E.2: Predefined cylindrical shell element in FLAC^{3D}. (FLAC^{3D} 3.1 manual, 2006)

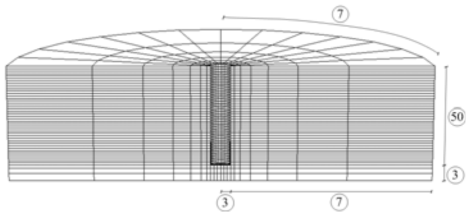

Figure E.3: The generated soil zones for the models with a 100 mm pile. The numbers in circles indicate the number of elements in the given parts.

Soil Properties

The soil properties for in the six models are set equal to the findings from the laboratory tests, cf. Tab. E.2.

Table E.2: Soil properties determined from the six laboratory tests and employed in the FLAC^{3D} models. The elasticities written in paranteses are found by means of the numerical model.

	D [mm]	P_0 [kPa]	φ_{tr} [°]	ψ_{tr} [°]	I_D [-]	γ' [kN/m^3]	E_0 [MPa]
Model 1	100	0	53.7	19.6	0.86	10.3	(4.0)
Model 2	100	50	50.3	19.0	0.89	10.4	38.24
Model 3	100	100	47.7	18.3	0.90	10.4	55.61
Model 4	40	0	54.4	20.4	0.91	10.4	(2.0)
Model 5	40	50	50.4	19.1	0.89	10.4	38.6
Model 6	40	100	48.0	18.6	0.91	10.4	57.2

For the tests without overburden pressure the low stresses lead to large uncertainties in the calculation of the elasticity modulus of the soil. Thus, in the FLAC^{3D}-models without overburden pressure the initial tangential elasticity modulus, E_0, is calibrated by means of the numerical model, so the load-deflection relationship obtained in the numerical models resemble the test results as good as possible.

The soil in the pressure tank had a limited depth of 0.58 m. Because of this relative small depth, the variation in effective stresses trough the layer is small as well.

Thus, the soil parameters in the FLAC^{3D} models are assumed constant with depth. In all six models the cohesion, c, is 0.1 kPa, and Poissons ratio, ν, is 0.23.

The coefficient of horizontal earth pressure at rest, K_0, the bulk modulus K, and the shear modulus, G, are calculated by Eqs. E.1 to E.3.

$$K_0 = 1 - \sin\varphi_{tr} \tag{E.1}$$

$$K = \frac{E}{3\cdot(1-2\cdot\nu)} \tag{E.2}$$

$$G = \frac{E}{2+2\cdot\nu} \tag{E.3}$$

Where:
φ_{tr} is the internal angle of friction [°]
E is the elasticity modulus [F/L^2]

E.3.2 Generation of Interfaces

In order to model the pile-soil interaction, an interface is generated between the pile and the soil. The interface elements allow gapping and slipping between the soil and the pile. They are modelled by use of the standard interface feature included in FLAC^{3D} which uses triangular elements. By default two interface elements are generated for each zone element.

The interfaces are generated along the sides adjacent to the side and bottom of the pile. In Fig. E.4 the dimensions for generating the interfaces are shown. The generated interfaces are one-sided and attached to the soil. In Fig. E.6 the interface for a pile with diameter D = 100 mm is shown.

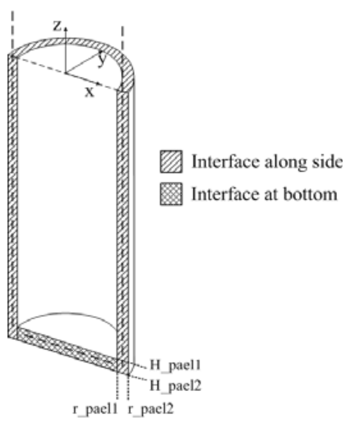

Figure E.4: Boundaries for interface generation. At the nodes within the hatched areas an interface is generated.

Each interface node is assigned an associated representative area based on weighted distribution of each interface element, cf. Fig. E.5. This way, a shear and a normal force for each individual node can be calculated.

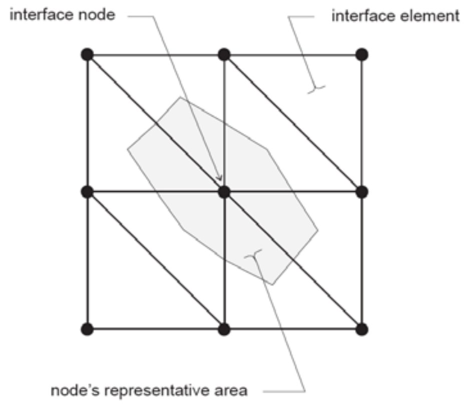

Figure E.5: Interface elements employed in FLAC^{3D}. (FLAC^{3D} 3.1 manual, 2006)

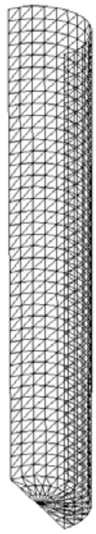

Figure E.6: Interface elements between the soil and the pile for the pile with D = 100 mm.

When another zone surface (target face) than the one the interface is attached to comes into contact with the interface element, the contact is detected at the interface node and is characterised by normal and shear stiffnesses as well as sliding properties, cf. Fig. E.7. The normal direction of the interface force is determined by the orientation of the target face.

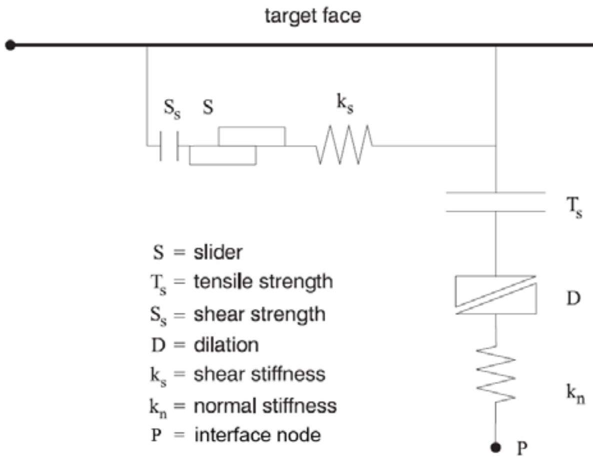

Figure E.7: Components of the bonded interface constitutive model. (FLAC^{3D} 3.1 manual, 2006)

The constitutive model employed for the interfaces is defined by a linear Coulomb shear strength criterion that limits the shear force acting at an interface node when the limit is reached. Further more, the criterion limits the normal and shear stiffness, and dilation angle that causes an increase in effective normal force on the target face after the shear-strength limit is reached.

Interface Properties

The interface properties are very important for the interaction between the soil and the pile, and thereby, the basis for getting the load-deflection curves to match the curves obtained from the laboratory tests. The interfaces have the properties of friction, cohesion, dilation, normal and shear stiffness, and tensile and shear bond strength, cf. Fig. E.7. By default the tensile and shear bond strengths are not activated.

The interface properties are calibrated by means of the numerical models. When using the interface properties as listed in Tab. E.3, the load-deflection curves are found to be similar to the curves obtained in the laboratory tests.

Table E.3: Interface properties calibrated by means of the numerical models. E_0 is the Young's modulus of the soil, cf. Tab. E.2.

Friction	φ_{int}	[°]	30
Cohesion	c_{int}	[kPa]	0.1
Dilation	ψ_{int}	[°]	0
Normal stiffness	k_n	[N/mm^2]	$100 \times E_0$
Shear stiffness	k_s	[N/mm^2]	$100 \times E_0$

E.3.3 Generation of the Pile

In contrast to the closed-ended pipe piles employed in the laboratory tests, the piles in the FLAC^{3D}-models are modelled as solid cylinders by use of cylindrical zone elements, cf. Fig. E.8. The pile grid is initially created separately and later moved into the soil and in contact with the interfaces. Hereby it is possible to group the pile elements, in one group, and to specify pile nodes for the computation of the bending moment. The advantage of grouping the zone elements is a simplification of the installation of the pile and the assignment of the material model and properties can be done by one command instead of individual commands for each part of the pile.

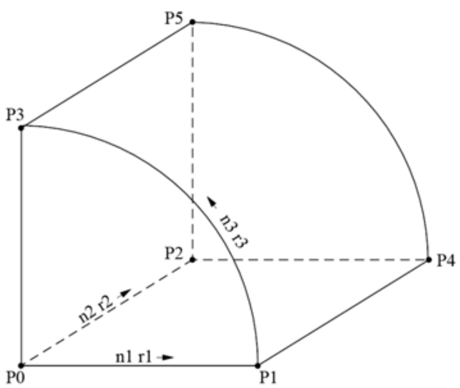

Figure E.8: Predefined cylindrical zone element in FLAC^{3D}. (FLAC^{3D} 3.1 manual, 2006)

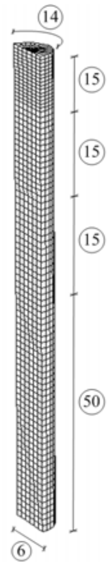

Figure E.9: Pile grid for the 100 mm pile. The numbers in circles indicate the number of elements in the given parts.

In order to ensure that nodes are generated at levels equal to the levels of the displacement transducers in the laboratory tests, the pile is generated in four parts; three above soil surface and one below, cf. Fig. E.9. Between the levels of the displacement transducers the pile is divided into 15 zone levels. Below the soil surface the zone elements for the pile is set to match the elements of the soil, i.e. the pile is divided into 40 zone levels for the 40 mm pile and 50 zone levels for the 100 mm pile. For both pile sizes, the diameter and perimeter of the pile is divided into six and fourteen zones, respectively. In Fig. E.9 the zone levels for the 100 mm pile is shown.

Pile Properties

Because the piles are modelled as solid cylinders instead of hollow piles as the ones used in the laboratory, an equivalent bending stiffness and density is required, cf. Fig. E.10. Based on this equivalence a reduced elasticity modulus and density for the modelled piles are given by Eqs. E.4 and E.5, respectively.

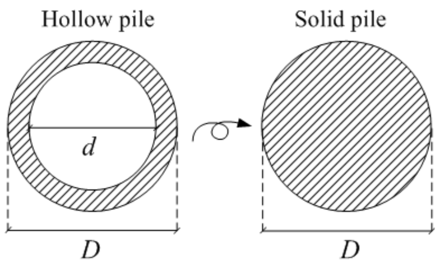

Figure E.10: Cross-section of a hollow pile as the ones used in the laboratory and a solid pile as modelled in FLAC^{3D}.

$$E_{solid} = \frac{E_{hollow} \cdot I_{hollow}}{I_{solid}} \tag{E.4}$$

$$\rho_{solid} = \frac{\rho_{hollow} \cdot A_{hollow}}{A_{solid}} \tag{E.5}$$

Where:

I	is the second moment of inertia of the pile [L^4]
	$I_{solid} = \frac{\pi}{64} \cdot D^4$ and $I_{hollow} = \frac{\pi}{64} \cdot (D^4 - d^4)$
ρ	is the density of the pile [M/L^3]
A	is the area of the pile [L^2]
$_{hollow}$	defines a parameter for the pipe pile used in the laboratory
$_{solid}$	defines a parameter for the solid pile modelled in FLAC^{3D}

The values for E_{hollow} and ρ_{hollow} are set to the values for aluminium $7.2 \cdot 10^4$ MPa and 2700 kg/m^3 according to Teknisk Ståbi (Jensen and Olsen, 2007).

Poisson's ratio, ν, for the pile material is not scaled to fit a solid model. This leads to an incorrect scaling of the shear and bulk modulus of the pile, cf. Eqs. E.2 and E.3. However, the effect of not scaling these parameters is considered negligible as the pile primarily is subjected to bending moments. The value of ν for aluminium is 0.33.

E.3.4 Final Geometry for the Models

The grid for the piles with diameter of 40 mm and 100 mm, when the piles are installed in the soil, are shown in Figs. E.11 and E.12, respectively.

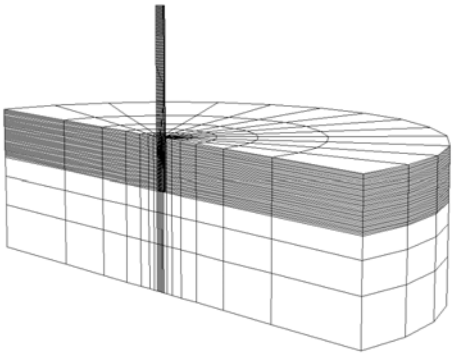

Figure E.11: Grid for the models with piles for D = 40 mm.

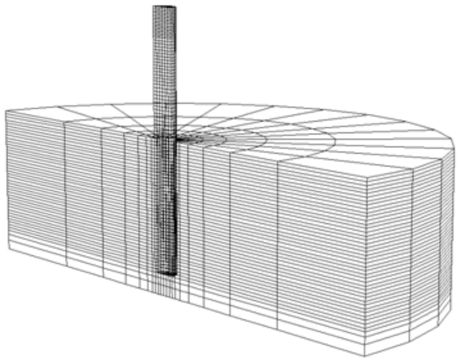

Figure E.12: Grid for the models with piles for D = 100 mm.

E.3.5 Grid Discretisation

The grid discretisation is automatically performed by FLAC^{3D}, where each zone element is divided into tetrahedron elements which are first order, constant rate of strain elements, cf. Figs. E.13 and E.14. An eight-noded zone can be discretised into two different configurations of five thetrahedrons, and the calculation of the nodal forces, based on evaluation of strain rate and stresses, are evaluated by averaging over the two configurations.

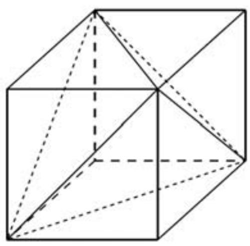

Figure E.13: Hexahedral zone discretised into five tetrahedral elements. After FLAC^{3D} 3.1 manual (2006)

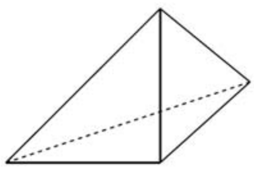

Figure E.14: Tetrahedron as employed sub zone elements in FLAC^{3D}. After FLAC^{3D} 3.1 manual (2006)

In some modelling cases combination of nodal velocities result in a deformation pattern in which no strain rate is generated. Thus, no nodal force increment is generated, and the model will not give a realistic response of the real nodal behaviour. When using tetrahedra elements this deformation pattern is avoided. However, the elements are known to exhibit an overstiff response in the framework of plasticity because they cannot deform individually without a change of volume. To overcome this problem a procedure of mixed discretisation is used. A deformation mode in which mixed discretisation would be most efficient is shown in Fig. E.15

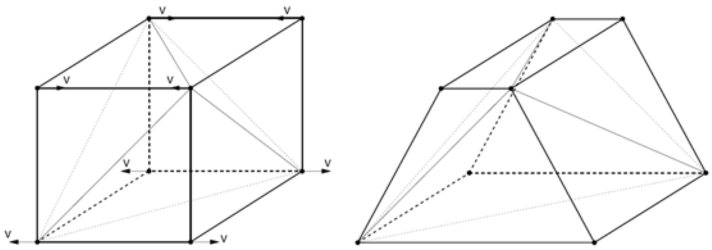

Figure E.15: Deformation mode in which mixed discretisation would be most efficient. (FLAC^{3D} 3.1 manual, 2006)

E.4 Material Models

FLAC^{3D} has twelve basic built-in material models; the "null" model, three elasticity models and eight plasticity models. Different material models are employed for the different parts of the model, i.e. the soil, the pile, and the space representing neither the soil nor the pile.

To describe the constitutive relations in the soil a Mohr-Coulomb model with tension cut-off, cf. Fig. E.16, is used. Note that compression stresses are negative in FLAC^{3D}. The Mohr-Coulomb model is an elasto-plastic model that approximates the stress-strain curve with a linear elastic perfect plastic expression, cf. Fig. E.17.

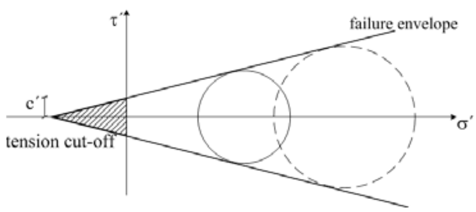

Figure E.16: Mohr-Coulomb criterion with tension cut-off.

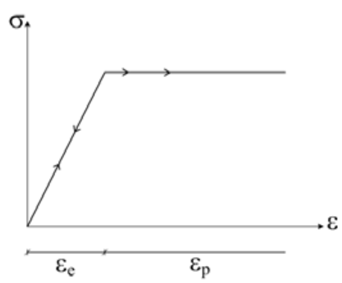

Figure E.17: Linear elastic perfect plastic stress-strain curve.

The yield function defines the stress for which plastic flow takes place and is controlled by a non-associated flow rule. The plastic flow formulation rests on basic assumptions from plasticity theory where the total strain increment can be expressed as the sum of the elastic and the plastic strain, cf. Fig. E.17. Only the elastic part contribute to the stress increment by means of Hooke's law.

The piles are modelled by use of an elastic, isotropic model which is valid for homogeneous, isotropic, continuous materials that exhibit linear stress-strain behaviour with no hysteresis on unloading.

The volume above the soil surface is modelled by the "null" model when the initial stresses in the soil are generated. In general the "null" model is used to represent material removed or excavated from the model. In this case the model represents the removed pile. The stresses within a null zone are automatically set to zero. The overburden pressure is applied afterwards.

E.5 Boundary Conditions

The boundary conditions are set to match the conditions in the pressure tank. Therefore, the outer boundaries are given as the volume of the soil mass in the tank, i.e. a diameter of 2.1 m and a soil depth of 0.58 m.

At the outer perimeter of the soil, the element nodes are restrained in the x- and y-direction. At the bottom surface of the model the nodes are restrained in all directions and because only half the laboratory test setup is modelled, the nodes at the symmetry line are restrained in the y-direction. In Fig. E.18 the dimensions for generating the boundary conditions are shown.

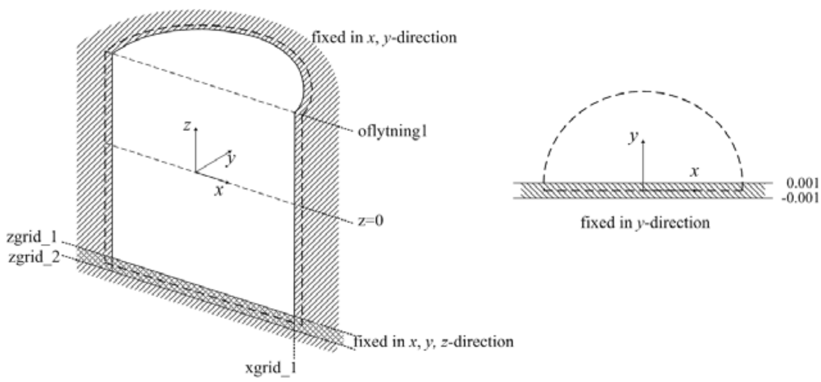

Figure E.18: Dimensions used for generating the boundary conditions.

E.6 Initial Conditions

The initial stresses are initialised based on the density of material, the gravitational loading, and the overburden pressure. The horizontal stresses are generated by use of a K_0-procedure in which $K_0 = 1 - \sin \varphi_{tr}$.

In order to prevent stress concentration near the pile, the model is brought to equilibrium with both the pile and the soil having the material properties of the soil. Further, at this initial stress state the pile is assumed smooth by setting the interface friction equal to zero. When equilibrium is reached, the correct pile and interface properties are assigned, and damping is employed in the model. Again the model is brought to equilibrium.

Another reason for bringing the model to an equilibrium state is that the interface stresses are not generated initially when the stresses are generated in the rest of the grid. To initialise the interface vector components for normal stress and shear stress, the model containing the interfaces must be brought to an initial equilibrium state.

In Figs. E.19 and E.20 the initial horizontal stresses for the models with $D = 100$ mm and $P_0 = 0$ kPa and 50 kPa, respectively, are shown. In Fig. E.20 it is seen that when overburden pressure is applied, the effective stresses in the soil is increased and the stress variation through the sand layer is minimal compared to the magnitude of the stresses.

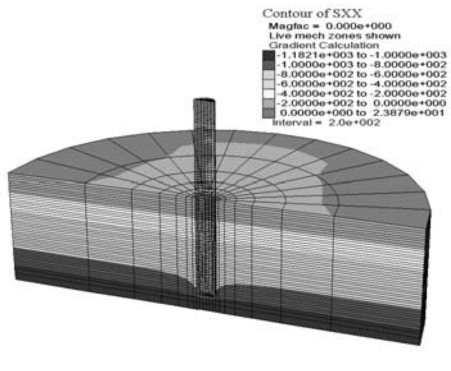

Figure E.19: Initial horizontal stresses in the model with D = 100 mm and P_0 = 0 kPa.

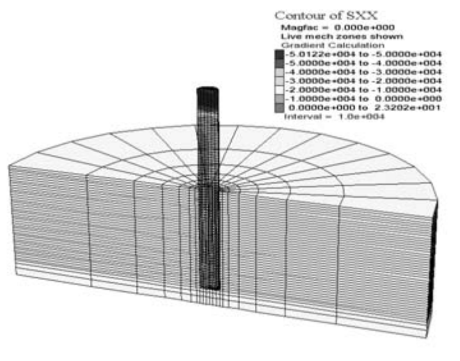

Figure E.20: Initial horizontal stresses in the model with D = 100 mm and P_0 = 50 kPa.

E.7 Numerical Damping

In order to obtain a quasi-static solution, damping is introduced in the system. In FLAC^{3D} it is possible to apply either local damping or combined damping.

In the local damping, the mass-adjustment process depends on the velocity sign-changes. For the applied velocity loading in the numerical models, the velocity components of most of the gridpoints will not change sign, hence the local damping will not be efficient. Instead the combined damping model is used. In this model damping is dependent on the sign-changes for the unbalanced force as well, and therefore more efficient in a model where the rigid-body motion of the system is significant in addition to the oscillatory motion which is to be dissipated.

E.8 Numerical Stability

In order to obtain valid results from the numerical solution of the differential equations the numerical scheme must be stable. The idealised medium is interpreted as an assembly of point masses, m, (located at the nodes) connected by linear springs with spring stiffness, k. A stable result is obtained if the timestep is chosen smaller than the critical timestep related to the minimum eigenperiod of the whole system. A global eigenvalue analysis is impractical, thus FLAC^{3D} perform a local variation of the stability analysis in which a uniform unit timestep, $\Delta t = 1$, is adopted for the whole system and the nodal masses are adjusted to fulfill the local stability condition.

For an infinite system of springs and nodal masses the limit stability criterion has the form

$$m = k(\Delta t)^2 \tag{E.6}$$

Thereby the system will be stable if the magnitude of the point mass is greater than or equal to the spring stiffness. This analysis validity can be extended to a tetrahedron by interpreting m as the nodal mass contribution at local nodes, and k as the corresponding nodal stiffness contribution. The critical timestep is thereby calculated based on the stiffness in the system.

E.9 Applying Lateral Deflection

The lateral deflection of the pile is accomplished by applying a lateral velocity in the pile at the eccentricity $z = 370$ mm. The velocities are applied to the nodes at the centre of the pile corresponding to $x = 0$ as shown in Fig. E.21. In this way no additional bending moment is introduced in the pile in contrast to the pile where the velocities are applied to all the nodes cf. Fig. E.22.

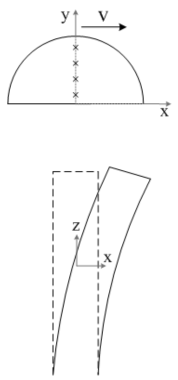

Figure E.21: Velocity applied to the nodes corresponding to $x = 0$.

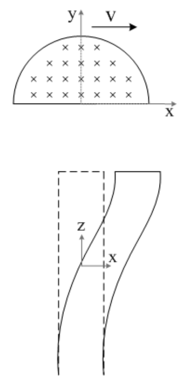

Figure E.22: Velocity applied to all the nodes.

In order to avoid a dynamic response of the system the velocity is applied in small increments. If the velocity is applied suddenly, the inertia effects will dominate and make it difficult to identify the steady-state response of the system. Thus, thousands of timesteps are required to propagate the correct loading of the model.

E.10 Calculation of Bending Moment and Soil Resistance

The bending moment, M, at a given level of the pile is calculated by use of Naviers formula, cf. Eq. E.7.

$$M = \frac{\sigma_{zz,i} \cdot I_{yy}}{x_i} \tag{E.7}$$

Where:

$\sigma_{zz,i}$	is the vertical normal stress at point i [F/L^2]
I_{yy}	is the second moment of inertia around the y-axis [L^4]
x_i	is the coordinate of point i [L]

In order to eliminate the average vertical stress corresponding to the axial force acting in the pile, the bending moment is calculated from two points ($y = 0, x = \pm D/2$) at each level of the pile, cf. Fig. E.23.

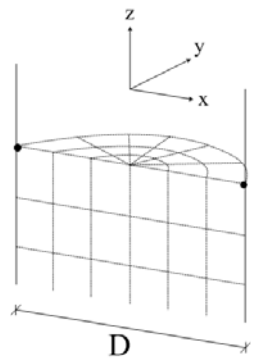

Figure E.23: Two points ($y = 0$, $x = \pm D/2$) for calculation of the bending moment in the pile.

The stresses at the interface nodes adjacent to the pile are considered as the stresses between the pile and the soil. The soil resistance per unit length along the pile is the x-component of the total stress acting in these points.

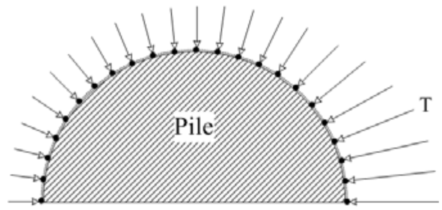

Figure E.24: Points for evaluation of the soil resistance.

At each point along the circumference, cf. Fig. E.24, the x-component of the total stress can be calculated by Eq. E.8.

$$T_x = \sigma'_{xx} n_x + \sigma'_{xy} n_y + \sigma'_{xz} n_z \tag{E.8}$$

Where:

T_x	is the x-component of the total stress acting in node i positioned in the interface elements adjacent to the pile. [F/L^2]
n_x, n_y, n_z	are components of unit normal
n_z	equals zero because the unit normal is on a horizontal plane

The soil resistance per unit length along the pile, p_x, is computed directly by integrating the x-component stresses in the interface along the circumference C, cf. Fig. E.24.

$$p_x = \int T_x dC \tag{E.9}$$

Where:

C is the circumference of the interface [L]

APPENDIX F

DIFFICULTIES WHEN CONDUCTING TESTS IN THE PRESSURE TANK

In this appendix the difficulties in the conduction of each of the six tests are described. Some of the difficulties resulted in uncertainties in test results.

An overview of the tests carried out in the pressure tank are shown in Tab. F.1 and the test results from each test are presented App. G to App. L.

Table F.1: Tests carried out in the pressure tank. The test marked with italic is not used in any analyses.

Test	Pile Diameter [mm]	Pressure [kPa]		Manometer [bar]	Force Transducer [kN]
Test 1	100	0		10	10
Test 2 - 0	*100*	*50*	*wire snapped*	*10*	*10*
Test 2 - I	100	50	wire dragged out of bracket	10	20
Test 2 - II	100	50	wire deformed and snapped	10	20
Test 2 - III	100	50	welding snapped	5	20
Test 3	100	100		5	20
Test 4	40	0		5	10
Test 5	40	50		5	10
Test 6	40	100		5	10

Test 1

Everything worked as it was supposed to.

Test 2

In total four tests was conducted for the second test. In *test 0* the wire connecting the pile and the force transducer snapped at a load of approximately 5 kN. Afterwards, the pile was brought back to upright position and the soil was vibrated until the CPT readings showed sufficient homogeneous compaction. The results from *test 0* are not used in the analysis.

For *test I* a new wire was constructed and used in the setup. During the test the wire was dragged out of the bracket leading to results with low lateral force and small deflection. Due to the small deflection *test II* was conducted without any additional movement of the pile or preparation of the soil.

Once more, the wire was replaced and *test II* was conducted. During the test the wire deformed and snapped at a load of approximately 8 kN.

During *tests 0*, *I*, and *II* the manometer showed large fluctuations in the pressure measurements. The fluctuations where at times larger than physically possible considering the size of the pressure tank versus the possible leaks in the tank. Just before *test III* the manometer reported error when measuring and was therefore replaced before *test III* was conducted. The fluctuations of the pressure measurements for the rest of the tests were much more realistic.

Before *test III* a new wire was ordered from Nordjysk Marine Service. The last test was conducted without any unloading-reloading as *test I* and *II* could be interpreted as such. At the end of *test III* the welding between the wire and the force transducer snapped at a load of approximately 11 kN.

A picture of the wrecked wires and the snapped welding are shown in Fig. F.1 and Fig. F.2, respectively.

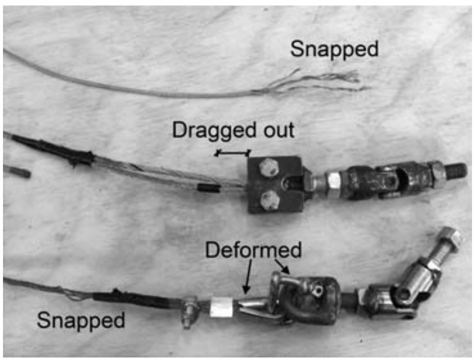

Figure F.1: Wrecked wires from *test 0*, *I*, and *II*

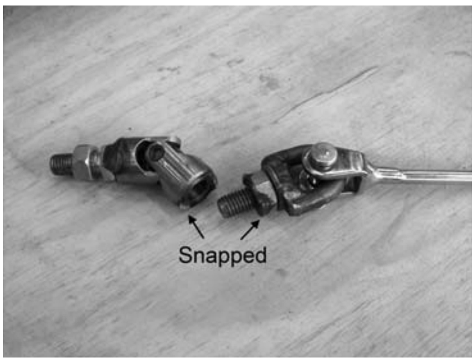

Figure F.2: Snapped welding from *test III*.

Test 3

Before the third test the welding was fixed and during the test everything worked as it was supposed to.

Test 4

When preparing the fourth test the wire was tightened while the vertical hydraulic piston was still fixing the pile. Because of the small pile diameter this caused a small deflection of the pile when the piston was removed. Furthermore, the pile got stuck in the joint between the pile and the hydraulic piston. This resulted in disturbances of the soil around the pile when removing the piston. Because of the small diameter of the pile, the soil volume activated by the pile during lateral actuation is small. Therefore, the disturbances of the soil might have large impact on the test results.

Test 5

Due to a technical error of the hydraulic piston it was unable to maintain a specific level even when turned off, if a relative heavy object was suspended to it. During the preparation of the test the pile was fixed by the piston, and because of the small weight of the pile, the drop of the piston led to an additional penetration of the pile. The pile was brought back to the right penetration depth and the soil was vibrated until the CPT readings showed sufficient homogeneous compaction.

When the CPT's were conducted the metal frame holding the CPT device fell down on the soil on the passive side of the pile. Fortunately the frame landed near the side of the pressure tank and did not disturb the soil near the pile.

The wire from the pile to the force transducer was tightened while the vertical piston was still fixing the pile. This might have caused a small deflection of the pile when the piston was removed before the test was run.

During the test, the water tab securing hydrostatic water pressure was held opened for approximately one minute after emptying the ascension pipe. This might have caused some drainage of the soil because the water flow out of the ascension pipe was faster than the water flow through the membrane. Though, because of the flow through the membrane, the sand must have obtained a state of full saturation again.

At the end of the test the leaking of the membrane increased rapidly resulting in a maximum flow of 80 L/h in the last five minutes instead of 30 L/h which was representive for the rest of the test.

Test 6

After the fifth test the soil was loosened with a gradient. Unfortunately the gradient became to high causing water channels in the soil and the soil to be loosened more than required. To reach the sufficient homogeneous compaction some extra rounds of vibration were necessary before conducting the test.

The water located above the soil surface when vibration is let out through pipes in the bottom of the tank before the membrane is placed on the soil surface. Before this test, too much water was led out and instead of a water level at the soil surface, the water level was approximately 20 mm below. To avoid vibrating the soil again, water was carefully pored in over the soil.

During the preparation of the test the fire hose was found to be leaking and the entire joint with hose clips was changed. The old and new joint are shown in Fig. F.3 and Fig. F.4 respectively.

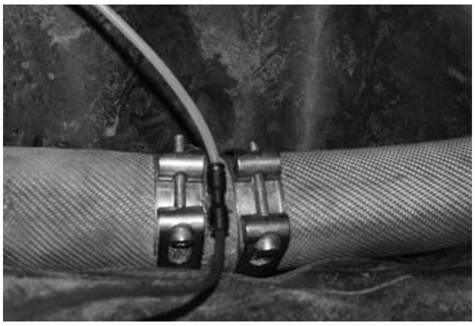

Figure F.3: Fire hose with old joint.

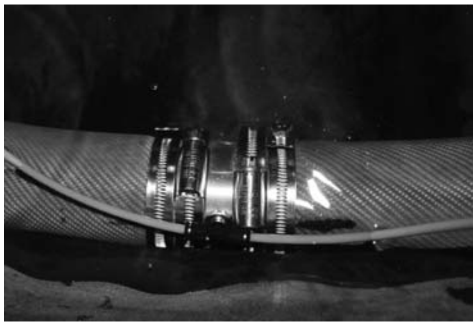

Figure F.4: Fire hose with new joint

After attaching the displacement and force transducers, the pile was stuck in the vertical hydraulic piston which resulted in disturbances of the soil around the pile when removing the piston.

TEST 1

D= 100 mm, *L* = 50 mm, P_0 = 0 kPa

CPT Readings Prior to Testing:

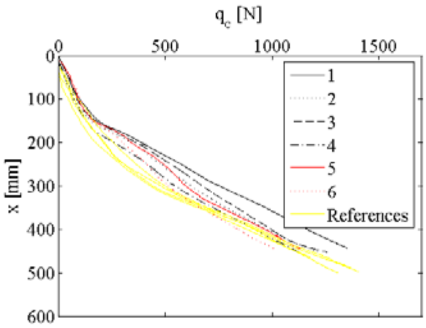

Figure G.1: Cone resistance.

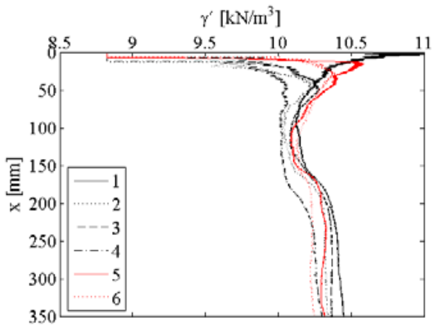

Figure G.2: Effective unit weight.

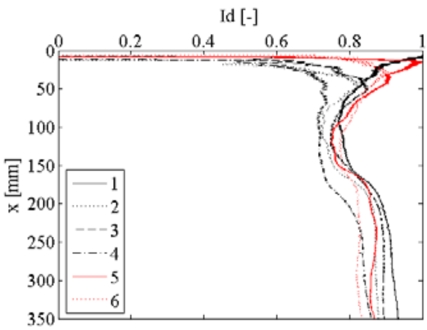

Figure G.3: Relative density.

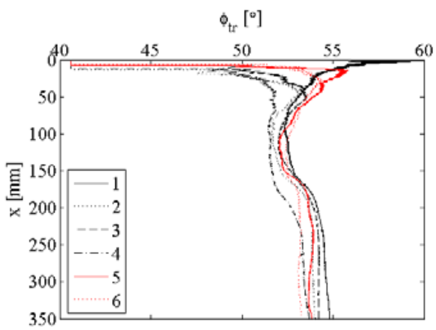

Figure G.4: Internal angle of friction.

Test Results:

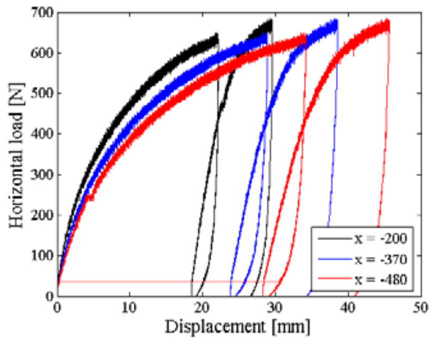

Figure G.5: Load versus displacement.

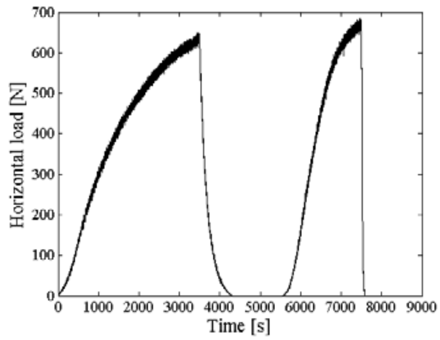

Figure G.6: Load versus time.

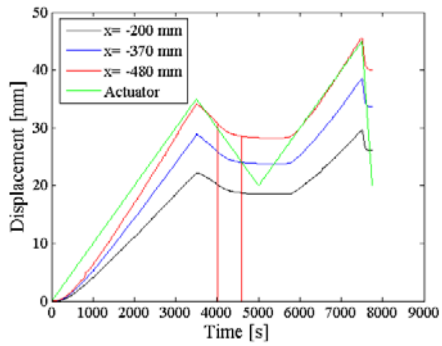

Figure G.7: Displacement versus time.

TEST 2

D= 100 mm, L = 50 mm, P_0 = 50 kPa

CPT Readings Prior to Testing:

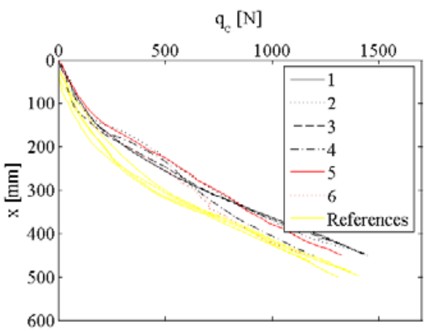

Figure H.1: Cone resistance.

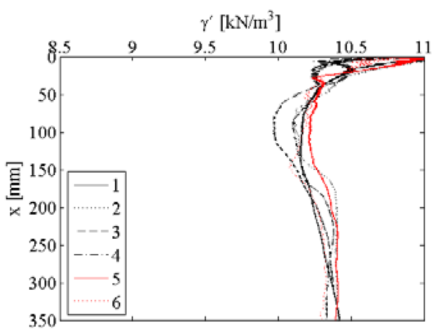

Figure H.2: Effective unit weight.

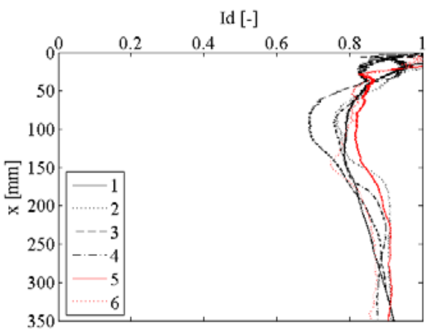

Figure H.3: Relative density.

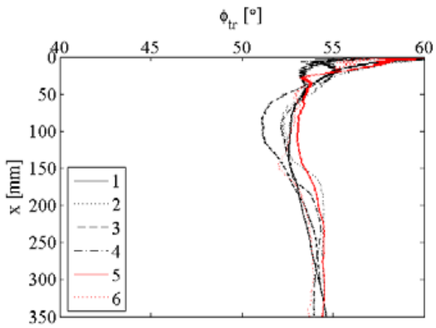

Figure H.4: Internal angle of friction.

Test Results:

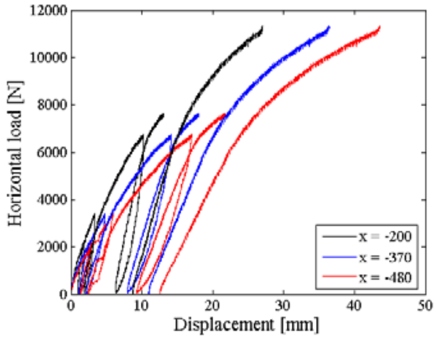

Figure H.5: Load versus displacement.

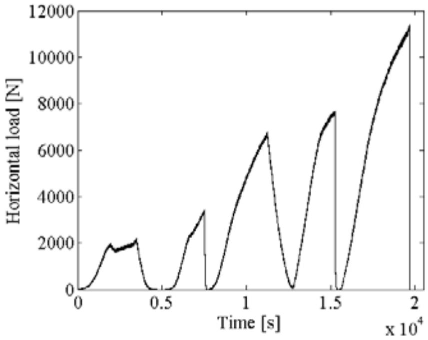

Figure H.6: Load versus time.

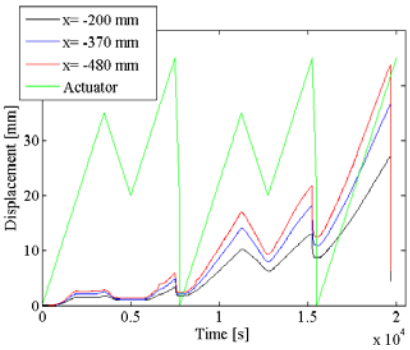

Figure H.7: Displacement versus time.

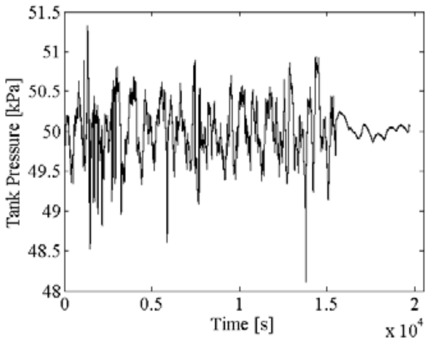

Figure H.8: Tank pressure versus time.

Test Results - test I:

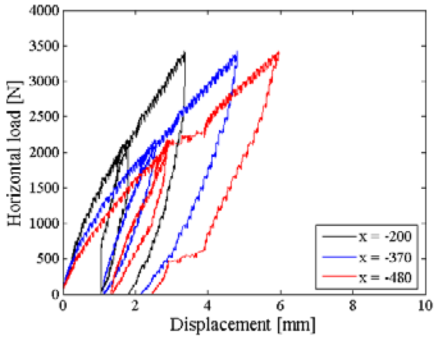

Figure H.9: Load versus displacement.

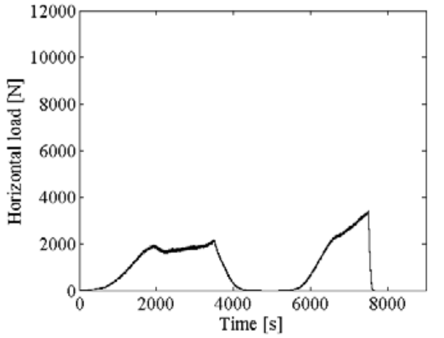

Figure H.10: Load versus time.

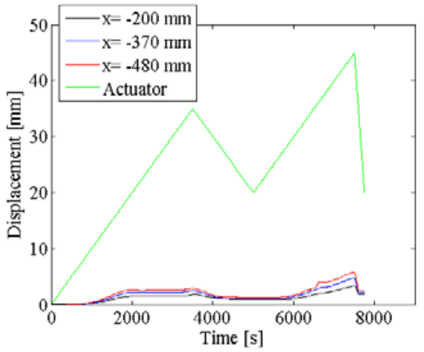

Figure H.11: Displacement versus time.

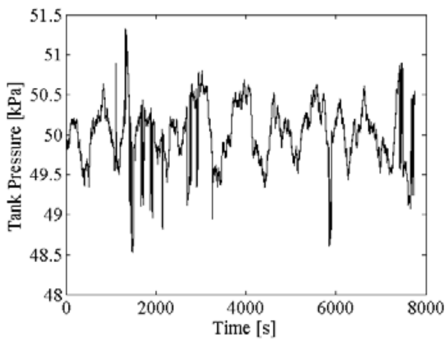

Figure H.12: Tank pressure versus time.

Test Results - test II:

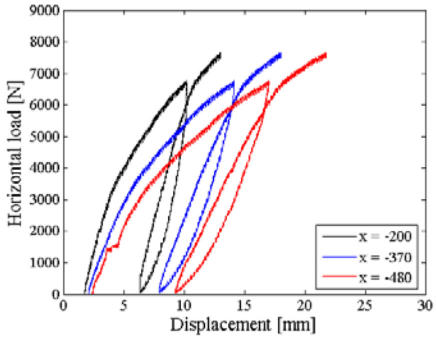

Figure H.13: Load versus displacement.

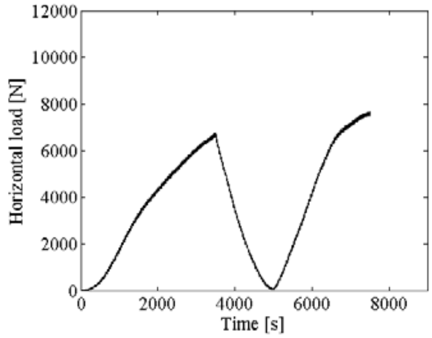

Figure H.14: Load versus time.

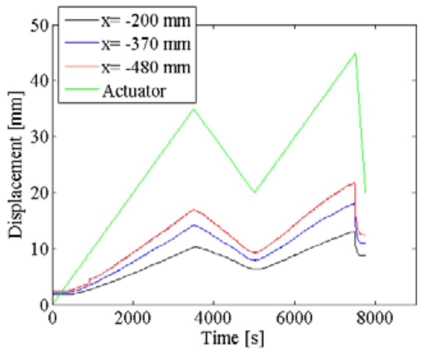

Figure H.15: Displacement versus time.

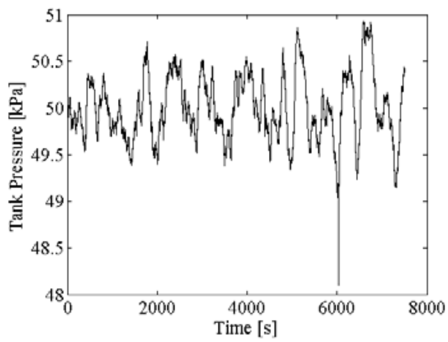

Figure H.16: Tank pressure versus time.

Test Results - test III:

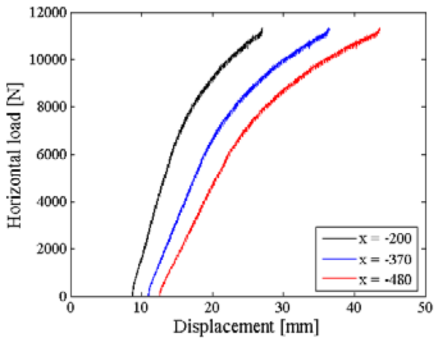

Figure H.17: Load versus displacement.

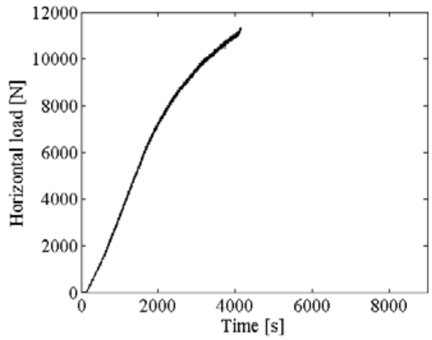

Figure H.18: Load versus time.

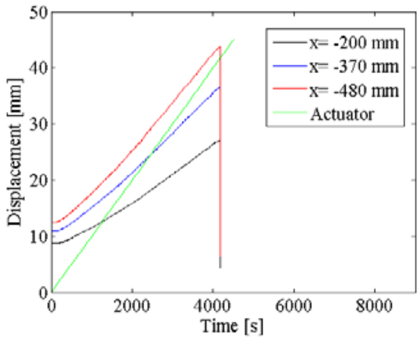

Figure H.19: Displacement versus time.

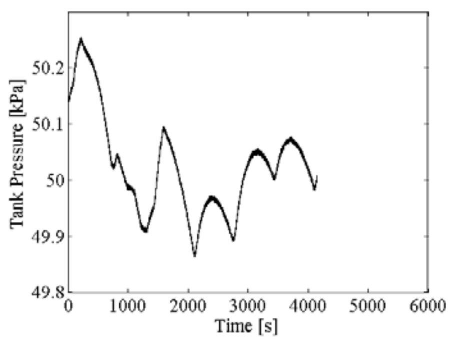

Figure H.20: Tank pressure versus time.

TEST 3

D= 100 mm, L = 50 mm, P_0 = 100 kPa

CPT Readings Prior to Testing:

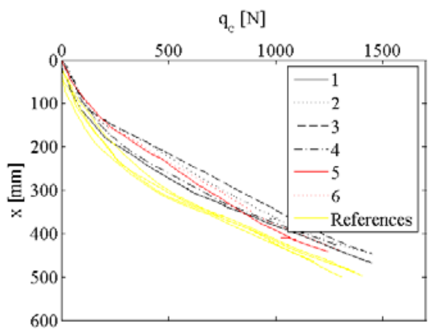

Figure I.1: Cone resistance.

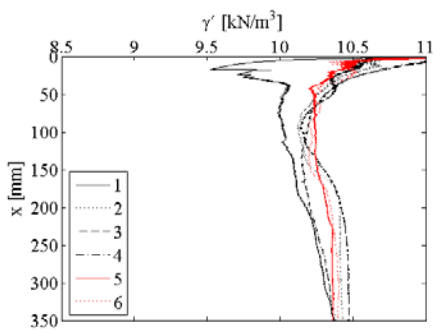

Figure I.2: Effective unit weight.

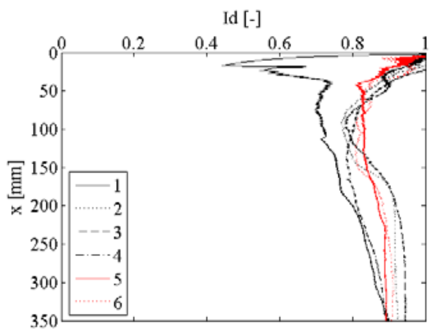

Figure I.3: Relative density.

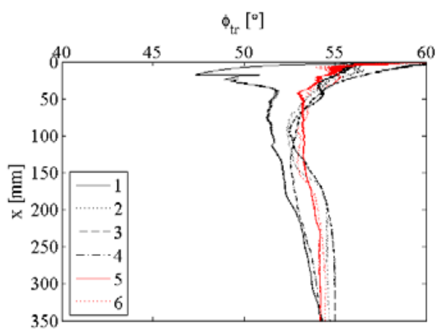

Figure I.4: Internal angle of friction.

Test Results:

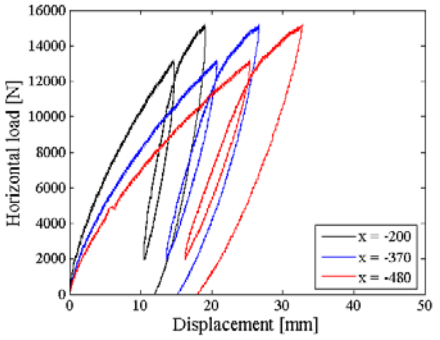

Figure I.5: Load versus displacement.

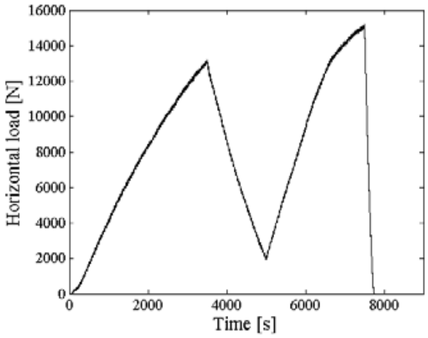

Figure I.6: Load versus time.

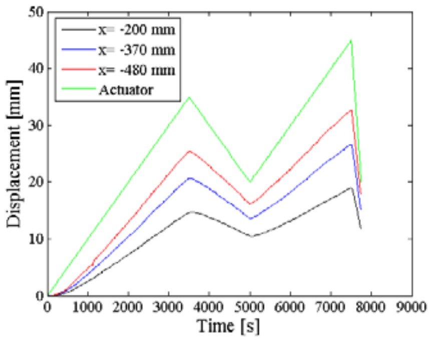

Figure I.7: Displacement versus time.

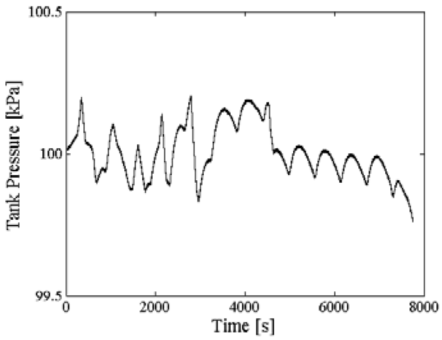

Figure I.8: Tank pressure versus time.

TEST 4

D= 40 mm, L = 20 mm, P_0 = 0 kPa

CPT Readings Prior to Testing:

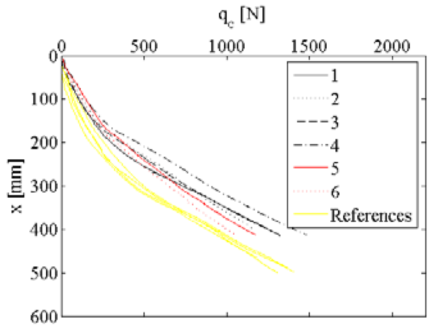

Figure J.1: Cone resistance.

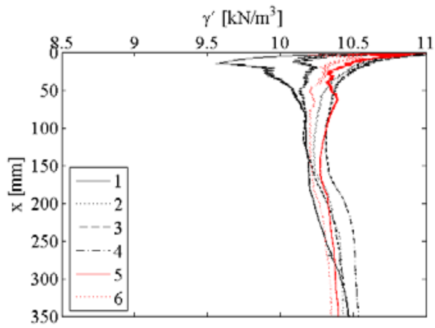

Figure J.2: Effective unit weight.

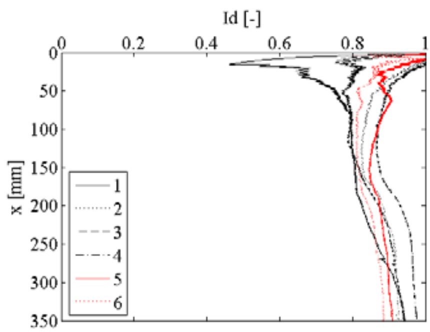

Figure J.3: Relative density.

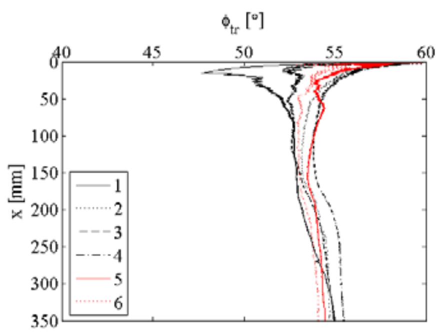

Figure J.4: Internal angle of friction.

Test Results:

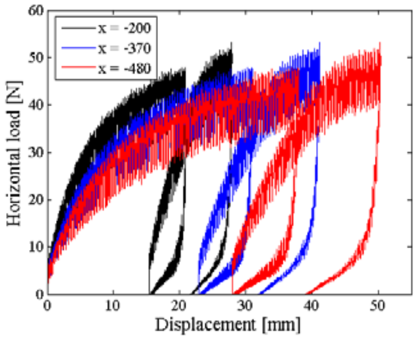

Figure J.5: Load versus displacement.

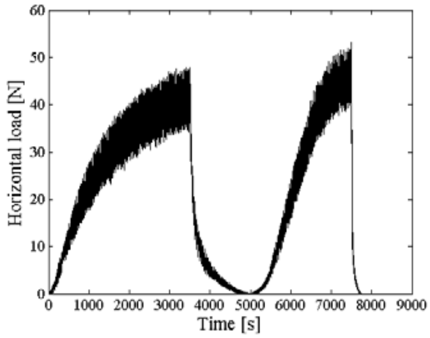

Figure J.6: Load versus time.

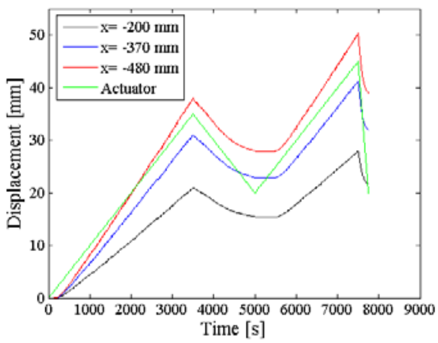

Figure J.7: Displacement versus time.

TEST 5

D= 40 mm, L = 20 mm, P_0 = 50 kPa

CPT Readings Prior to Testing:

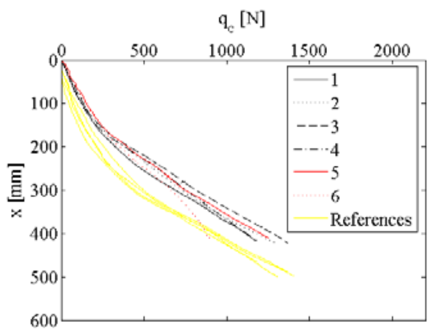

Figure K.1: Cone resistance.

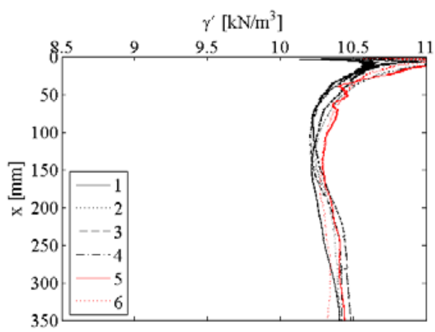

Figure K.2: Effective unit weight.

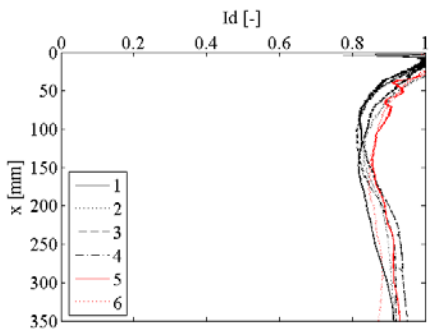

Figure K.3: Relative density.

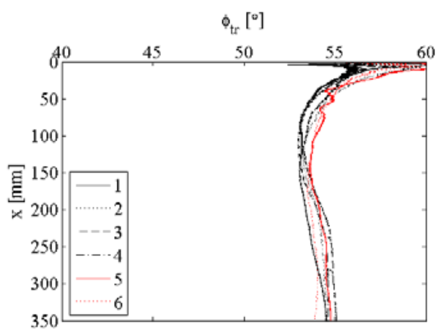

Figure K.4: Internal angle of friction.

Test Results:

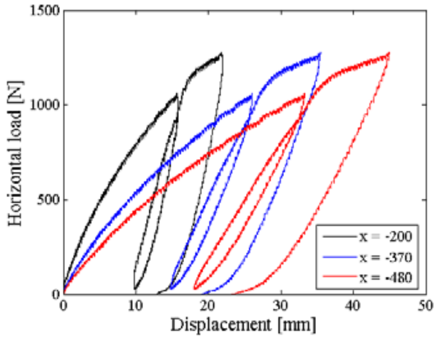

Figure K.5: Load versus displacement.

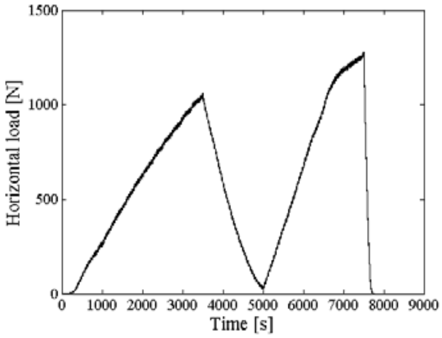

Figure K.6: Load versus time.

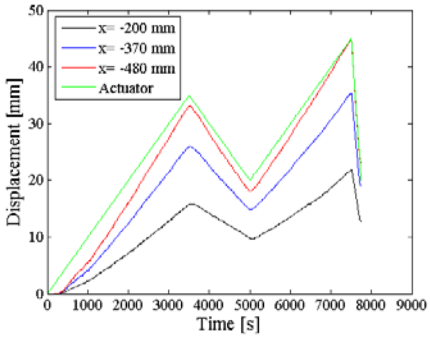

Figure K.7: Displacement versus time.

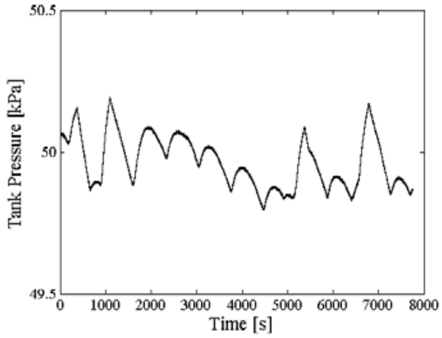

Figure K.8: Tank pressure versus time.

TEST 6

D= 40 mm, L = 20 mm, P_0 = 100 kPa

CPT Readings Prior to Testing:

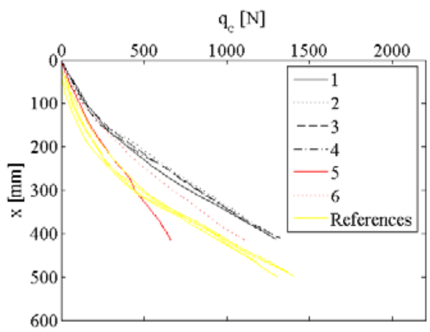

Figure L.1: Cone resistance.

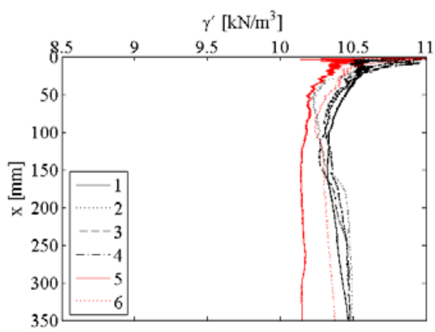

Figure L.2: Effective unit weight.

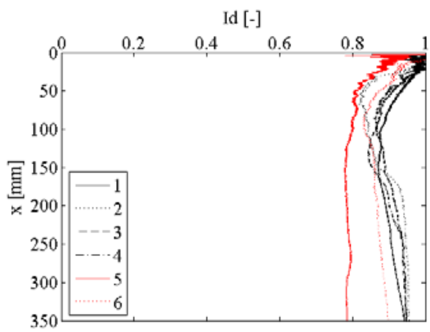

Figure L.3: Relative density.

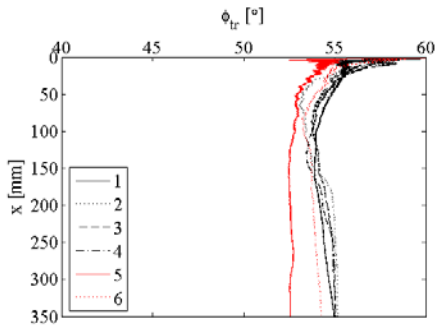

Figure L.4: Internal angle of friction.

Test Results:

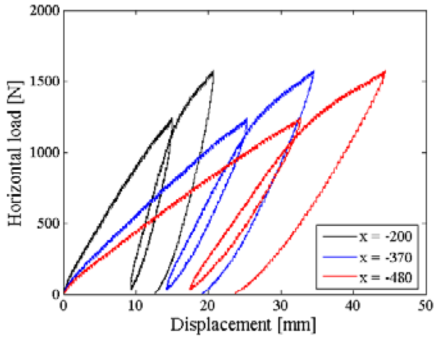

Figure L.5: Load versus displacement.

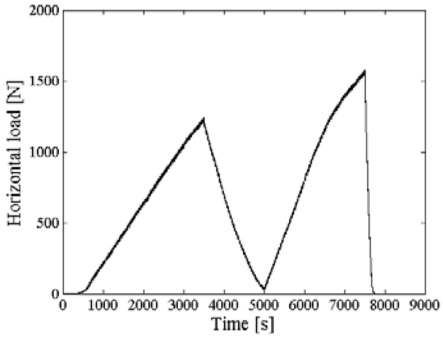

Figure L.6: Load versus time.

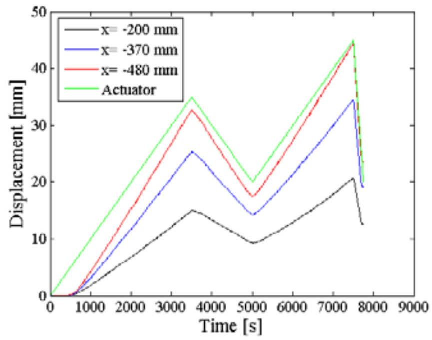

Figure L.7: Displacement versus time.

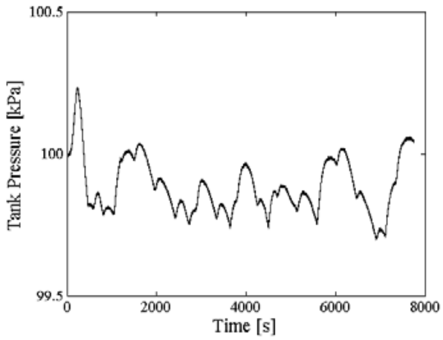

Figure L.8: Tank pressure versus time.

APPENDIX M

MODEL 1

D= 100 mm, L = 50 mm, P_0 = 0 kPa

Results from the numerical model:

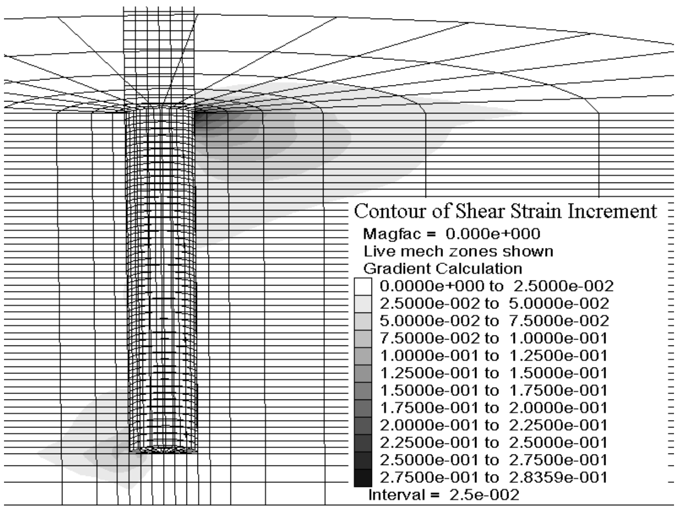

Figure M.1: Failuremode

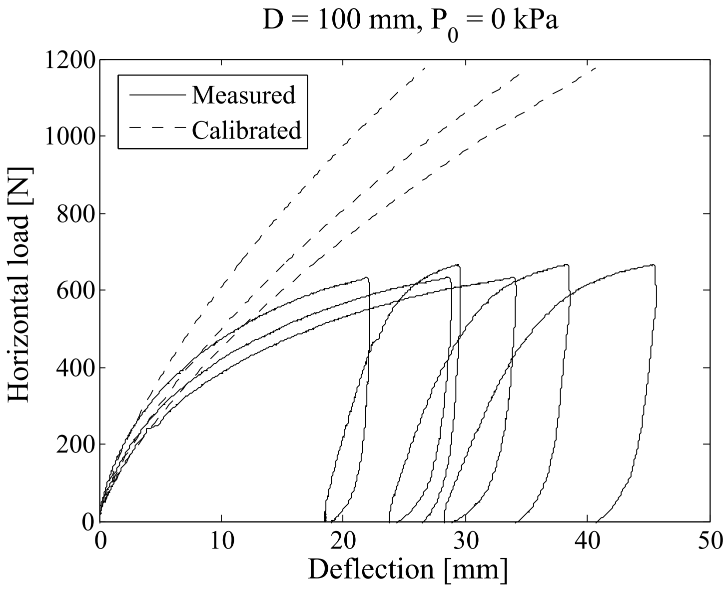

Figure M.2: Load-deflection curves calibrated by means of FLAC^{3D} compared with the measured load-deflection from the laboratory test 1.

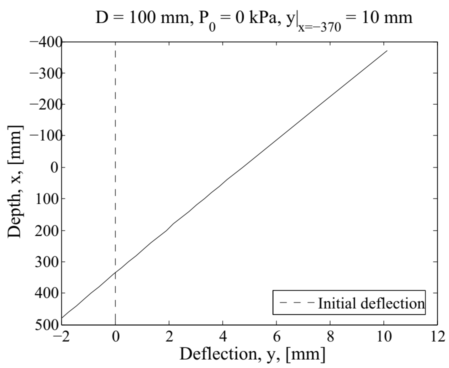

Figure M.3: Depth versus deflection when y = 10 mm at x = -370 mm.

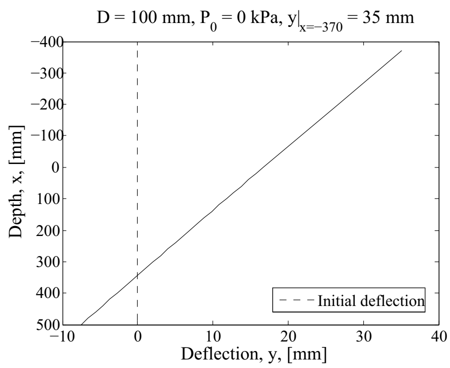

Figure M.4: Depth versus deflection when y = 35 mm at x = -370 mm.

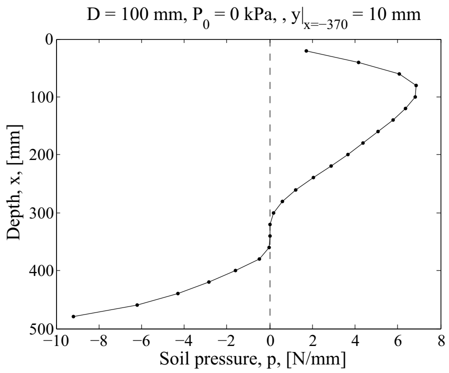

Figure M.5: Soil pressure along the pile when y = 10 mm at x = -370 mm..

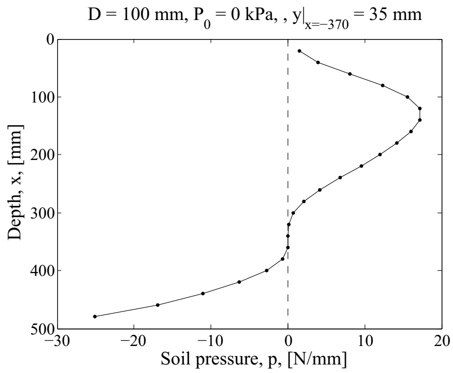

Figure M.6: Soil pressure along the pile when y = 35 mm at x = -370 mm..

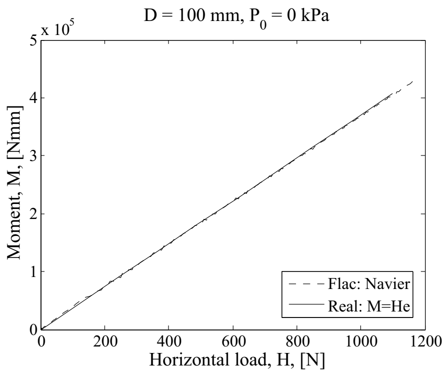

Figure M.7: Bending moment at soil surface calculated by means of FLAC^{3D} and as the horizontal load, H, times the load eccentricity, e.

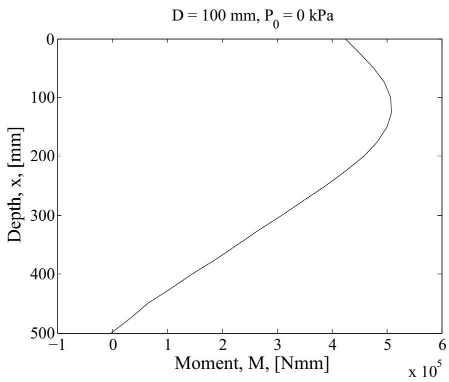

Figure M.8: Bending moment distribution when y = 35 mm at x = -370 mm.

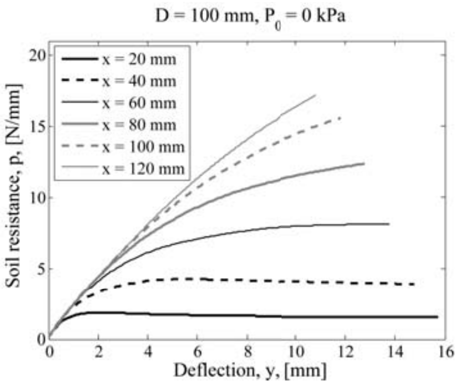

Figure M.9: $p - y$ curves at different depth x.

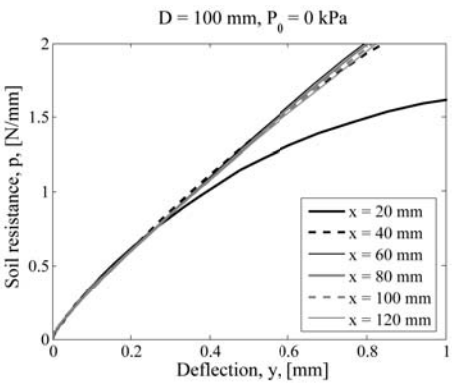

Figure M.10: Initial part of Fig. M.9.

APPENDIX N

MODEL 2

D= 100 mm, L = 50 mm, P_0 = 50 kPa

Results from the numerical model:

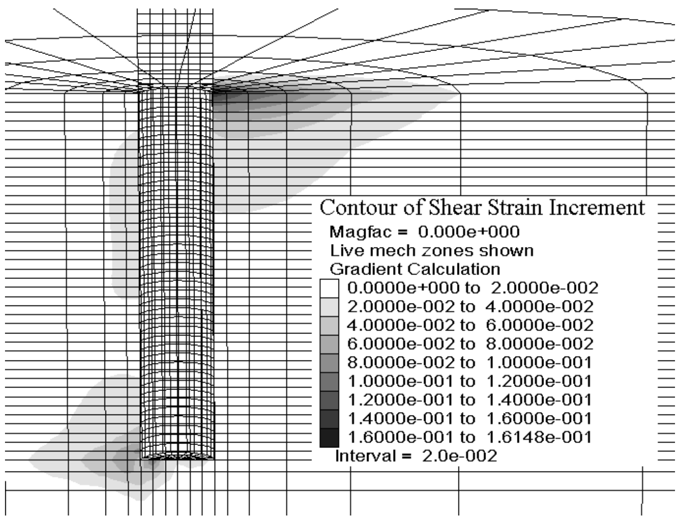

Figure N.1: Failuremode

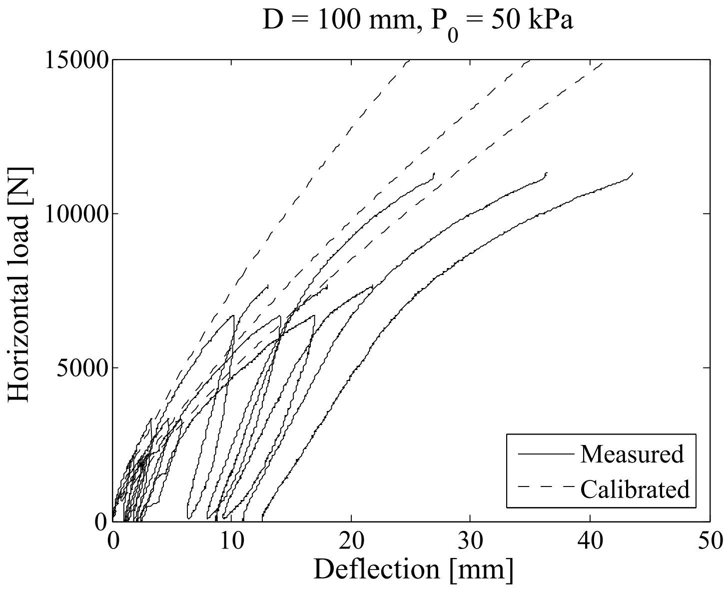

Figure N.2: Load-deflection curves calibrated by means of FLAC[3D] compared with the measured load-deflection from the laboratory test 1.

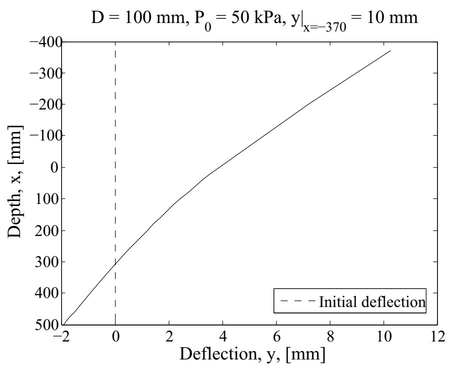

Figure N.3: Depth versus deflection when y = 10 mm at x = -370 mm.

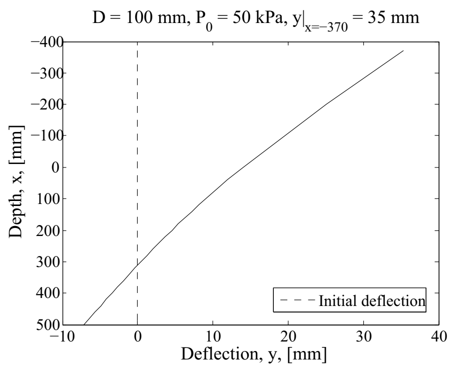

Figure N.4: Depth versus deflection when y = 35 mm at x = -370 mm.

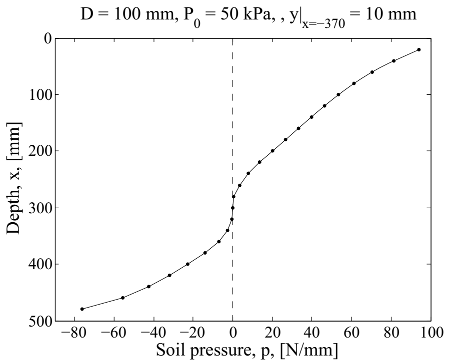

Figure N.5: Soil pressure along the pile when y = 10 mm at x = -370 mm.

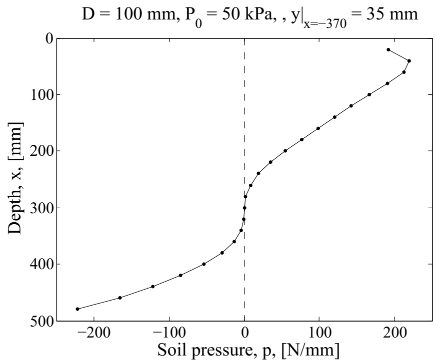

Figure N.6: Soil pressure along the pile when y = 35 mm at x = -370 mm.

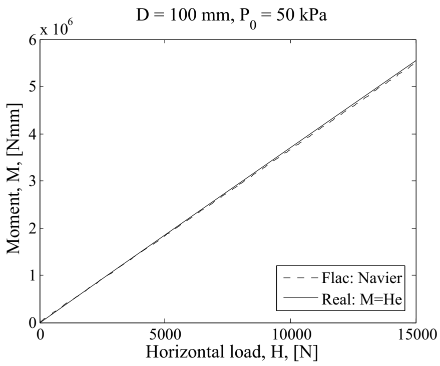

Figure N.7: Bending moment at soil surface calculated by means of FLAC^{3D} and as the horizontal load, H, times the load eccentricity, e.

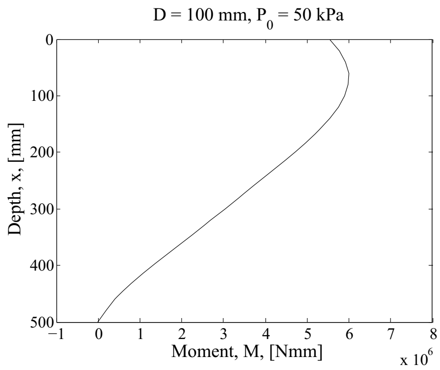

Figure N.8: Bending moment distribution when y = 35 mm at x = -370 mm.

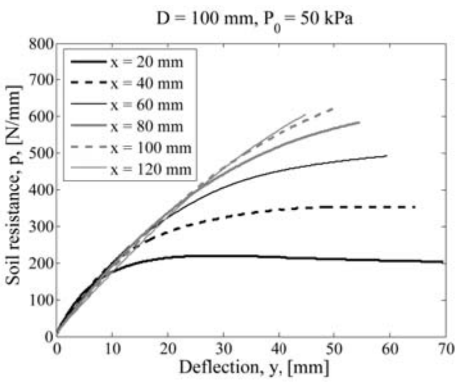

Figure N.9: $p - y$ curves at different depth x.

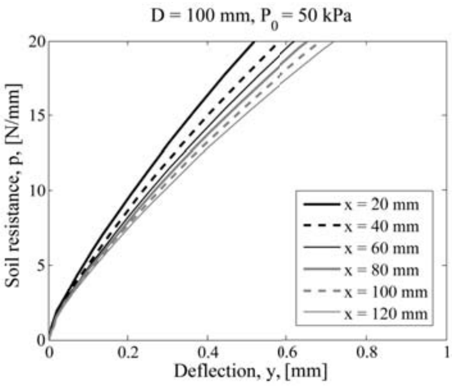

Figure N.10: Initial part of Fig. N.9.

MODEL 3

D= 100 mm, L = 50 mm, P_0 = 100 kPa

Results from the numerical model:

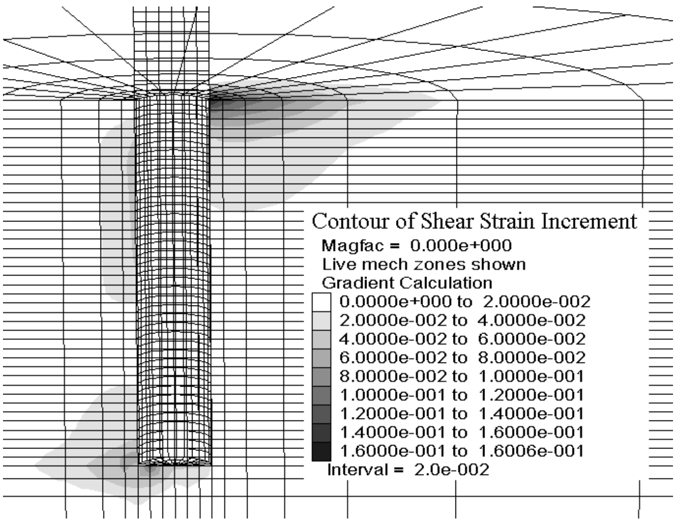

Figure O.1: Failuremode

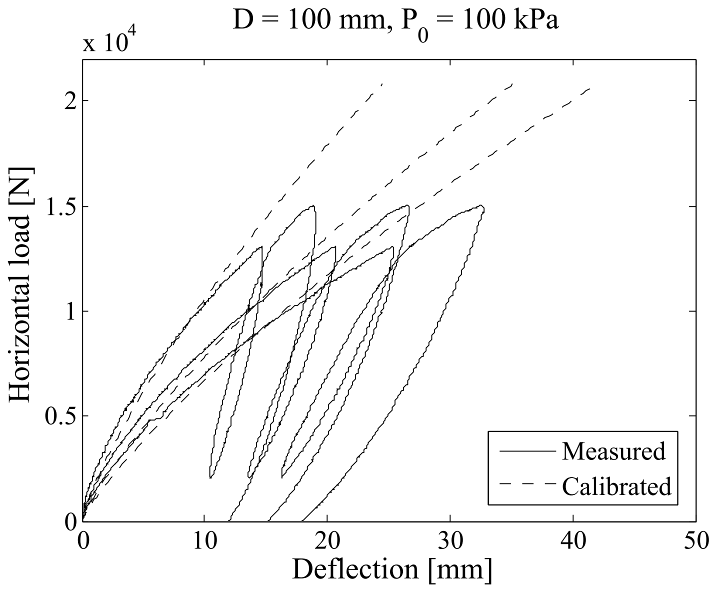

Figure O.2: Load-deflection curves calibrated by means of FLAC^{3D} compared with the measured load-deflection from the laboratory test 1.

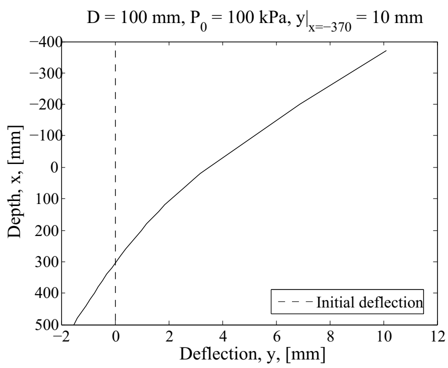

Figure O.3: Depth versus deflection when y = 10 mm at x = -370 mm.

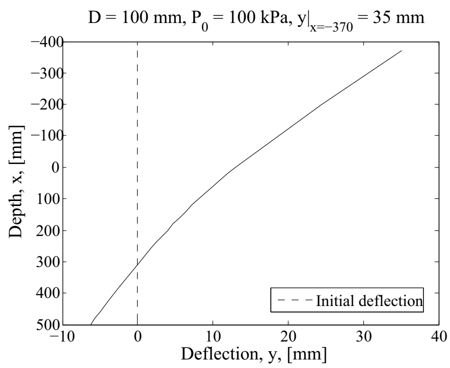

Figure O.4: Depth versus deflection when y = 35 mm at x = -370 mm.

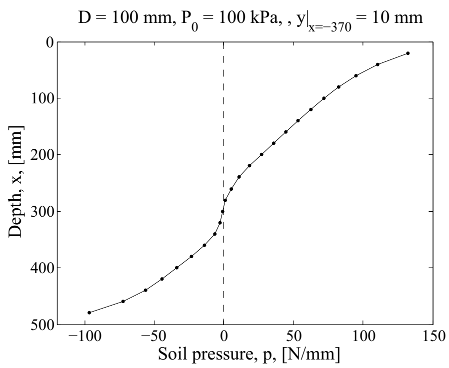

Figure O.5: Soil pressure along the pile when y = 10 mm at x = -370 mm.

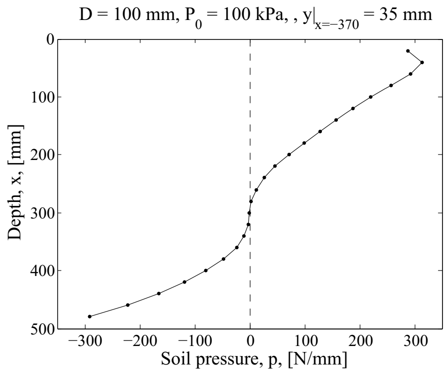

Figure O.6: Soil pressure along the pile when y = 35 mm at x = -370 mm.

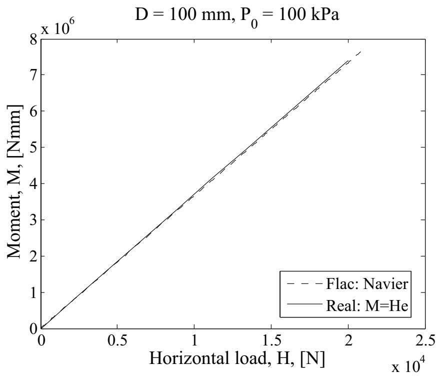

Figure O.7: Bending moment at soil surface calculated by means of FLAC^{3D} and as the horizontal load, H, times the load eccentricity, e.

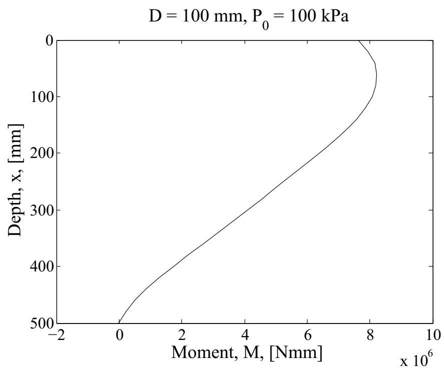

Figure O.8: Bending moment distribution when y = 35 mm at x = -370 mm.

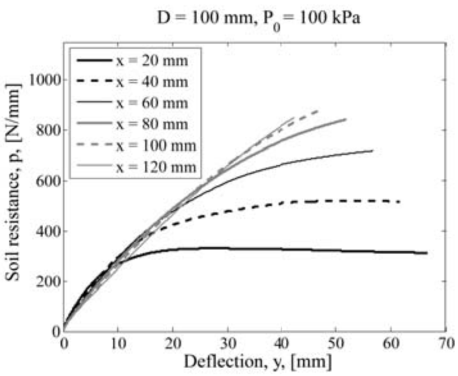

Figure O.9: $p - y$ curves at different depth x.

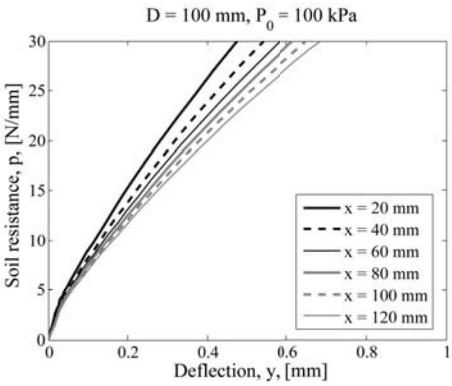

Figure O.10: Initial part of Fig. O.9.

APPENDIX P

MODEL 4

D= 40 mm, *L* = 20 mm, P_0 = 0 kPa

Results from the numerical model:

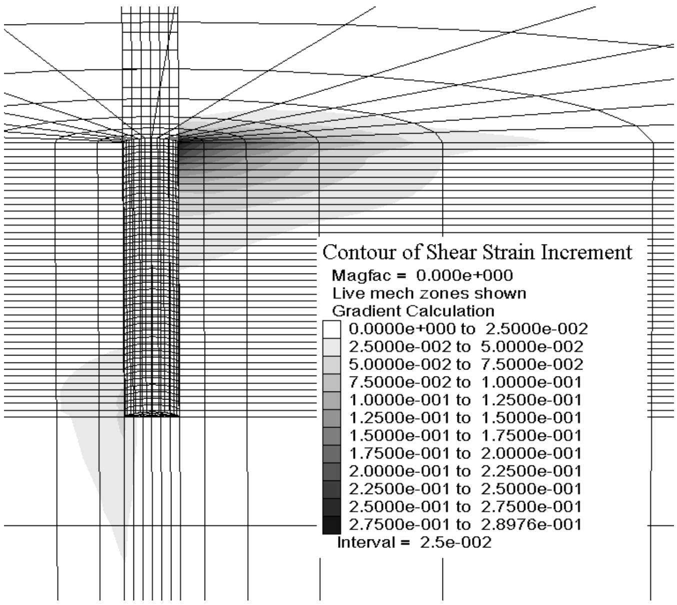

Figure P.1: Failuremode

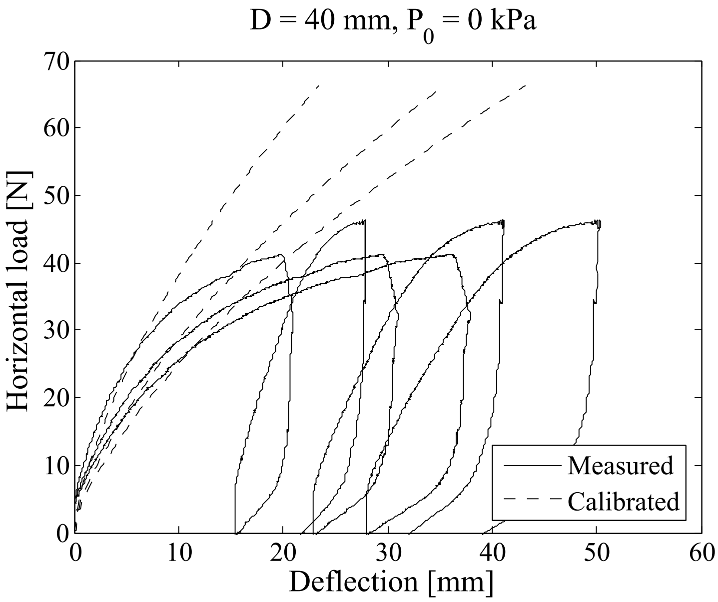

Figure P.2: Load-deflection curves calibrated by means of FLAC^{3D} compared with the measured load-deflection from the laboratory test 1.

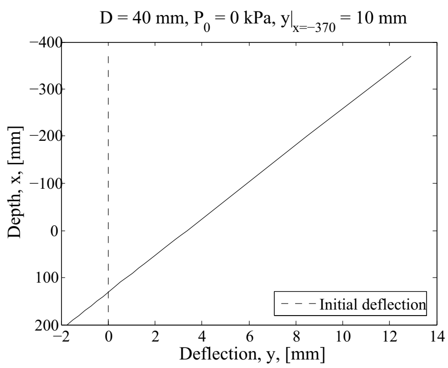

Figure P.3: Depth versus deflection when y = 10 mm at x = -370 mm.

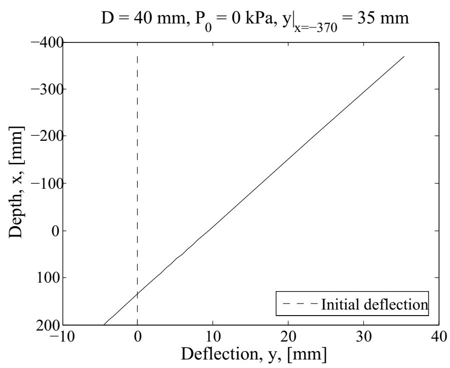

Figure P.4: Depth versus deflection when y = 35 mm at x = -370 mm.

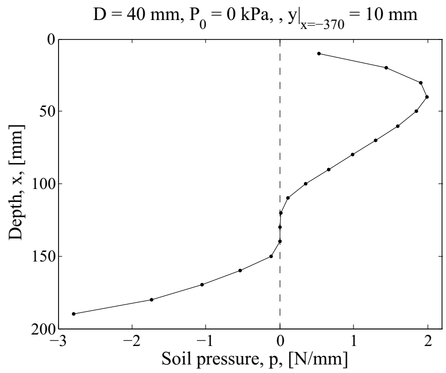

Figure P.5: Soil pressure along the pile when y = 10 mm at x = -370 mm.

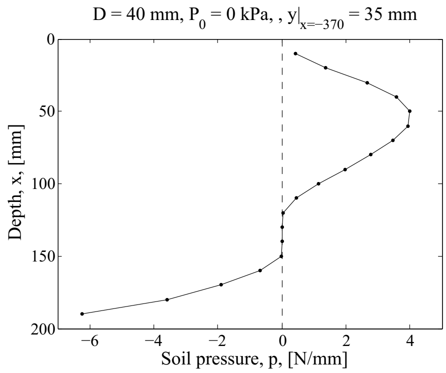

Figure P.6: Soil pressure along the pile when y = 35 mm at x = -370 mm.

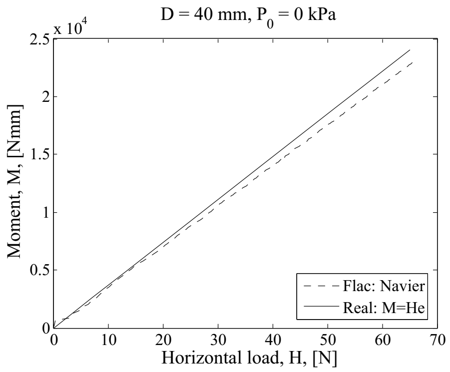

Figure P.7: Bending moment at soil surface calculated by means of FLAC^{3D} and as the horizontal load, H, times the load eccentricity, e.

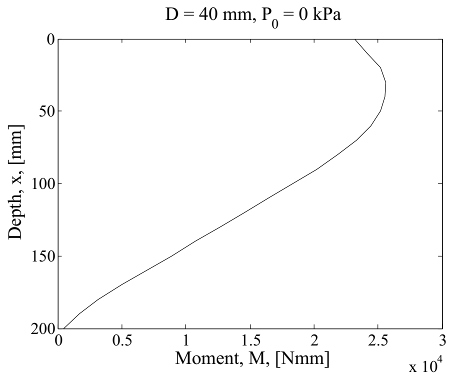

Figure P.8: Bending moment distribution when y = 35 mm at x = -370 mm.

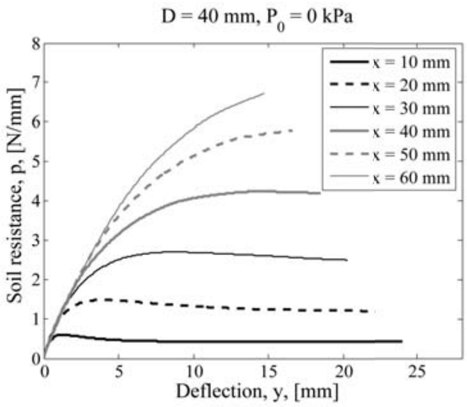

Figure P.9: $p - y$ curves at different depth x.

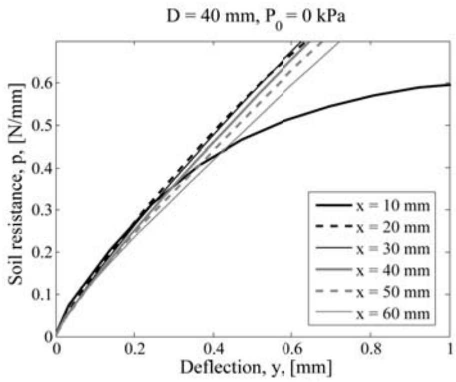

Figure P.10: Initial part of Fig. P.9.

MODEL 5

D= 40 mm, L = 20 mm, P_0 = 50 kPa

Results from the numerical model:

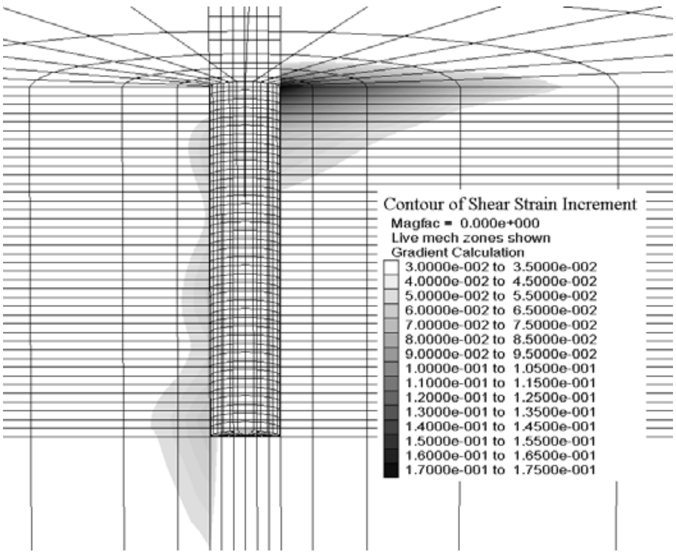

Figure Q.1: Failuremode

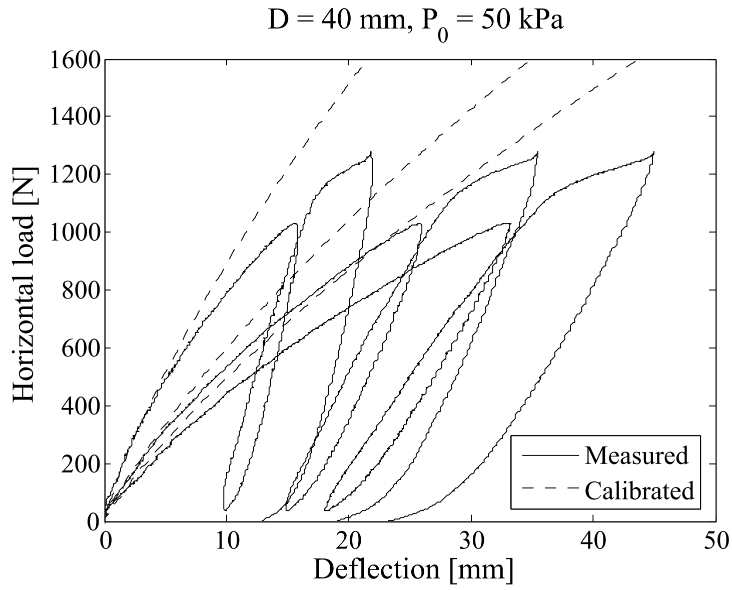

Figure Q.2: Load-deflection curves calibrated by means of FLAC^{3D} compared with the measured load-deflection from the laboratory test 1.

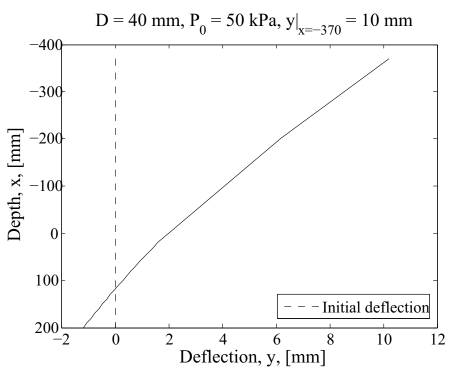

Figure Q.3: Depth versus deflection when y = 10 mm at x = -370 mm.

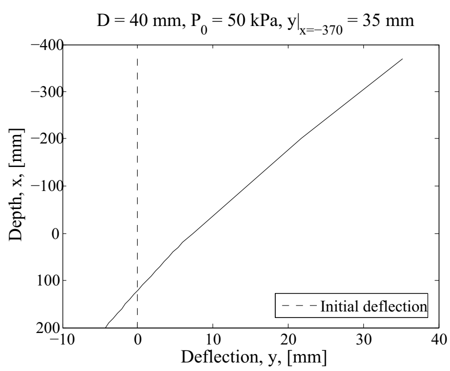

Figure Q.4: Depth versus deflection when y = 35 mm at x = -370 mm.

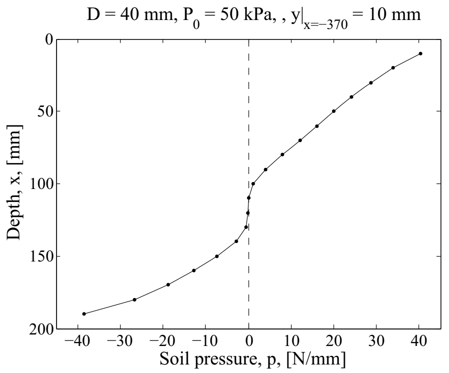

Figure Q.5: Soil pressure along the pile when y = 10 mm at x = -370 mm.

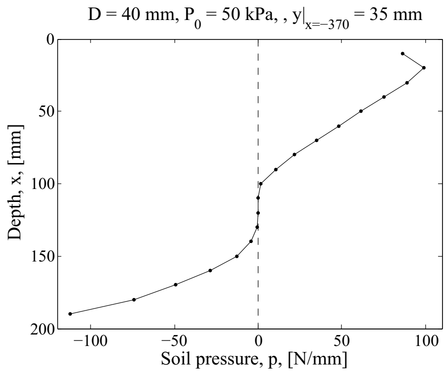

Figure Q.6: Soil pressure along the pile when y = 35 mm at x = -370 mm.

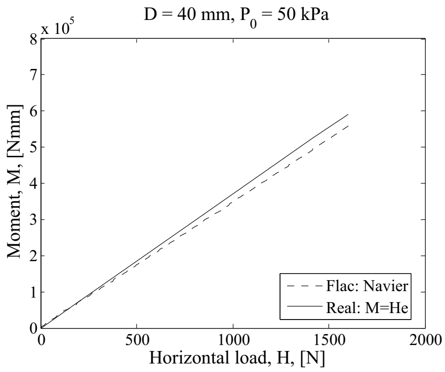

Figure Q.7: Bending moment at soil surface calculated by means of FLAC^{3D} and as the horizontal load, H, times the load eccentricity, e.

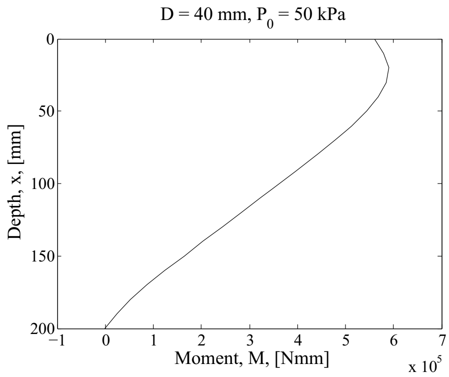

Figure Q.8: Bending moment distribution when y = 35 mm at x = -370 mm.

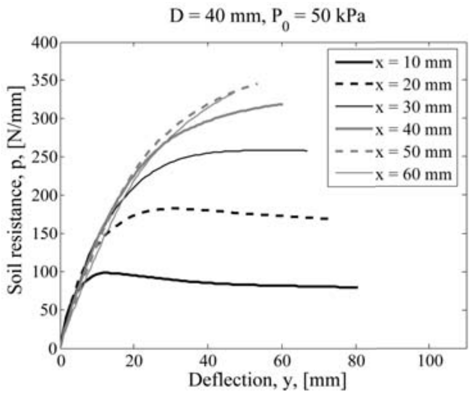

Figure Q.9: $p - y$ curves at different depth x.

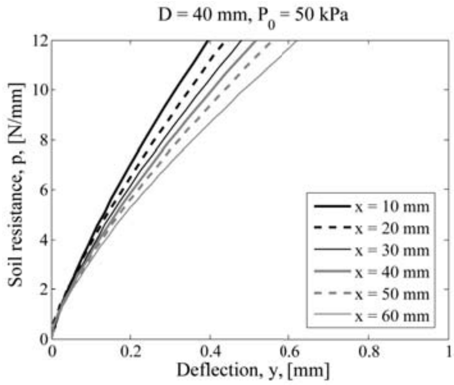

Figure Q.10: Initial part of Fig. Q.9.

APPENDIX R

MODEL 6

D= 40 mm, L = 20 mm, P_0 = 100 kPa

Results from the numerical model:

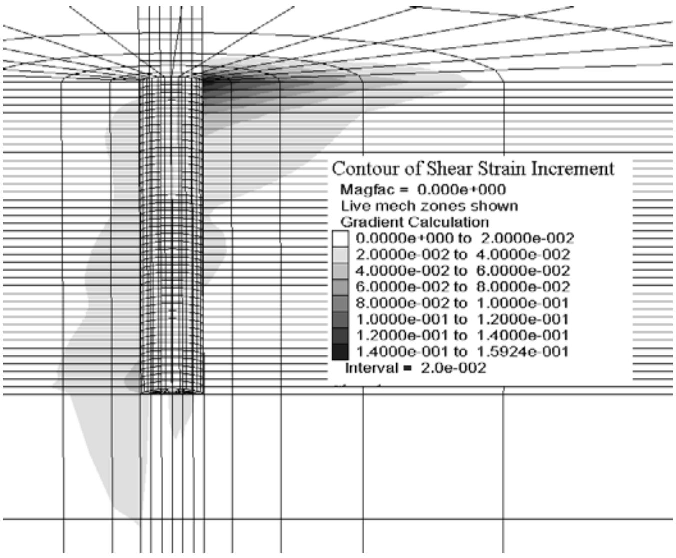

Figure R.1: Failuremode

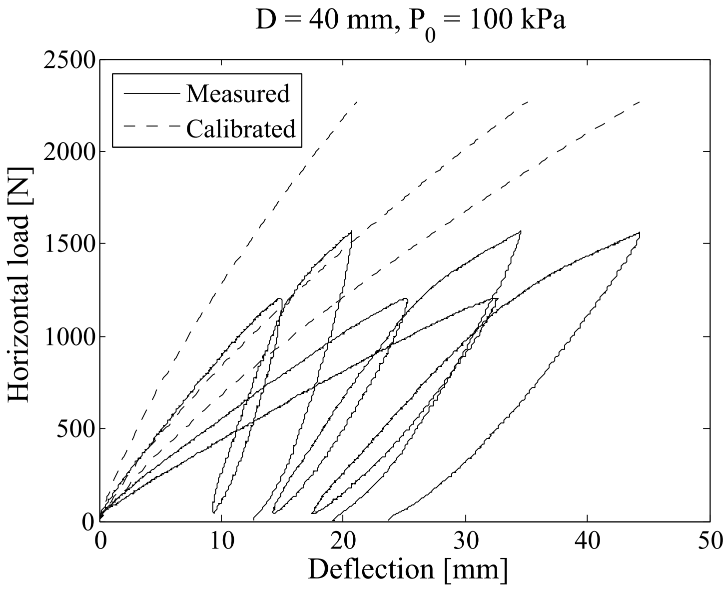

Figure R.2: Load-deflection curves calibrated by means of FLAC^{3D} compared with the measured load-deflection from the laboratory test 1.

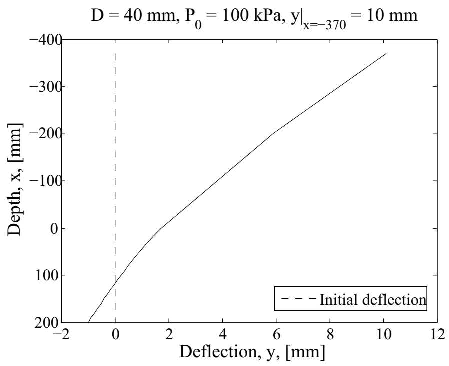

Figure R.3: Depth versus deflection when y = 10 mm at x = -370 mm.

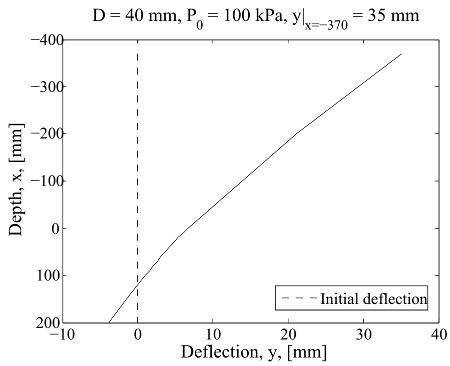

Figure R.4: Depth versus deflection when y = 35 mm at x = -370 mm.

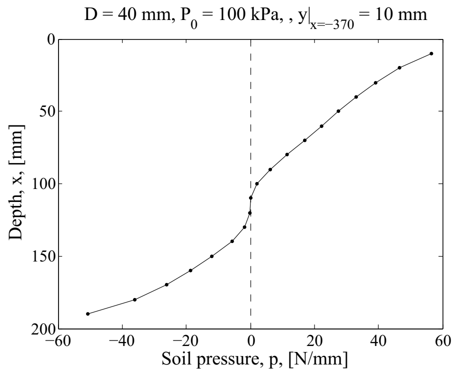

Figure R.5: Soil pressure along the pile when y = 10 mm at x = -370 mm.

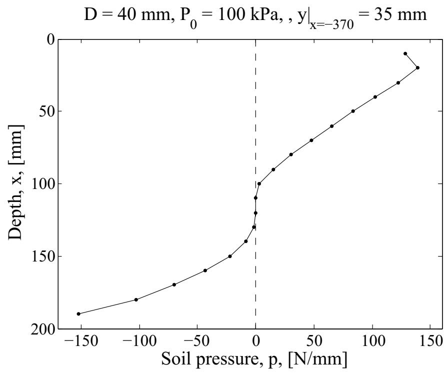

Figure R.6: Soil pressure along the pile when y = 35 mm at x = -370 mm.

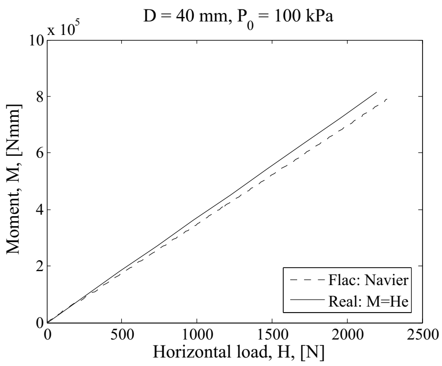

Figure R.7: Bending moment at soil surface calculated by means of FLAC^{3D} and as the horizontal load, H, times the load eccentricity, e.

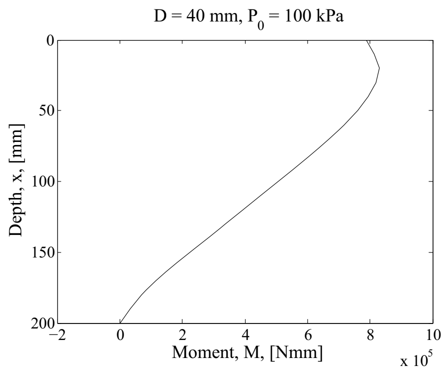

Figure R.8: Bending moment distribution when y = 35 mm at x = -370 mm.

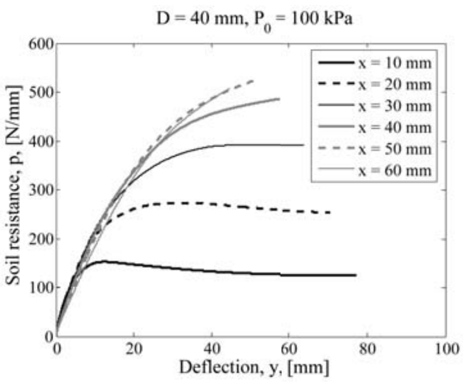

Figure R.9: $p - y$ curves at different depth x.

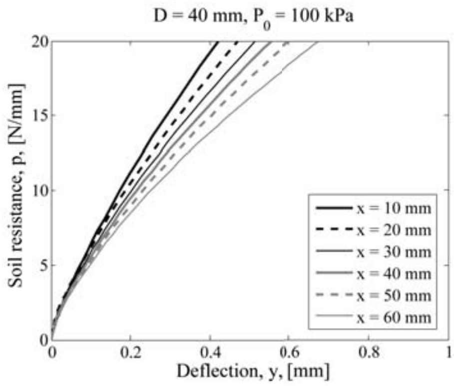

Figure R.10: Initial part of Fig. R.9.

BIBLIOGRAPHY

Andersen, A., E. Madsen, and Schaarup-Jensen (1998). Eastern Scheldt Sand, Baskarp Sand No. 15. *Data Report 9701 Part 1*. Geotechnical Engineering Group, Aalborg University.

API (1993). *Recommended Practice for Planning, Designing and Constructing Fixed Offshore Platforms – Working Stress Design*. American Petroleum Institute.

Augustesen, A. H. and L. B. Ibsen (2008, April). Assessment of existing methods for predicting soil response of laterally loaded piles in sand. *DCE Technical Report No. 41*. Aalborg Universitet.

Austrell, P., O. Dahlbom, J. Lindemann, A. Olsson, K. Olsson, K. Persson, H. Petersson, M. Ristinmaa, G. Sandberg, and P. Wernberg (2004). *CALFEM - A finite element toolbox - version 3.4*. Structural Mechanics, LTH Sweden. ISBN: 91-8855823-1.

Brødbæk, K., M. Møller, S. Sørensen, and A. Augustesen (2009, January). Evaluation of p-y relationship in cohesionless soil. *DCE Technical Report No. 57*. Aalborg University.

Brinkgreve, R. B. J. and W. Swolfs (Eds.) (2007). *PLAXIS 3D FOUNDATION, Material Models manual, Version 2*. PLAXIS b.v.

Clausen, C., P. Aas, and E. Hasle (1984). *SPLICE, a computer program for analysing structure-pile-soil interaction problems*. Norwegian Geotechnical Institute, Oslo. Publication, 152.

Cox, W. R., L. C. Reese, and B. R. Grubbs (1974, May 6–8). Field Testing of Laterally Loaded Piles in Sand. *Offshore Technology Conference*. Paper Number OTC 2079.

DNV (1992, February). *Foundations*. Det Norske Veritas. Classification Notes No. 30.4.

Fan, C.-C. and J. H. Long (2005). Assessment of existing methods for predicting soil response of laterally loaded piles in sand. *Computers and Geotechnics 32*, 274–289.

FLAC^{3D} 3.1 manual (2006). FLAC^{3D} *Fast Lagrangian Analysis of Continua in 3 Dimensions*. Itasca Consulting Group Inc., Minneapolis, Minnesota, USA.

Georgiadis, M. (1983). Development of p-y curves for layered soils. *Proceedings of the Conference on Geotechnical Engineering*, 536–545.

Gwizdala, K. and M. Jacobsen (Eds.) (1992). *Bearing capacity and settlements of piles*. Aalborg University. ISBN 87-88787-10-9.

Hansen, J. B. (1961). The Ultimate Resistance of Rigid Piles Against Transversal Forces. *Bulletin No. 12*. Geoteknisk Institut.

Ibsen, L. and L. Bødker (1994). Baskarp Sand No. 15. *Data Report 9301*. Geotechnical Engineering Group, Aalborg University.

Ibsen, L. B., M. Hanson, T. Hjort, and M. Thaarup (2009). MC-Parameter Calibration for Baskarp Sand No. 15. *DCE Technical Report No.62*. Department of Civil Engineering, Aalborg University.

Jensen, B. C. and K. Olsen (Eds.) (2007). *Teknisk Ståbi* (19th ed.). Geoteknisk Institut.

Kristensen, L. and T. Pedersen (2007). Strength and deformation abilities of suction caissons subjected to cyclic loading. *Master thesis*. Department of Civil Engineering, Aalborg University.

Leblanc, C. (2009). Design of Offshore Wind Turbine Support Structures. *DCE Thesis No. 18*. Ph.D. Thesis, Aalborg University.

Murchison, J. M. and M. W. O'Neill (1984). Evaluation of p-y Relationship in Cohesionless Soil. *Analysis and Design of Pile Foundation. Proceedings of a Symposium in Conjunction with the ASCE National Convention, ASCE*, 174–191.

Ovesen, N. K., L. Fuglsang, and G. Bagge (Eds.) (2007). *Lærebog i Geoteknik* (1st ed.). Polyteknisk Forlag. ISBN 87 502 0961 2.

Reese, L. C., W. R. Cox, and F. D. Koop (1974, May 6–8). Analysis of Laterally Loaded Piles in Sand. *Offshore Technology Conference*. Paper Number OTC 2080.

Reese, L. C. and W. F. Van Impe (2001). *Single Piles and Pile Groups under Lateral Loading*. A.A.Balkema/Rotterdam/Brookfield. ISBN 90 5809 340 9.

Sørensen, S., K. Brødbæk, M. Møller, A. Augustesen, and L. Ibsen (2009). Evaluation of the Load-Displacement Relationships for Large-Diameter Piles in Sand. *Civil-Comp Press*. Paper 244.

Sørensen, S., L. Ibsen, and A. Augustesen (2010). Effects of diameter on initial stiffness of p-y curves for large-diameter piles in sand. Aalborg University.

Sørensen, S. P., K. T. Brødbæk, and M. Møller (2009). *Evaluation of Load-Displacement Relationships for Large-Diameter Piles*. Faculties of Engineering, Science and Medicine, Aalborg University. Long Candidate Project.

The University of Western Australia (2000). *User Manual Program PYGMY* (2.31 ed.). The University of Western Australia.

Thomassen, K. and H. R. Roesen (2010). Small-Scale Testing of Laterally Loaded, Non-Slender Monopiles in Sand. Short Candidate Project.